Intrabodies as Therapeutics for Huntington's Disease

Thesis by

Amber L. Southwell

In Partial Fulfillment of the Requirements

for the Degree of

Doctor of Philosophy

California Institute of Technology

Pasadena, California

2009

(Defended March 13th 2009)

Acknowledgements

This work was funded by grants from the High Q, Hereditary Disease and McGrath Foundations, and the NINDS.

I thank David Colby and K. Dane Wittrup for providing V_L12.3, the MRC Center for Protein Engineering for providing the Griffin.1 library, Elena Cattaneo for providing ST14A cells, Christian Essrich for the design and piloting of the brain slice experiments, David Anderson for providing 293-GPG cells, David Baltimore for providing lentiviral production plasmids, Elio Vanin and Martha Bohn at Northwestern University for providing the AAV2 genome plasmid with modified CBA promoter, the University of Pennsylvania viral vector core for providing the AAV1 rep/cap plasmid, Beverly Davidson and the University of Iowa viral vector core for providing AAV1-GFP of known titer and for protocols and technical support for AAV production and purification, Jeffrey Cantle and William Yang for providing BACHD mice, Michael Hayden for providing YAC128 mice, Peggy Blue, Karen Lencioni and Janet Baer of the Caltech Office of Laboratory Animal Research, and animal care technicians Danielle Willis, Amanda Updike, and Reyna Sauza.

I would also like to thank my advisor Paul Patterson for being supportive, interested, available, collaborative, knowledgeable, excellent at problem solving, and fun to laugh with.

My thesis committee: Erin Shuman, David Anderson, Henry Lester and Ali Khoshnan for their high expectations and wonderful input.

Previous and current Patterson lab members Jan Ko, Limin Shi, Susan Ou, Kristina Holmberg, Sylvian Bauer, Natalie Malkova, Ben Deverman, Catherine Bregere, Erin Watkin, Stephen Smith, Wally Bugg, Elaine Hsiao and Kelly Lin as well as previous and current members of other Caltech labs Mark Zylka, Xinzhong Dong, Tim lebestky, Sacha Malin, Wulf Haubensak, Agnes Lukaszewicz, Chi-Sung Chiu, Andrew Tapper, Holly Beale, Anne Hergarden, Elizabeth Jones and Devin Tesar for providing reagents, instruction and support.

Thanks to my undergraduate research advisors Nigel Atkinson and Harold Zakon for choosing me from the large number of undergraduates applying for research positions as well as for their instruction and continued support.

Thanks to my parents Dolly Southwell and Terry Southwell for passing on their curiosity and love of science and knowledge.

And last but certainly not least, my husband, Jason Hovel, for providing custom behavioral equipment and data analysis software as well as for making my life better in every way and making sure I ate and slept while writing this.

ABSTRACT

Huntington's disease (HD) is a devastating, genetic, neurodegenerative disease for which there is currently no effective therapy. The polyglutamine (polyQ) expansion that causes HD is in the first exon (HDx1) of huntingtin (Htt). However, other parts of the protein, including the 17 N-terminal amino acids (AAs) and two proline (polyP) repeat domains, modulate the toxicity of mutant Htt (mHtt). The role of the P-rich domain that is flanked by the polyP domains has not been explored. Using highly specific intracellular antibodies (intrabodies; iAbs), we tested various epitopes for their roles in mHDx1 toxicity, aggregation, localization and turnover. Three domains in the P-rich region (PRR) of HDx1 are defined by iAbs: MW7 binds the two polyP domains, and Happs 1 and 3, two new iAbs, bind the unique, P-rich epitope located between the two polyP epitopes. In cultured cells, we find that the three PRR-binding iAbs, as well as V_L12.3, which binds an epitope in the N-terminal 17 AA segment, decrease the toxicity and aggregation of mHDx-1, but they do so by different mechanisms. The PRR-binding iAbs have no effect on Htt localization, but they cause a significant increase in the turnover rate of mHtt, which V_L12.3 does not change. In contrast, expression of V_L12.3 increases nuclear Htt. These results suggest that the PRR domain regulates mHtt stability and toxicity. Thus, compromising this pathogenic epitope by iAb binding represents a novel therapeutic strategy for treating HD.

We have tested this hypothesis by delivering both V_L12.3 and Happ1 to the brains of HD model mice using an AAV2/1 viral vector with a modified CBA promoter. V_L12.3 treatment, while beneficial in a lentiviral model of HD, has no

effect on the YAC128 HD model and actually increases severity of phenotype and mortality in the R6/2 HD model. In contrast, Happ1 treatment confers significant beneficial effects in assays of motor and cognitive deficits as well as in the neuropathology found in the lentiviral, R6/2, N171-82Q, YAC128 and BACH models of HD. These results indicate that increasing the turnover of mHtt using AAV-Happ1 gene therapy represents a highly specific and effective treatment possibility for HD.

Contents

LIST OF FIGURES

ABBREVIATIONS

AA, amino acid

AAV, adeno-associated virus

AD, Alzheimer's disease

ANOVA, analysis of variance

APP, amyloid precursor protein

BDNF, brain derived neurotrophic factor

CBA, chicken β-actin

CFP, cyan fluorescent protein

CMV, cytomegalovirus

CNS, central nervous system

DARPP-32, dopamine- and cyclic AMP-regulated phosphoprotein

EthD-2, ethidium homodimer-2

FBS, fetal bovine serum

GDNF, glia derived neurotrophic factor

GFP, green fluorescent protein

GTS, glutathione-s-transferase

HA, hemaglutinin epitope tag

HDAC, histone de-acetylase

HD, Huntington's disease

HDx-1, huntingtin exon 1

HRP, horseradish peroxidase

Htt, huntingtin

iAb, intrabody

IHC, immunohistochemistry

IPTG, isopropyl β-D-1-thiogalactopyranoside

ITI, inter trial interval

LDH, lactate dehydrogenase

NHP, non-human primate

NMDAR, N-methyl-D-aspartate receptor

MSNs, medium spiny neurons

mx, mutant x

ORF, open reading frame

PBS, phosphate buffered saline

PCR, polymerase chain reaction

PD, Parkinson's disease

PFA, paraformaldehyde

polyP, polyproline

polyQ, polyglutamine

P-rich, proline rich

PRR, proline rich region

Px, postnatal day x

scFv, single chain fragment variable

SDS/PAGE, sodium dodecyl sulfate polyacrylamide gel electrophoresis

T1, trial 1

T2, trial 2

WT, wildtype

YFP, yellow fluorescent protein

Chapter 1

Introduction

Huntington's disease is an autosomal dominant, progressive, neurodegenerative disorder that results from the expansion of a polyglutamine (polyQ) tract in HDx-1 (Huntington's disease collaborative research group,1993). At least nine other neurodegenerative diseases are caused by the expansion of a polyQ tract, including several types of spino-cerebellar ataxia (Orr et al., 1993; Kawaguchi et al., 1994; Imbert et al., 1996; David et al., 1997), dentatorubral pallidoluysian atrophy (Koide et al., 1994), and spino-bulbar muscular atrophy (Spada et al., 1991). In each case, the polyQ expansion is in a different protein, and although the mutant protein is expressed widely, only a specific subset of neurons, unique to each disease, die. Although expression of pure polyQ is sufficient to cause toxicity (Marsh et al., 2000; Yang et al., 2002), it is the protein context surrounding the polyQ expansion that makes particular neurons susceptible in each disease. In HD, the mutant protein, mutant huntingtin (mHtt), exhibits toxic gain of function, which includes aggregation, sequestering of important cellular proteins, aberrant protein-protein interactions, disruption of the ubiquitin proteasome, and dysregulation of axonal transport, transcription, and mitochondrial metabolism (Ramaswamy et al., 2007; Rosas et al., 2008). This leads to chorea, dementia, weight loss and loss of striatal medium spiny neurons (MSNs) as well as some cortical neurons (Nakamura and Aminoff, 2007).

The simple genetic nature and autosomal dominant transmission of HD should facilitate therapy development. Unlike Alzheimer's and Parkinson's

diseases (AD and PD), which are predominately idiopathic and not diagnosed until significant neuronal loss has occurred, there is an opportunity for reliable pre-symptomatic treatment of HD. This allows for neuroprotective strategies rather than more complicated restorative strategies such as fetal graft transplantation or strategies for coping with existing neuronal loss such as L-Dopa treatment for PD. Surprisingly, the therapies currently available to HD patients are aimed at symptom management rather than disease process. These include SSRIs and atypical anti-psychotics for psychiatric disturbances and tetrabenzine for chorea (recently, the first drug to be approved by the FDA specifically for the treatment of HD)(Huntington Study Group, 2006). Though HD has a single genetic cause, it has a very complex pathology with detrimental effects on a wide variety of cellular processes. As a result, a wide variety of therapies aimed at downstream events have been investigated in both pre-clinical and clinical trials.

Pre-clinical experiments involve the use of animal models. In the case of HD there are *C. elegans*, *Drosophila*, rodent, sheep, and non-human primate (NHP) models available. These models are generated by neurotoxic lesion or genetically by viral delivery or germline manipulation.

The short experimental time frame of *C. elegans* and *Drosophila* models is well suited to high throughput screening and proof of principal studies. However, the simplicity of the *C. elegans* nervous system and the absence of higher brain structures and endogenous Htt in *Drosophila* lessen the impact of therapeutic trials using these models.

Despite the large number of available HD mouse models, no one model completely recapitulates the human disease (Ehrnhoefer et al., 2009). Transgenic mice expressing N-terminal mHtt fragments (which are much more toxic than full-length mHtt), such as the R6/2 and N171-82Q lines, exhibit rapid onset of progressive motor and cognitive deficits, weight loss, Htt inclusion formation, and striatal atrophy accompanied by ventricular enlargement, but no loss of MSNs (Mangiarini et al., 1996; Carter et al., 1999; Lione et al., 1999; Schilling et al., 1999). These models are also limited to therapeutic strategies directed at the N-terminus of mHtt, so they cannot be used to study modifiers of mHtt toxicity with sites of action outside of this area such as caspase-6 cleavage (Graham et al., 2006). Given its rapid symptom onset, the R6/2 line is widely used for preclinical testing, but the drawbacks are that it more closely resembles a model of juvenile onset HD and its very severe symptoms may be more difficult to treat with candidate therapies.

The N171-82Q model provides a compromise between adult symptom onset and a tractable experimental time frame. However, unlike most HD transgenic models, which are under the control of the human or mouse Htt promoter, transgene expression in the N171-82Q line is driven by the prion protein promoter. While the Htt promoter drives evenly distributed, ubiquitous expression, the prion protein promoter results in ~8-fold higher transgene expression in the cerebellum, leading to cerebellar inclusion formation at a much younger age than forebrain inclusion formation (Harper et al., 2005). Thus, cerebellar pathology could underlie some of the motor deficits in these mice.

Full-length Htt transgenic models, such as the YAC128 and BACHD lines, exhibit more human-like, slower, progressive cognitive and motor deficits along with striatal atrophy, ventricular enlargement and some selective loss of MSNs at later stages. However, their motor deficits are quite mild compared to those seen with the N-terminal fragment models, making it difficult to achieve statistically significant therapeutic effects and, unlike in the human disease, the YAC128 and BACHD mice gain, rather than lose, weight during disease progression (Slow et al., 2003; Van Raamsdonk et al., 2005; Gray et al., 2008). The background strain of these models, the FVB/N line, is also subject to retinal degeneration confounding late stage behavior testing (Taketo, 1991).

Models of HD induced by viral vectors coding for mHtt, such as the lentiviral model, exhibit the striatal neuron loss characteristic of human HD, which makes these models very attractive for studying this key aspect of the HD phenotype. However, these animals show only mild motor deficits and no change in body weight (De Almeida et al., 2002; Regulier et al., 2003).

Rat models are limited, including neurotoxin and lentivirus-induction models (De Almeida et al., 2002) and a single transgenic with onset at greater than 12 months (von Hörsten et al., 2003). All of the rodent models have the drawbacks that brain size is too small to employ gene therapy delivery techniques valid to human HD, as well as the lack of separation of the caudate and putamen, as is the case in humans.

The newly developed sheep transgenic model has the benefits of being a fairly inexpensive genetic model with brain size and morphology much more

similar to humans than rodents (Snell et al., 2008). However, the lack of established sheep behavioral tests and facilities for the care of late stage disease make this model most appropriate for histological studies of the pre-symptomatic and early disease stages. Reduction of dopamine- and cyclic AMP-regulated phosphoprotein (DARPP-32) immunostaining, a marker of healthy MSNs that is diminished in the striatum of HD postmortem brains (Rudnicki et al., 2008), has been observed in these animals prior to motor symptoms. The founders have not yet reached symptomatic onset, so the extent or existence of motor deficit and neurodegeneration is unknown.

Non-human primate models obviously share the most morphological and behavioral homology with humans. However, studies with NHPs are expensive and, until very recently, only neurotoxin and viral-induction models of HD were available. Neurotoxin models are not useful for therapies directed at the mHtt protein rather than downstream non-specific effects of toxicity. Viral-induction models are spatially and temporally limited, thus incapable of fully recapitulating human HD. Thus, it is important that a NHP transgenic model is currently being developed. Preliminary studies indicate behavior and neuropathology similar to human HD (Yang et al., 2008). This model has the potential to be very informative and predictive for pre-clinical trials.

There are many cellular aspects of mHtt toxicity. For instance, it disrupts transcriptional regulation, an example of which is dysregulation of CBP, a protein that acetylates histones (Steffan et al., 2001). Treatment with histone deacetyase (HDAC) inhibitors induces postitive effects in cell culture, *Drosophila* and

transgenic mouse HD models (McCampbell et al., 2001; Ferrante et al., 2003). However, toxicity of broad-spectrum HDAC inhibitors has previously limited their therapeutic potential. Recently, isotype-specific HDAC inhibitors, which should have fewer side effects, have been validated in *Drosophila* and transgenic mouse HD models (Pallos et al., 2008; Thomas et al., 2008). A phase I clinical trial of an isotype-specific HDAC inhibitor for the treatment of cancer showed safety and tolerability (Siu et al., 2008).

Another example of transcriptional dysregulation in HD is repression of brain derived neurotrophic factor (BDNF) expression. BDNF is produced by cortical neurons and is required for striatal neuron survival (Zuccato et al., 2001). Over-expression of BDNF or glial derived neurotrophic factor (GDNF) in the rat brain is neuroprotective in an excitotoxic HD model (Kells et al., 2004). Upregulating BDNF in HD mice with ampakine treatemnt, a positive modulator of AMPA receptors, rescues synaptic plasticity and improves long-term memory deficits (Simmons et al., 2009). Interestingly, cystamine, a transglutaminase inhibitor originally thought to reduce mHtt-induced toxicity by preventing cross-linking of expanded polyQ molecules, increases BDNF secretion in the brain of HD model mice and in the serum of mouse and non-human primate models (Borrell-Pagès et al., 2006). A phase I clinical trial of cysteamine treatment, the FDA-approved, reduced form of cystamine, shows safety and tolerability (Dubinsky and Gray, 2006).

mHtt also disrupts glutamate uptake (Behrens et al., 2002), N-methyl-D-aspartate receptor (NMDAR) signaling (Zeron et al., 2002), and mitochondrial

regulation and metabolism resulting in excitotoxicity and oxidative damage. NMDAR antagonist treatment improves survival and body weight in HD mice, but not motor symptoms (Schiefer et al., 2002). Combinatorial treatment with an NMDAR antagonist and a mitochondrial anti-oxidant, coenzyme Q_{10}, improves survival, motor deficit and ventricular enlargement of HD model mice (Ferrante et al., 2002). However, a phase I clinical trial showed no effect on disease progression (Huntington Study Group, 2001), further supporting the idea that beneficial results in a single mouse model of HD are not a valid predictor of clinical efficacy. Other mitochondrial modifiers such as minocycline, which decreases mitochondrial permeability, and creatine, which increases mitochondrial stability, have neuroprotective effects (Ferrante et al., 2000; Andreassen et al., 2001; Wang et al., 2003b). Both were safe and tolerated in clinical trials and modest beneficial effects were reported (Bonelli et al., 2004; Hersch et al., 2006). A recent high throughput screen for small molecules that inhibit mHtt-induced neuronal death showed that inhibition of mitochondrial functions, including electron transport but also coupling and general metabolism, is sufficient to rescue cell death (Varma et al., 2007). Mutant Htt represses transcription of PGC-1α, a regulator of mitochondrial metabolism, which when delivered by lentivirus to the striatum of transgenic HD model mice, prevents neuronal atrophy (Cui et al., 2006).

There may be advantages in terms of specificity and efficacy in directing therapy towards the most upstream HD targets. An obvious approach of this type is to reduce the level of mHtt protein itself, either by gene silencing or through

increased clearance. RNAi silencing of mHtt with shRNAs or siRNAs can knock down mHtt expression and improve HD phenotype in three different transgenic HD mouse models (Harper et al., 2005; Rodriguez-Lebron et al., 2005; DiFiglia et al., 2007). Both viral-mediated delivery of RNAs and direct neuronal uptake of cholesterol-conjugated RNAs have been reported. One caveat of this approach is that current RNAis cannot distinguish between expanded and normal polyQ stretches and therefore do not differentiate between wild type (wt) and mHtt. They can, however, target human Htt versus mouse Htt. As a result, endogenous wtHtt is not silenced in these models although it would be in human HD applications. Conditional knockout of wtHtt in adult mice results in progressive neurodegeneration (Dragatsis et al., 2000), indicating that silencing of wtHtt may not be tolerated. A new study reports that reduction of mouse wtHtt levels by up to 80% for up to four months has no negative effects while this same reduction in mHtt levels has dramatic beneficial effects (Boudreau et al., 2009), arguing that non-allele-specific silencing of Htt in human HD would therefore be a viable strategy.

The general resistance to Htt-associated neurodegeneration in the mouse brain should also be considered, however. If sensitivity to Htt-associated neuropathology were similar between mice and humans, heterozygous knock-in HD mice with polyQ lengths equivalent to those seen in patients would model human HD fairly closely. In actuality, these mice have no HD-related phenotype (White et al., 1997), and in order to model human HD in mice, polyQ expansions lengths well above those seen in humans are used, often in the context of a

highly toxic N-terminal fragment. For this reason, development of allele-specific RNAi is preferable. This could be accomplished using single nucleotide polymorphisms (SNPs), as has been demonstrated for spinocerebellar ataxia type 3 (Miller et al., 2003). However, this method would likely require generation of custom siRNAs for each patient based on SNP composition. A recent report indicates that a large percentage of HD gene positive individuals could be treated using a small panel of SNPs that are significantly enriched in HD patients of European descent (Warby et al., 2009). However, this approach, still in its infancy, would not be useful for a large number of patients.

A different strategy for reducing mHtt levels involves induction of autophagy. Autophagy is a non-specific degradation process for long-lived and mis-folded cytoplasmic proteins. Induction of autophagy by rapamycin, valproate or trehalose results in accelerated clearance of mHtt and subsequent therapeutic benefit in fly and mouse HD models (Ravikumar et al., 2004; Sarkar et al., 2007). Though wtHtt levels are not affected by this strategy, it is not specific to Htt and could potentially have off-target effects. Ideally, therapeutic action should be specific to the mHtt protein. This is why we are exploring the use of an antibody-based approach.

REFERENCES

The Huntington's Disease Collaborative Research Group. (1993) A novel gene containing a trinucleotide repeat that is expanded and unstable on Huntington's disease chromosomes. Cell 72:971-983.

Andreassen OA, Dedeoglu A, Ferrante RJ, Jenkins BG, Ferrante KL, Thomas M, Friedlich A, Browne SE, Schilling G, Borchelt DR, Hersch SM, Ross CA, Beal MF (2001) Creatine increase survival and delays motor symptoms in a transgenic animal model of Huntington's disease. Neurobiology of disease 8:479-491.

Behrens PF, Franz P, Woodman B, Lindenberg KS, Landwehrmeyer GB (2002) Impaired glutamate transport and glutamate-glutamine cycling: downstream effects of the Huntington mutation. Brain 125:1908-1922.

Bonelli RM, Hödl AK, Hofmann P, Kapfhammer H-P (2004) Neuroprotection in Huntington's disease: a 2-year study on minocycline. International clinical psychopharmacology 19:337-342.

Borrell-Pagès M, Canals JM, Cordelières FP, Parker JA, Pineda JR, Grange G, Bryson EA, Guillermier M, Hirsch E, Hantraye P, Cheetham ME, Néri C, Alberch J, Brouillet E, Saudou F, Humbert S (2006) Cystamine and cysteamine increase brain levels of BDNF in Huntington disease via HSJ1b and transglutaminase. The journal of clinical investigation 116:1410-1424.

Boudreau R, McBride J, Martins I, Shen S, Xing Y, Carter B, Davidson BL (2009) Nonallele-specific Silencing of Mutant and Wild-type Huntingtin

Demonstrates Therapeutic Efficacy in Huntington. Molecular therapy 17:1053-1063.

Carter RJ, Lione LA, Humby T, Mangiarini L, Mahal A, Bates GP, Dunnett SB, Morton AJ (1999) Characterization of progressive motor deficits in mice transgenic for the human Huntington's disease mutation. The journal of neuroscience 19:3248-3257.

Cui L, Jeong H, Borovecki F, Parkhurst CN, Tanese N, Krainc D (2006) Transcriptional repression of PGC-1alpha by mutant huntingtin leads to mitochondrial dysfunction and neurodegeneration. Cell 127:59-69.

David G, Abbas N, Stevanin G, Durr A, Yvert G, Cancel G, Weber C, Imbert G, Saudou F, Antoniou E, Drabkin H, Gemmill R, Giunti P, Benomar A, Wood N, Ruberg M, Agid Y, Mandel J-L, Brice A (1997) Cloning of the SCA7 gene reveals a highly unstable CAG repeat expansion. Nature genetics 17:65-70.

De Almeida LP, Ross CA, Zala D, Aebischer P, Deglon N (2002) Lentiviral-Mediated delivery of mutant huntingtin in the striatum of rats induces a selective neuropathology modulated by polyglutamine repeat size, huntingtin expression levels, and protein length. The journal of neuroscience 22:3473-3483.

DiFiglia M, Sena-Esteves M, Chase K, Sapp E, Pfister E, Sass M, Yoder J, Reeves P, Pandey RK, Rajeev KG, Manoharan M, Sah DWY, Zamore PD, Aronin N (2007) Therapeutic silencing of mutant huntingtin with siRNA attenuates striatal and cortical neuropathology and behavioral deficits.

Proceedings of the national academy of sciences of the United States of America 104:17204-17209.

Dragatsis I, Levine MS, Zeitlin S (2000) Inactivation of Hdh in the brain and testis results in progressive neurodegeneration and sterility in mice. Nature genetics 26:300-306.

Dubinsky R, Gray C (2006) CYTE-I-HD: phase I dose finding and tolerability study of cysteamine (Cystagon) in Huntington's disease. Movement disorders 21:530-533.

Ehrnhoefer DE, Butland SL, Pouladi MA, Hayden MR (2009) Mouse models of Huntington disease: variations on a theme. Disease models & mechanisms 2:123-129.

Ferrante RJ, Andreassen OA, Dedeoglu A, Ferrante KL, Jenkins BG, Hersch SM, Beal MF (2002) Therapeutic effects of coenzyme Q10 and remacemide in transgenic mouse models of Huntington's disease. The journal of neuroscience 22:1592-1599.

Ferrante RJ, Andreassen OA, Jenkins BG, Dedeoglu A, Kuemmerle S, Kubilus JK, Kaddurah-Daouk R, Hersch SM, Beal MF (2000) Neuroprotective effects of creatine in a transgenic mouse model of Huntington's disease. The journal of neuroscience 20:4389-4397.

Ferrante RJ, Kubilus JK, Lee J, Ryu H, Beesen A, Zucker B, Smith K, Kowall NW, Ratan RR, Luthi-Carter R, Hersch SM (2003) Histone deacetylase inhibition by sodium butyrate chemotherapy ameliorates the

neurodegenerative phenotype in Huntington's disease mice. The journal of neuroscience 23:9418-9427.

Graham RK, Deng Y, Slow EJ, Haigh B, Bissada N, Lu G, Pearson J, Shehadeh J, Bertram L, Murphy Z, Warby SC, Doty CN, Roy S, Wellington CL, Leavitt BR, Raymond LA, Nicholson DW, Hayden MR (2006) Cleavage at the caspase-6 Site Is required for neuronal dysfunction and degeneration due to mutant huntingtin. Cell 125:1179-1191.

Gray M, Shirasaki DI, Cepeda C, André VM, Wilburn B, Lu X-H, Tao J, Yamazaki I, Li S-H, Sun YE, Li X-J, Levine MS, Yang XW (2008) Full-length human mutant huntingtin with a stable polyglutamine repeat can elicit progressive and selective neuropathogenesis in BACHD mice. The journal of neuroscience 28:6182-6195.

Huntington Study Group HS (2001) A randomized, placebo-controlled trial of coenzyme Q10 and remacemide in Huntington's disease. Neurology 57:397-404.

Huntington Study Group HS (2006) Tetrabenazine as antichorea therapy in Huntington disease: a randomized controlled trial. Neurology 66.

Harper SQ, Staber PD, He X, Eliason SL, Martins IH, Mao Q, Yang L, Kotin RM, Paulson HL, Davidson BL (2005) From the Cover: RNA interference improves motor and neuropathological abnormalities in a Huntington's disease mouse model. Proceedings of the national academy of sciences of the United States of America 102:5820-5825.

Hersch SM, Gevorkian S, Marder K, Moskowitz C, Feigin A, Cox M, Como P, Zimmerman C, Lin M, Zhang L, Ulug AM, Beal MF, Matson W, Bogdanov M, Ebbel E, Zaleta A, Kaneko Y, Jenkins B, Hevelone N, Zhang H, Yu H, Schoenfeld D, Ferrante R, Rosas HD (2006) Creatine in Huntington disease is safe, tolerable, bioavailable in brain and reduces serum 8OH2'dG. Neurology 66:250-252.

Imbert G, Saudou F, Yvert G, Devys D, Trottier Y, Garnier J-M, Weber C, Mandel J-L, Cancel G, Abbas N, Durr A, Didierjean O, Stevanin G, Agid Y, Brice A (1996) Cloning of the gene for spinocerebellar ataxia 2 reveals a locus with high sensitivity to expanded CAG/glutamine repeats. Nature genetics 14:285-291.

Kawaguchi Y, Okamoto T, Taniwaki M, Aizawa M, Inoue M, Katayama S, Kawakami H, Nakamura S, Nishimura M, Akiguchi I, Kimura J, Narumiya S, Kakizuka A (1994) CAG expansions in a novel gene for Machado-Joseph disease at chromosome 14q32.1. Nature genetics 8:221-228.

Kells APAP, Fong DMDM, Dragunow MM, During MJMJ, Young DD, Connor BB (2004) AAV-mediated gene delivery of BDNF or GDNF is neuroprotective in a model of Huntington disease. Molecular therapy 9:682-688.

Koide R, Ikeuchi T, Onodera O, Tanaka H, Igarashi S, Endo K, Takahashi H, Kondo R, Ishikawa A, Hayashi T, Saito M, Tomoda A, Miike T, Naito H, Ikuta F, Tsuji S (1994) Unstable expansion of CAG repeat in hereditary dentatorubral-pallidoluysian atrophy (DRPLA). Nature genetics 6:9-13.

Lione LA, Carter RJ, Hunt MJ, Bates GP, Morton AJ, Dunnett SB (1999) Selective discrimination learning impairments in mice expressing the human Huntington's disease mutation. The journal of neuroscience 19:10428-10437.

Mangiarini L, Sathasivam K, Seller M, Cozens B, Harper A, Hetherington C, Lawton M, Trottier Y, Lehrach H, Davies SW, Bates GP (1996) Exon 1 of the HD gene with an expanded CAG repeat is sufficient to cause a progressive neurological phenotype in transgenic mice. Cell 87:493-506.

Marsh JL, Walker H, Theisen H, Zhu Y-Z, Fielder T, Purcell J, Thompson LM (2000) Expanded polyglutamine peptides alone are intrinsically cytotoxic and cause neurodegeneration in Drosophila. Human molecular genetics 9:13-25.

McCampbell A, Taye AA, Whitty L, Penney E, Steffan JS, Fischbeck KH (2001) Histone deacetylase inhibitors reduce polyglutamine toxicity. Proceedings of the national academy of sciences of the United States of America 98:15179-15184.

Miller VM, Xia H, Marrs GL, Gouvion CM, Lee G, Davidson BL, Paulson HL (2003) Allele-specific silencing of dominant disease genes. Proceedings of the national academy of sciences of the United States of America 100:7195-7200.

Nakamura KK, Aminoff MJMJ (2007) Huntington's disease: clinical characteristics, pathogenesis and therapies. Medicamentos de actualidad 43:97-116.

Orr HT, Chung M-y, Banfi S, Kwiatkowski TJ, Servadio A, Beaudet AL, McCall AE, Duvick LA, Ranum LPW, Zoghbi HY (1993) Expansion of an unstable trinucleotide CAG repeat in spinocerebellar ataxia type 1. Nature genetics 4:221-226.

Pallos J, Bodai L, Lukacsovich T, Purcell JM, Steffan JS, Thompson LM, Marsh JL (2008) Inhibition of specific HDACs and sirtuins suppresses pathogenesis in a Drosophila model of Huntington's disease. Human molecular genetics 17:3767-3775.

Ramaswamy SS, Shannon KMKM, Kordower JHJH (2007) Huntington's disease: pathological mechanisms and therapeutic strategies. Cell transplantation 16:301-312.

Ravikumar B, Vacher C, Berger Z, Davies JE, Luo S, Oroz LG, Scaravilli F, Easton DF, Duden R, O'Kane CJ, Rubinsztein DC (2004) Inhibition of mTOR induces autophagy and reduces toxicity of polyglutamine expansions in fly and mouse models of Huntington disease. Nature genetics 36:585-595.

Regulier E, Trottier Y, Perrin V, Aebischer P, Deglon N (2003) Early and reversible neuropathology induced by tetracycline-regulated lentiviral overexpression of mutant huntingtin in rat striatum. Human molecular genetics 12:2827-2836.

Rodriguez-Lebron E, Denovan-Wright EM, Nash K, Lewin AS, Mandel RJ (2005) Intrastriatal rAAV-mediated delivery of anti-huntingtin shRNAs induces

partial reversal of disease progression in R6/1 Huntington's disease transgenic mice. Molecular therapy 12:618-633.

Rosas D, Salat D, Lee S, Zaleta A, Hevelone N, Hersch SM (2008) Complexity and heterogeneity: what drives the ever-changing brain in Huntington's disease? Annals of the New York academy of sciences 1147:196-205.

Sarkar S, Davies JE, Huang Z, Tunnacliffe A, Rubinsztein DC (2007) Trehalose, a novel mTOR-independent autophagy enhancer, accelerates the clearance of mutant huntingtin and alpha-synuclein. The journal of biological chemistry 282:5641-5652.

Schiefer J, Landwehrmeyer GB, Lüesse H-G, Sprünken A, Puls C, Milkereit A, Milkereit E, Kosinski CM (2002) Riluzole prolongs survival time and alters nuclear inclusion formation in a transgenic mouse model of Huntington's disease. Movement disorders 17:748-757.

Schilling G, Becher MW, Sharp AH, Jinnah HA, Duan K, Kotzuk JA, Slunt HH, Ratovitski T, Cooper JK, Jenkins NA, Copeland NG, Price DL, Ross CA, Borchelt DR (1999) Intranuclear inclusions and neuritic aggregates in transgenic mice expressing a mutant N-terminal fragment of huntingtin. Human molecular genetics 8:397-407.

Simmons D, Rex C, Palmer L, Pandyarajan V, Fedulov V, Gallb C, Lynch G (2009) Up-regulating BDNF with an ampakine rescues synaptic plasticity and memory in Huntington’s disease knockin mice. Proceedings of the national academy of sciences of the United States of America 106:4906-4911.

Siu LL, Pili R, Duran I, Messersmith WA, Chen EX, Sullivan R, MacLean M, King S, Brown S, Reid GK, Li Z, Kalita AM, Laille EJ, Besterman JM, Martell RE, Carducci MA (2008) Phase I study of MGCD0103 given as a three-times-per-week oral dose in patients with advanced solid tumors. Journal of clinical oncology 26:1940-1947.

Slow EJ, van Raamsdonk J, Rogers D, Coleman SH, Graham RK, Deng Y, Oh R, Bissada N, Hossain SM, Yang Y-Z, Li X-J, Simpson EM, Gutekunst C-A, Leavitt BR, Hayden MR (2003) Selective striatal neuronal loss in a YAC128 mouse model of Huntington disease. Human molecular genetics 12:1555-1567.

Snell RG, Jacobsen JC, Waldvogel HJ, Reid SJ, Bawden CS, S. R, MacDonald ME, Gusella JF, Rees MI, Faull RLM (2008) HD transgenic sheep model. Heriditary disease foundation annual meeting abstract.

Spada ARL, Wilson EM, Lubahn DB, Harding AE, Fischbeck KH (1991) Androgen receptor gene mutations in X-linked spinal and bulbar muscular atrophy. Nature 352:77-79.

Steffan JS, Bodai L, Pallos J, Poelman M, McCampbell A, Apostol BL, Kazantsev A, Schmidt E, Zhu YZ, Greenwald M, Kurokawa R, Housman DE, Jackson GR, Marsh JL, Thompson LM (2001) Histone deacetylase inhibitors arrest polyglutamine-dependent neurodegeneration in Drosophila. Nature 413:739-743.

Thomas EA, Coppola G, Desplats PA, Tang B, Soragni E, Burnett R, Gao F, Fitzgerald KM, Borok JF, Herman D, Geschwind DH, Gottesfeld JM (2008)

The HDAC inhibitor 4b ameliorates the disease phenotype and transcriptional abnormalities in Huntington's disease transgenic mice. Proceedings of the national academy of sciences of the United States of America 105:15564-15569.

Van Raamsdonk JM, Pearson J, Slow EJ, Hossain SM, Leavitt BR, Hayden MR (2005) Cognitive dysfunction precedes neuropathology and motor abnormalities in the YAC128 mouse model of Huntington's disease. The journal of neuroscience 25:4169-4180.

Varma H, Cheng R, Voisine C, Hart AC, Stockwell BR (2007) Inhibitors of metabolism rescue cell death in Huntington's disease models. Proceedings of the national academy of sciences of the United States of America 104:14525-14530.

von Hörsten S, Schmitt I, Nguyen HP, Holzmann C, Schmidt T, Walther T, Bader M, Pabst R, Kobbe P, Krotova J, Stiller D, Kask A, Vaarmann A, Rathke-Hartlieb S, Schulz JB, Grasshoff U, Bauer I, Vieira-Saecker AMM, Paul M, Jones L, Lindenberg KS, Landwehrmeyer B, Bauer A, Li X-J, Riess O (2003) Transgenic rat model of Huntington's disease. Human molecular genetics 12:617-624.

Wang X, Zhu S, Drozda M, Zhang W, Stavrovskaya IG, Cattaneo E, Ferrante RJ, Kristal BS, Friedlander RM (2003) Minocycline inhibits caspase-independent and -dependent mitochondrial cell death pathways in models of Huntington's disease. Proceedings of the national academy of sciences of the United States of America 100:10483-10487.

White JK, Auerbach W, Duyao MP, Vonsattel JP, Gusella JF, Joyner AL, MacDonald ME (1997) Huntingtin is required for neurogenesis and is not impaired by the Huntington's disease CAG expansion. Nature genetics 17:404-410.

Yang S-H, Cheng P-H, Banta H, Piotrowska-Nitsche K, Yang J-J, Cheng ECH, Snyder B, Larkin K, Liu J, Orkin J, Fang Z-H, Smith Y, Bachevalier J, Zola SM, Li S-H, Li X-J, Chan AWS (2008) Towards a transgenic model of Huntington's disease in a non-human primate. Nature 453:921-924.

Yang W, Dunlap JR, Andrews RB, Wetzel R (2002) Aggregated polyglutamine peptides delivered to nuclei are toxic to mammalian cells. Human molecular genetics 11:2905-2917.

Zeron MM, Hansson O, Chen N, Wellington CL, Leavitt BR, Brundin P, Hayden MR, Raymond LA (2002) Increased sensitivity to N-methyl-D-aspartate receptor-mediated excitotoxicity in a mouse model of Huntington's disease. Neuron 33:849-860.

Zuccato C, Ciammola A, Rigamonti D, Leavitt BR, Goffredo D, Conti L, MacDonald ME, Friedlander RM, Silani V, Hayden MR, Timmusk T, Sipione S, Cattaneo E (2001) Loss of huntingtin-mediated BDNF gene transcription in huntington's disease. Science 293:493-498.

Chapter 2

Intrabodies binding the proline-rich domains of mutant huntingtin increase its turnover and reduce neurotoxicity

Southwell AL, Khoshnan A, Dunn DE, Bugg CW, Lo DC, Patterson PH
J Neurosci. 2008, 28(36): 9013-20.

INTRODUCTION

The first exon of Htt consists of 17 N-terminal amino acids (AAs) followed by the polyQ tract, the PRR, which consists of two polyP stretches that are separated by a P-rich domain, and 13 additional AAs (Fig.1A). The non-polyQ domains in HDx-1 are known to modulate the toxicity of the mutant protein, although the mechanisms by which this occurs are not well understood (Duennwald et al., 2006). Understanding how these non-polyQ domains contribute to the toxicity and cellular specificity of mHtt could lead to new therapeutic strategies.

Classically, the function of a protein domain would be studied by removal of that domain followed by functional testing. Although a great deal of knowledge has been acquired through such methods, the deletion of a domain may cause altered folding of the remaining protein or otherwise generate effects not related directly to the function of the missing domain. Perturbation of a protein domain by intrabody (iAb) binding is a more specific method for exploring function. Intrabodies are intracellular, recombinant, single chain antibody fragments (scFv) that contain the heavy and light antigen-binding domains (V_H and V_L) connected by a linker. Alternatively, single domain antibody fragments consist of either V_H or V_L. Intrabodies are highly specific reagents that can be targeted to sub-cellular

compartments, distinct protein conformations, post-transcriptional modifications, as well as to non-protein targets such as oligosaccharides (Biocca and Cattaneo, 1995; Stocks, 2005; Messer and McLear, 2006; Lo et al., 2008). Intrabodies therefore have great potential to increase our understanding of the functions of individual protein domains in living cells.

We sought to use iAbs to investigate the role of the PRR of Htt in HD pathology, and to explore their efficacy as possible HD therapeutics. The PRR is known to be important for mHtt toxic gain of function (Passani et al., 2000; Steffan et al., 2000; Modregger et al., 2002; Khoshnan et al., 2004; Qin et al., 2004), and although a number of PRR binding partners, including WW domain-containing proteins, vesicle-associated proteins, P53, and IKKγ, have been identified, the mechanism of the modulation of mHtt toxicity by the PRR domains remains unclear. To investigate the role of the polyP stretches of the PRR domain we used MW7(Ko et al., 2001), a scFv iAb that binds polyP. MW7 reduces mHtt-induced aggregation and promotes cell survival in culture (Khoshnan et al., 2002). It also inhibits mHtt-induced neurodegeneration in a *Drosophila* HD model (Jackson et al., 2004). However, the specificity of this iAb for pure polyP could allow binding to other cellular proteins containing a polyP domain, although there is no evidence of the latter binding to date using immunoblotting. To characterize the role of the P-rich stretch of the PRR, we produced novel iAbs (Happs) against the P-rich domain of Htt. Happ1 and 3 are single domain, light chain iAbs (V_Ls) that bind mHtt in a PRR-dependent manner. We then tested the Happs, MW7 and V_L12.3, a single domain light chain iAb that

binds the 17 N terminal AAs of Htt (Colby et al., 2004b), for efficacy in blocking mHDx-1 aggregation and toxicity in dissociated cell culture as well as in brain slice cultures. We also examined their effects on the level of mHDx-1 and its sub-cellular localization. The most striking findings are that both the anti-polyP and anti-P-rich iAbs reduce toxicity by increasing mHtt turnover and lowering mHtt level, while the anti-N-terminal iAb appears to reduce mHtt toxicity by a different mechanism.

RESULTS

Isolation of Happ intrabodies. Novel iAbs against the PRR domain were selected in a two-stage protocol. First, a non-immune, human, recombinant scFv phage library (Griffin.1)(Griffiths et al., 1994) was used and clones were selected that bind a unique, P-rich sequence between the two polyP domains in mHDx-1. The second stage involved three rounds of selection using mHDx-1Q50 (Scherzinger et al., 1997). Following the second stage, individual clones were analyzed for inserts containing open reading frames (ORFs). Although the Griffin.1 library consists of full scFv fragments, the two clones selected had only the V_L ORFs. A control V_L that does not bind Htt (CV_L) was also isolated from the library. These three V_Ls (Happ1, Happ3 and CV_L) were then inserted into a mammalian expression vector for cell culture and brain slice studies. To verify the specificity of these iAbs, they were expressed as glutathione-s-transferase (GST) fusion proteins and used as primary antibodies to stain lysates of 293 cells transfected with HDx1 or HDx1ΔPRR. The lysates of non-transfected cells were

used to test for binding non-Htt cellular proteins (Fig. 1B). As expected, MW7 and the Happs bind only to HDx1 containing the PRR, while V_L12.3 binds both forms of HDx1. None of these iAbs bind the non-transfected lysates. These results confirm that the Happs require the Htt PRR epitope for binding.

The intrabodies reduce mHDx-1 aggregation and toxicity. Each of the iAbs was tested at various ratios to mHDx-1 (0.5:1, 1:1, 2:1, 3:1, and 4:1) for effects on mHDx-1 toxicity by counting ethidium homodimer-2 (EthHD-2)-positive dead cell nuclei (Fig. 2A), and aggregation by counting green foci of the HDx-1-green fluorescent protein (GFP) fusion protein (Fig. 2B). While V_L12.3, Happ1 and Happ3 reduce aggregation in a dose-dependent, saturable manner, MW7 displays a threshold effect, requiring a 4:1 ratio to mHtt for effect. This may be the result of its specificity for pure polyP. As there are two polyP stretches that can each likely accommodate binding of two iAb molecules, reduction of aggregation by polyP binding may require complete blockade of these epitopes. As with aggregation, V_L12.3 is also the most effective iAb in reducing toxicity, with an optimal ratio to mHDx-1 of 1:1. MW7 is optimal at a ratio of 4:1, while Happ1 and 3 each show an optimal ratio of 2:1, with significant beneficial effects at 1:1. Similar effects on mHDx-1-induced toxicity are seen when measuring lactate dehydrogenase (LDH) activity released into the culture supernatant (data not shown). These results confirm previous findings with iAbs against the N1-17 AA epitope (Colby et al., 2004b), and further demonstrate that the PRR also modulates HDx1 toxicity. As expected, CV_L has no dose-dependent effects on mHtt-induced toxicity or aggregation.

The anti-Htt intrabodies reduce mHDx-1-induced neurodegeneration in a cortico-striatal brain slice model of HD. Rat brain slices, which preserve much of the intrinsic circuitry, were biolistically co-transfected with yellow fluorescent protein (YFP), mHDx-1-cyan fluorescent protein (CFP) and an iAb. Four-5 days after slice preparation and transfection, the number of morphologically healthy, transfected MSNs in the striatum of each slice was then assessed using YFP fluorescence as an independent reporter of cell type and vitality (Fig. 3). The number of healthy MSNs per brain slice was compared between iAb controls (brain slices transfected with YFP + CV_L and slices transfected with YFP + mHDx-1 + CV_L), a negative control (transfected with YFP + mHDx-1 + vector backbone DNA), and the test condition transfected with YFP + mHDx-1 + anti-Htt iAb). Compared to transfection with YFP + CV_L, co-transfection of mHDx-1 with CV_L, results in a significant reduction in healthy MSNs. In contrast, co-transfection of mHDx-1 with V_L12.3 or Happ1 results in numbers of healthy MSNs that are similar to slices transfected with YFP + CV_L (Fig. 3A). Co-transfection of slices with mHDx-1 + MW7 yields intermediate results, with significantly greater numbers of healthy MSNs than with mHDx-1 + CV_L, but fewer than with YFP + CV_L (Fig. 3B). These results extend the findings from 293 cells to MSNs in a semi-intact milieu.

V_L12.3 alters cytoplasmic vs. nuclear localization of mHDx-1. To evaluate the effect of the iAbs on HDx-1 intracellular localization, ST14A striatal neuronal precursor cells (Cattaneo and Conti, 1998) were co-transfected with mHDx-1-GFP and iAb and incubated for 48 hours. Cells were fixed, stained for

both iAb and nuclei, and then analyzed by confocal microscopy. GFP fluorescence intensity was used to compare levels of mHDx-1 in the whole cell vs. the nucleus (Fig. 4). The anti-PRR iAbs do not alter the cytoplasmic/nuclear mHDx-1 ratio, while V_L12.3 causes a significant increase of nuclear Htt (Fig. 4B). In terms of localization of the iAbs themselves, V_L12.3, Happ1 and Happ3 display a slight preference for the nucleus while MW7 is slightly more cytoplasmic (Fig. 4C). This could be the result of the larger size of the MW7 scFv compared to the single domain iAbs. No significant differences are seen between V_L12.3, Happ1 and Happ3, and the slight preference of V_L12.3 for the nucleus is too small to account for the increased nuclear HDx-1 in the presence of V_L12.3, indicating that this change in localization is not the result of the iAb itself targeting the nucleus. Thus, iAb binding to the N-terminus of Htt disrupts cytoplasmic vs. nuclear trafficking of Htt, which may influence its nuclear functions. Since the amount of nuclear mHtt correlates with toxicity (Truant et al., 2007), this result suggests that V_L12.3 may not be ideal as a therapeutic iAb despite its clear effects on blocking mHtt toxicity.

The intrabodies differentially alter the level of soluble mHDx-1. To determine the effects of the intrabodies on mHDx-1 levels, 293 cells were co-transfected with iAb and either wtHDx-1 or mHDx-1, using each iAb at its optimal ratio to HDx-1, and incubated for 48 hrs. Soluble and insoluble cell fractions were then assayed for HDx-1 by immunoblotting and densitometery (Fig. 5). Each of the iAbs dramatically reduces the level of insoluble mHDx-1. However, the three anti-PRR iAbs (MW7, Happ1, Happ3) also significantly reduce the level of

soluble mHDx-1, while V_L12.3 has no significant effect on soluble mutant or wtHDx-1 levels. From a therapeutic standpoint, it is important that only a slight reduction of wtHDx-1 protein is seen, indicating that anti-PRR iAbs are selective for the mutant form. Although these iAbs bind wtHDx-1, their preference for the mutant form is not unexpected as the interaction of endogenous Htt PRR-binding partners with Htt is known to increase with increasing polyQ repeat length (Passani et al., 2000; Holbert et al., 2001).

The anti-PRR intrabodies increase mHDx-1 turnover. To further investigate the reduction of soluble mHDx-1 a SNAP tag fusion labeling experiment was performed (Jansen et al., 2007). A traditional pulse chase experiment was not used because mHDx-1 is known to affect transcriptional regulation. This property of mHDx-1 could conceivably be altered by iAb binding leading to variable transcription rates of HDx-1 in the presence of the various iAbs. Traditional pulse-chase experiments require equal transcription and translation of the target protein in all conditions within the labeling period. The SNAP tag fusion system allows labeling of all pre-existing HDx-1. By measuring the amount of Htt at the time of labeling and again at a later time point, we are able to measure a rate of turnover independent of transcription or translation rate. This system also offers greater specificity as only the SNAP tag fusion protein is labeled as opposed to all cellular proteins translated during the labeling period as with traditional pulse-chase experiments.

To investigate HDx-1 turnover using the SNAP tag fusion system, 293 cells were co-transfected with iAb and HDX-1 fused to the SNAP tag. Twenty-

four hours post-transfection, HDx-1 was labeled using a fluorescent, cell permeable SNAP substrate. This substrate undergoes a covalent binding reaction with the SNAP tag and remains fluorescent until the SNAP-tag fusion protein is broken down. Some cultures were immediately examined for HDx-1 levels while others were incubated for 48 hours post-transfection to allow turnover of labeled HDx-1. Fluorescence intensity of HDx-1-SNAP was used to determine the percentage of HDx-1 labeled at 24 hours that is still intact at 48 hours (Fig. 6). Cells transfected with HDx-1-SNAP alone were used to determine a baseline level of turnover. While the percentage of mHDx-1 remaining in the presence of V_L12.3 is equivalent to that in the control, this percentage is significantly reduced in the presence of MW7, Happ1 or Happ3, indicating an increase in the rate of mHDx-1 turnover specifically in the presence of anti-PRR iAbs (Fig. 6B). The lack of effect of V_L12.3 provides a convenient control for non-specific effects of iAb binding to mHDx-1. Although the mechanism by which this increase in mHtt turnover occurs is not yet clear, the levels of iAb protein are increased in the presence of mHtt (data not shown), suggesting that mHtt is not broken down as a part of a complex with iAb. This novel ability of anti-PRR iAbs to increase turnover of mHtt suggests that this region of the protein is important for stability. Further evidence of the specificity of the iAb effects is shown by the fact that none of the anti-Htt iAbs significantly changes the rate of wtHDx-1 turnover (Fig. 6C).

DISCUSSION

While anti-N-terminal and anti-PRR intrabodies ameliorate the negative effects of mHtt in cell culture and brain slice models of HD, they do so with different efficacy and by different mechanisms. These different mechanisms offer clues to the specific functions of their target domains.

The V_L12.3 intrabody was isolated from a yeast surface display library and initially required a 5:1 ratio to mHtt to reduce aggregation (Colby et al., 2004a). It was then re-engineered, including removal of the disulfide bonds, which do not form in the reducing environment of the mammalian cytoplasm (and can cause mis-folding of intrabodies (Biocca et al., 1995)), and mutated for greater binding affinity to Htt (Colby et al., 2004b). In addition to inhibiting mHtt-induced toxicity and aggregation, we find that V_L12.3 also alters cytoplasmic vs. nuclear trafficking of HDx-1.

Modulation of Htt intracellular targeting by the N-terminus has been recently characterized. Removal of this amphipathic alpha helix causes an increase in the level of nuclear Htt, indicating that it functions as a cytoplasmic retention signal (Rockabrand et al., 2007). Mutation of hydrophobic residues, or the introduction of a helix breaking proline residue in the N-terminal domain results in increased nuclear Htt, suggesting that cytoplasmic retention by the N-terminus is the result of association with organelle and vesicle membranes (Atwal et al., 2007). Although the N-terminus is not a dimerization domain, disruption of the helical structure also prevents the aggregation of mHtt, which is accompanied by an increase in the toxicity of the protein. Thus, the N-terminus of Htt is

required for cytoplasmic localization and the formation of aggregates. The effect on toxicity seen in these experiments may be related to the prevention of aggregation, since mHtt-expressing neurons without aggregates exhibit more toxicity than those with aggregates (Arrasate et al., 2004). Toxicity related to the N-terminus may also involve altered Htt localization, as the addition of a nuclear localization signal to mHtt increases its toxicity in both cell culture and mouse models of HD (Peters et al., 1999; Schilling et al., 2004). Interestingly, while removal or mutation of the N-terminus results in increased toxicity, V_L12.3 binding results in reduced toxicity, suggesting that V_L12.3 may inhibit formation of a toxic conformation or an oligomerization seed molecule. Thus, this intrabody may ameliorate toxicity regardless of mHtt localization or aggregation state.

The polyP and P-rich domains of mHtt are implicated in a number of aberrant protein interactions. These domains are required for mHtt binding to, and sequestering of, several SH3 domain-containing proteins, including proteins associated with vesicle function (Modregger et al., 2002; Qin et al., 2004). The PRR of Htt is required for interaction with WW domain-containing proteins (Staub and Rotin, 1996; Faber et al., 1998). These include transcription factors, and these interactions are enhanced with increased polyQ repeat length (Passani et al., 2000; Holbert et al., 2001). These domains are the site of interaction with IKKγ, a regulatory subunit of the IκB kinase complex. Activation of this complex is known to promote aggregation and nuclear localization of mHtt (Khoshnan et al., 2004). The PRR of Htt is also the site of P53 interaction and is required for

transcriptional repression of P53-regulated genes (Steffan et al., 2000). Again, this interaction is enhanced by increased polyQ repeat length.

MW7, an intrabody recognizing pure polyP, reduces mHtt-induced aggregation and toxicity in cell culture and in *Drosophila* models of HD (Khoshnan et al., 2002; Jackson et al., 2004). We find that it is also effective in an acute brain slice model of HD, and that it increases the turnover of HDx-1, with greater effect on the mutant than the wild type form. We also produced novel intrabodies, Happ1 and 3, which recognize the unique, P-rich epitope between the two polyP domains of Htt. The Happ intrabodies exhibit beneficial properties similar to those of MW7 such as preferential effects on the mutant form of Htt and increasing turnover without altering localization, but the Happs are effective at lower ratios to Htt than MW7. We found no evidence that the anti-PRR intrabodies bind to previously aggregated mHtt, suggesting that the observed reduction in aggregation is the indirect result of increased turnover of the soluble form of the protein, causing a shift away from the aggregated state. The increased turnover of mHDx-1 in the presence of either anti-polyP or anti-P-rich intrabodies suggests that this effect is a direct result of blocking these epitopes and therefore that this domain has a role in modulating stability of the mutant protein.

Disruption of mHtt stability by Happ binding could have therapeutic potential. The success of RNAi experiments show that reduction of mHtt levels is an effective therapeutic strategy (Harper et al., 2005; Rodriguez-Lebron et al., 2005; Machida et al., 2006). Unlike RNAi however, these intrabodies can

distinguish between the wt and mutant forms of Htt, which is preferable, as the loss of normal Htt function can have negative effects (Dragatsis et al., 2000; Leavitt et al., 2001; Zuccato et al., 2001). The ability of the Happ intrabodies to increase turnover of mHtt may ameliorate the disruption of the ubiquitin proteasome seen in HD, although it is presently unclear if this increased turnover occurs through a ubiquitin-dependent pathway. As the levels of intrabody protein are increased in the presence of Htt, it is likely that the intrabodies direct the breakdown of mHtt without themselves being degraded. Moreover, the Happs, although significantly more effective than the original intrabody isolated and matured to become V_L12.3, have yet to undergo any re-engineering and could potentially be improved by removal of disulfide bonds and mutation for greater Htt binding affinity. In addition, the present results with the Happ intrabodies highlight the importance of the unique, P-rich domain in mHtt toxicity.

MATERIALS AND METHODS

Cell culture. HEK 293 (ATCC, Manassas, VA) or ST14A striatal precursor cells (Cattaneo and Conti, 1998) were grown in DMEM (Invitrogen, Carlsbad, CA.) supplemented with 10% heat-inactivated fetal bovine serum (FBS), 2 mM glutamine, 1 mM streptomycin and 100 international units of penicillin (Invitrogen). Cells were maintained in 37^{o}C (293) or 33^{o}C (ST14A) incubators with 5% CO_2 (unless otherwise stated). Transfections were performed using lipofectamine 2000 transfection reagent (Invitrogen) according to the manufacturer's protocol.

Immunoblotting. Protein concentration was determined using a BCA assay (Pierce, Rockford IL.). Seventy five μg total protein/sample in a volume of 30 μl was combined with 6 μl 6X protein loading buffer (Ausubel F.M., 1993), and boiled for 5 minutes. Samples were separated by sodium dodecyl sulfate polyacrylamide gel electrophoresis (SDS/PAGE) using 4-20% criterion pre-cast gels (Biorad, Hercules, CA.) and precision plus protein kaleidoscope molecular weight standard (BioRad). Samples were then transferred overnight to nitrocellulose membranes for immunoblotting. Appropriate primary and horseradish peroxidase (HRP)-conjugated secondary antibodies were then applied as described in (Ausubel F.M., 1993). Super signal west dura (Pierce) substrate was applied to membranes according to the manufacturer's protocol. Chemiluminescence was detected and densitometry was performed using a Fluorchem 8900 (Alpha Innotech, San Leandro CA.) gel doc system.

Selection of clones from phage display library for binding to P-rich epitope of Htt. Intrabodies were selected from the Griffin.1 human recombinant, scFv phage display library (Griffiths et al., 1994). One well of a six well plate was coated with a synthetic peptide (200 μg /ml) derived from the P-rich epitope of Htt (PQLPQPPPQAQP) located between the two poly P stretches by incubating at 4^{o}C overnight**.** Following the provider's instructions, the coated well was then used to select phage expressing intrabodies specific for this epitope. After the fourth round of selection, the phage pool enriched for binding to P-rich peptide was purified by PEG/NaCl precipitation and suspended in 2 ml phosphate buffered saline (PBS).

Generation of bait peptide for isolation of Happ intrabodies. A plasmid encoding mHDx-1Q50-GST (Scherzinger et al., 1997) was transformed into XL-10 gold ultra-competent bacteria (Stratagene, La Jolla, CA) according to the manufacturer's protocol. Cells were grown to an OD of 0.6 at 600 nm and induced with 1 mM isopropyl β-D-1-thiogalactopyranoside (IPTG) for 4 hours. Bacteria were collected by centrifugation, and GST fusion proteins were isolated in 1 ml 50% glutathione-Sepharose bead slurries containing bound peptide (Ausubel F.M., 1993). Twenty-five μl of each bead slurry was added to 10 μl protein loading buffer, boiled for 5 minutes and separated by SDS/PAGE. Peptide expression was verified by Coomassie staining of PAGE gels and the sizes compared to a protein molecular weight marker (data not shown).

Selection of Happ intrabodies from P-rich-specific phage display library. One ml of the pre-selected, P-rich-specific phage pool was selected with mHDx-1Q50-GST as described in the library provider's instructions. Briefly, GST-fusion bait peptide bound to glutathione-sepharose beads was incubated with replication deficient phage displaying pre-selected, P-rich scFvs and then washed in PBS with 0.1% triton X-100 to remove unbound phage particles. Bound phages were allowed to infect log phase bacteria. To repeat selection, M13 helper phages, which do not display scFvs but enable the replication of scFv displaying phages from pre-infected bacteria, were used to recover selected phages. This selection was repeated an additional two times. After the final round of selection, individual clones were screened for inserts by the polymerase chain reaction (PCR)(Griffiths et al., 1994). Six clones with inserts were identified

(Happ1-6). Inserts were sequenced and analyzed for open reading frames (ORFs). Three clones were found to contain ORFs, two of which were redundant. The two unique ORFs (Happ1 and 3) were amplified by PCR using primers designed to add both appropriate restriction sites and a C-terminal hemaglutinin (HA) epitope tag, and cloned into the AAV (adeno-associated virus) genome plasmid (Stratagene) mammalian expression vector for characterization in cell culture, and also into the pGEX-6p1 GST fusion (Amersham Biosciences, Piscataway, NJ.) bacterial expression vector for protein purification. A control intrabody that does not bind HDx-1 (CV_L) was also isolated from the library and cloned into these vectors. Cloning was performed according to the Invitrogen One-shot top 10 competent cell protocol.

Htt aggregation and toxicity assays. HEK 293 cells were co-transfected with mHDx-1Q103-GFP and intrabody (iAb) in poly-D-lysine-coated 24 well plates at ~60% confluency. Each well received 0.2 μg mHDx-1 DNA in pcDNA3.1 vector and iAb (V_L12.3, MW7, Happ1, Happ3, or CV_L) DNA in AAV vector at various ratios to HDx-1 (0.5:1, 1:1, 2:1, 3:1, 4:1). DNA levels were normalized to 1 μg per well using CV_L in AAV vector. Non-transfected wells were used as a negative control, and each condition was performed in triplicate. Cultures were moved to a 33^{o}C incubator 8 hours post-transfection to slow cell division and maintain a monolayer. At 40 hours post-transfection, cells were incubated in medium containing 1 mM EthD-2 (Invitrogen) for 15 min at 33^{o}C for detection of dead cell nuclei. Cells were then fixed in 4% paraformaldehyde (PFA) at 4^{o}C for 30 minutes and permeabilized with PBS containing 0.1% triton

for 15 minutes. For detection of all nuclei, cells were treated with PBS containing 0.5 μg/ml DAPI. Fluorescence microscopy was used to visualize dead cells (red channel), large Htt aggregates (green channel), and total cell number (blue channel). Three representative microscope fields were analyzed for each well (9 per condition). Dead cells and aggregates were counted for each field and normalized to the total cell number. P values were computed using two-way analysis of variance (ANOVA) and Bonferroni post-hoc test.

Brain slice neurodegeneration assay. All animal experiments were performed in accordance with the institutional Animal Care and Use Committee and Duke University Medical Center Animal Guidelines. Brain slice preparation and biolistic transfection were performed as previously described (Lo et al., 1994; Khoshnan et al., 2004). Briefly, brain tissue was dissected from euthanized postnatal day 10 (P10) CD Sprague-Dawley rats (Charles River Laboratory, Raleigh, NC) and placed in ice-cold culture medium containing 15% heat-inactivated horse serum, 10 mM KCl, 10 mM HEPES, 100 U/ml penicillin/streptomycin, 1 mM MEM sodium pyruvate, and 1 mM L-glutamine in Neurobasal A (Invitrogen). Brain tissue was cut in 250 μm thick coronal slices using a Vibratome (Vibratome, St. Louis, MO) and incubated for 1 hr at 37^{o}C under 5.0% CO_2 prior to biolistic transfection. Gold particles (1.6 μm gold microcarriers; Bio-Rad, Hercules, CA) were coated with the appropriate DNAs (see below) as per manufacturer's instructions and loaded into Tefzel tubing (McMaster-Carr, Atlanta, GA) for use with the Helios biolistic device (Bio-Rad), which was used at a delivery pressure of 95 psi. Gold particles were coated with

expression constructs encoding YFP as a morphometric marker, cyan fluorescent protein CFP-tagged mHDx-1Q-73, and the relevant iAb; for control transfections, particles were coated with YFP + CV_L, YFP + mHDx-1Q73 and vector backbone DNA, or YFP + mHDx-1Q73 + CV_L. For each condition, transfections were done on 12 brain slices and using fluorescence microscopy the number of healthy MSNs expressing the YFP reporter was assessed 4-5 days after brain slice preparation and transfection using fluorescence microscopy. MSNs with normal-sized cell bodies, even and continuous expression of YFP in the cell body and dendrites, and having > 2 discernable primary dendrites > 2 cell bodies long were scored as healthy. P values were computed using one-way ANOVA and Bonferroni post-hoc test.

Immunohistochemical HDx-1 localization. ST14A cells were grown in 6 well plates containing coverslips and co-transfected with mHDx-1Q103-GFP and intrabody in 6 well plates at ~60% confluency. Each well received 1 μg mHDx-1 and intrabody DNA at optimal ratios. Non-transfected wells were used as a negative control. At 48 hours post-transfection, cells were fixed and permeabilized as described above. Intrabodies were then labeled using M2 anti-Flag for MW7 and 3F10 anti-HA for V_L12.3, Happ1 and Happ3. Secondary antibodies were conjugated to Alexa fluor 568 (Invitrogen)(S. Hockfield, 1993). Cells were processed for microscopy as above. Mean fluorescence intensity for whole cell and nuclear HDx-1 (green channel) and iAb (red channel) was measured in 3 microscope fields per well. The ratio of nuclear HDX-1 or iAb to cellular HDx-1 or iAb was determined by (mean intensity of nucleus/mean

intensity of whole cell). P values were computed using one-way ANOVA and Bonferroni post-hoc test.

HDx-1 immunoblot assay. HEK 293 cells were co-transfected with HDx-1-GFP and iAb in 10 cm dishes at ~80% confluency. Each dish received 4 μg of mHDx-1Q103 or HDx-1Q25 DNA in pcDNA3.1 vector and iAb DNA in AAV vector at the optimal ratio for each iAb (4 μg V_L12.3, 16 μg MW7, 8 μg Happ1 and Happ3). A non-transfected dish was used as a negative control. At 48 hours post-transfection, cells were dislodged by mechanical dissociation and pipetting, harvested by centrifugation, washed with PBS and lysed by sonication in 500 μl lysis buffer (25 mM Hepes, 50 mM NaCl, 1 mM $MgCl_2$, 0.5 % triton) containing 1 Complete, Mini, EDTA-free Protease Inhibitor Cocktail tablet (Roche) per 7 ml buffer. The soluble protein fraction was collected by centrifugation for 20 min at 4^o C at 20,000x g. The insoluble pellet was sonicated in 150 μl 6 M urea and incubated for 20 min at RT. Immunoblots were then performed using rabbit anti-GFP (1:1000 Invitrogen, Carlsbad CA) as primary antibody and HRP-conjugated, goat anti-rabbit (1:10,000 Santa Cruz Biotechnology, Santa Cruz, CA.) as secondary antibody to detect HDx-1-GFP. For a loading control, membranes were stripped using Restore western blot buffer (Pierce) and re-probed with mouse anti-β-tubulin (1:1000 Sigma) as primary and HRP-conjugated, goat anti-mouse (1:10,000 Santa Cruz Biotechnology) as secondary antibody. Densities of HDx-1 and β-tubulin bands were determined. Each HDx-1 band was normalized to the level of the β-tubulin band for that sample. The ratio of HDx-1 level in the presence of iAb to HDx-1 level alone was determined by (density of

intrabody plus HDX-1/density of iAb plus HDx-1 βtubulin)/(density of HDx-1 alone/density of HDx-1 alone βtubulin). The experiment was repeated three additional times giving an N of 4. P values were computed using two-way ANOVA and Bonferroni post-hoc test.

HDx-1 turnover assay. ST14A cells were grown in 6 well plates containing coverslips and co-transfected with HDx-1-SNAP and intrabody at ~60% confluency. Each well received 1 μg of either mHDx-1Q97-SNAP (fused to the SNAP tag) or HDx-1Q25-SNAP DNA in pSEMXT-26m vector (Covalys Witterswil, Switzerland) and iAb DNA in AAV vector at optimal ratios (1 μg V_L12.3, 4 μg MW7, 2 μg Happ1 and Happ3). Non-transfected wells were used as a negative control, and each condition was performed twice. To covalently label HDx-1 present at 24 hours post-transfection, cells were treated with DAF green fluorescent SNAP-substrate (Covalys) according to the manufacturer's protocol. After labeling, cells were handled in low light conditions to avoid photo bleaching the DAF substrate. One well of each condition was then fixed and permeabilized as described above. For detection of all nuclei, cells were treated with blocking solution (3% BSA w/v, 10% NGS, 0.1% Triton X-100 in PBS) containing 1:2000 Toto-3 iodide (Invitrogen). Coverslips were then mounted with Prolong gold anti-fade reagent (Invitrogen). The remaining well of each condition was incubated for an additional 24 hours (48 hours post-transfection) to allow turnover of labeled HDx-1, and then processed for microscopy as above. Mean fluorescence intensity of individual cells was observed in 3 microscope fields per well using LCS software (Leica Wetzlar, Germany). Mean cellular fluorescence

intensities were computed for both the 24 and 48 hour conditions. The percentage of labeled HDx-1 at 24 hours and remaining at 48 hours was determined by ((mean intensity at 48 hours/mean intensity at 24 hours) x 100). The experiment was repeated three additional times giving an N of 4. P values were computed using one-way ANOVA and Bonferroni post-hoc test.

REFERENCES

Arrasate M, Mitra S, Schweitzer ES, Segal MR, Finkbeiner S (2004) Inclusion body formation reduces levels of mutant huntingtin and the risk of neuronal death. Nature 431:805-810.

Atwal RS, Xia J, Pinchev D, Taylor J, Epand RM, Truant R (2007) Huntingtin has a membrane association signal that can modulate huntingtin aggregation, nuclear entry and toxicity. Human molecular genetics 16:2600-2615.

Ausubel F.M. RB, R.E. Kingston, D.D. Moore, J.G. Seidman, J.A. Smith, K. Struhl (1993) Current protocols in molecular biology: Greene publishing associates and Wiley interscience

Biocca SS, Cattaneo AA (1995) Intracellular immunization: antibody targeting to subcellular compartments. Trends in cell biology 5:248-252.

Biocca SS, Ruberti FF, Tafani MM, Pierandrei-Amaldi PP, Cattaneo AA (1995) Redox state of single chain Fv fragments targeted to the endoplasmic reticulum, cytosol and mitochondria. Biotechnology 13:1110-1115.

Cattaneo E, Conti L (1998) Generation and characterization of embryonic striatal conditionally immortalized ST14A cells. Journal of neuroscience research 53:223-234.

Colby DW, Garg P, Holden T, Chao G, Webster JM, Messer A, Ingram VM, Wittrup KD (2004a) Development of a human light chain variable domain (VL) intracellular antibody specific for the amino terminus of huntingtin via yeast surface display. Journal of molecular biology 342:901-912.

Colby DW, Chu Y, Cassady JP, Duennwald M, Zazulak H, Webster JM, Messer A, Lindquist S, Ingram VM, Wittrup KD (2004b) Potent inhibition of huntingtin aggregation and cytotoxicity by a disulfide bond-free single-domain intracellular antibody. Proceedings of the national academy of sciences of the United States of America 101:17616-17621.

Dragatsis I, Levine MS, Zeitlin S (2000) Inactivation of Hdh in the brain and testis results in progressive neurodegeneration and sterility in mice. Nature genetics 26:300-306.

Duennwald ML, Jagadish S, Muchowski PJ, Lindquist S (2006) Flanking sequences profoundly alter polyglutamine toxicity in yeast. Proceedings of the national academy of sciences of the United States of America 103:11045-11050.

Faber PW, Barnes GT, Srinidhi J, Chen J, Gusella JF, MacDonald ME (1998) Huntingtin interacts with a family of WW domain proteins. Human molecular genetics 7:1463-1474.

Griffiths AAD, Williams SSC, Hartley OO, Tomlinson IIM, Waterhouse PP, Crosby WWL, Kontermann RRE, Jones PPT, Low NNM, Allison TTJ (1994) Isolation of high affinity human antibodies directly from large synthetic repertoires. The EMBO journal 13:3245-3260.

Harper SQ, Staber PD, He X, Eliason SL, Martins IH, Mao Q, Yang L, Kotin RM, Paulson HL, Davidson BL (2005) From the Cover: RNA interference improves motor and neuropathological abnormalities in a Huntington's

disease mouse model. Proceedings of the national academy of sciences of the United States of America 102:5820-5825.

Holbert S, Denghien I, Kiechle T, Rosenblatt A, Wellington C, Hayden MR, Margolis RL, Ross CA, Dausset J, Ferrante RJ, Neri C (2001) The Gln-Ala repeat transcriptional activator CA150 interacts with huntingtin: Neuropathologic and genetic evidence for a role in Huntington's disease pathogenesis. Proceedings of the national academy of sciences of the United States of America 98:1811-1816.

Jackson GR, Sang T, Khoshnan A, Ko J, Patterson PH (2004) Inhibition of mutant huntingtin-induced neurodegeneration In vivo by expression of a polyproline-binding single chain antibody. SFN abstract 938.5.

Jansen LET, Black BE, Foltz DR, Cleveland DW (2007) Propagation of centromeric chromatin requires exit from mitosis. Journal of cell biology 176:795-805.

Khoshnan A, Ko J, Patterson PH (2002) Effects of intracellular expression of anti-huntingtin antibodies of various specificities on mutant huntingtin aggregation and toxicity. Proceedings of the national academy of sciences of the United States of America 99:1002-1007.

Khoshnan A, Ko J, Watkin EE, Paige LA, Reinhart PH, Patterson PH (2004) Activation of the I{kappa}B kinase complex and nuclear factor-{kappa}B contributes to mutant huntingtin neurotoxicity. The journal of neuroscience 24:7999-8008.

Ko J, Ou S, Patterson PH (2001) New anti-huntingtin monoclonal antibodies: implications for huntingtin conformation and its binding proteins. Brain research bulletin 56:319-329.

Leavitt BBR, Guttman JJA, Hodgson JJG, Kimel GGH, Singaraja RR, Vogl AAW, Hayden MMR (2001) Wild-type huntingtin reduces the cellular toxicity of mutant huntingtin in vivo. American journal of human genetics 68:313-324.

Lo ASY, Zhu Q, Marasco WA (2008) Intracellular antibodies (intrabodies) and their therapeutic potential. in: Therapeutic antibodies, pp 343-373.

Lo DDC, McAllister AAK, Katz LLC (1994) Neuronal transfection in brain slices using particle-mediated gene transfer. Neuron 13:1263-1268.

Machida Y, Okada T, Kurosawa M, Oyama F, Ozawa K, Nukina N (2006) rAAV-mediated shRNA ameliorated neuropathology in Huntington disease model mouse. Biochemical and biophysical research communications 343:190-197.

Messer AA, McLear JJ (2006) The therapeutic potential of intrabodies in neurologic disorders: focus on Huntington and Parkinson diseases. BioDrugs 20:327-333.

Modregger J, DiProspero NA, Charles V, Tagle DA, Plomann M (2002) PACSIN 1 interacts with huntingtin and is absent from synaptic varicosities in presymptomatic Huntington's disease brains. Human mol genetics 11:2547-2558.

Passani LA, Bedford MT, Faber PW, McGinnis KM, Sharp AH, Gusella JF, Vonsattel J-P, MacDonald ME (2000) Huntingtin's WW domain partners in

Huntington's disease post-mortem brain fulfill genetic criteria for direct involvement in Huntington's disease pathogenesis. Human molecular genetics 9:2175-2182.

Peters MF, Nucifora FC, Kushi J, Seaman HC, Cooper JK, Herring WJ, Dawson VL, Dawson TM, Ross CA (1999) Nuclear targeting of mutant huntingtin increases toxicity. Molecular and cellular neuroscience 14:121-128.

Qin Z-H, Wang Y, Sapp E, Cuiffo B, Wanker E, Hayden MR, Kegel KB, Aronin N, DiFiglia M (2004) Huntingtin bodies sequester vesicle-associated proteins by a polyproline-dependent interaction. The journal of neuroscience 24:269-281.

Rockabrand E, Slepko N, Pantalone A, Nukala VN, Kazantsev A, Marsh JL, Sullivan PG, Steffan JS, Sensi SL, Thompson LM (2007) The first 17 amino acids of Huntingtin modulate its sub-cellular localization, aggregation and effects on calcium homeostasis. Human molecular genetics 16:61-77.

Rodriguez-Lebron E, Denovan-Wright EM, Nash K, Lewin AS, Mandel RJ (2005) Intrastriatal rAAV-mediated delivery of anti-huntingtin shRNAs induces partial reversal of disease progression in R6/1 Huntington's disease transgenic mice. Molecular therapy 12:618-633.

S. Hockfield SC, C. Evans, P. Levitt, J. Pintar, L. Silberstein (1993) Selected methods for antibody and nucleic acid probes: Cold Spring Harbor Laboratory press.

Scherzinger E, Lurz R, Turmaine M, Mangiarini L, Hollenbach B, Hasenbank R, Bates GP, Davies SW, Lehrach H, Wanker EE (1997) Huntingtin-encoded polyglutamine expansions form amyloid-like protein aggregates in vitro and in vivo. Cell 90:549-558.

Schilling G, Savonenko AV, Klevytska A, Morton JL, Tucker SM, Poirier M, Gale A, Chan N, Gonzales V, Slunt HH, Coonfield ML, Jenkins NA, Copeland NG, Ross CA, Borchelt DR (2004) Nuclear-targeting of mutant huntingtin fragments produces Huntington's disease-like phenotypes in transgenic mice. Human molecular genetics 13:1599-1610.

Staub OO, Rotin DD (1996) WW domains. Structure 4:495-499.

Steffan JS, Kazantsev A, Spasic-Boskovic O, Greenwald M, Zhu Y-Z, Gohler H, Wanker EE, Bates GP, Housman DE, Thompson LM (2000) The Huntington's disease protein interacts with p53 and CREB-binding protein and represses transcription. Proceedings of the national academy of sciences of the United States of America 97:6763-6768.

Stocks MM (2005) Intrabodies as drug discovery tools and therapeutics. Current opinion in chemical biology 9:359-365.

Truant R, Atwal RS, Burtnik A (2007) Nucleocytoplasmic trafficking and transcription effects of huntingtin in Huntington's disease. Progress in neurobiology 83:211-227.

Zuccato C, Ciammola A, Rigamonti D, Leavitt BR, Goffredo D, Conti L, MacDonald ME, Friedlander RM, Silani V, Hayden MR, Timmusk T,

Sipione S, Cattaneo E (2001) Loss of huntingtin-mediated BDNF gene transcription in huntington's disease. Science 293:493-498.

FIGURES

Fig 1

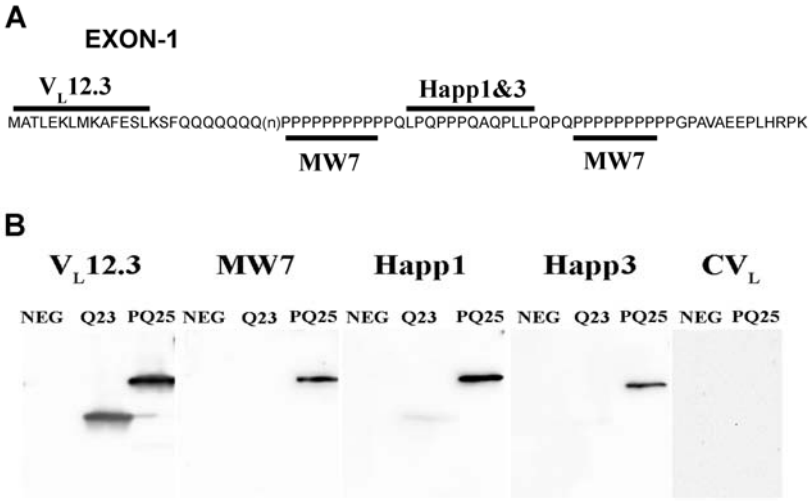

Figure 1. The intrabodies bind different epitopes of HDx-1. (A) The epitopes in HDx-1 for the various intrabodies are depicted. (B) To verify binding specificity 293 cells were transfected with HDx-1 (PQ25) or HDx-1ΔPRR (Q23). After 48 hours, cell lysates were separated by SDS/PAGE and blotted with intrabodies. Non-transfected cells (NEG) were used as a negative control. While V_L12.3 binds both forms of HDx-1, MW7, Happ1 and Happ3 bind only the form containing the PRR. CV_L does not bind HDx-1.

Fig 2

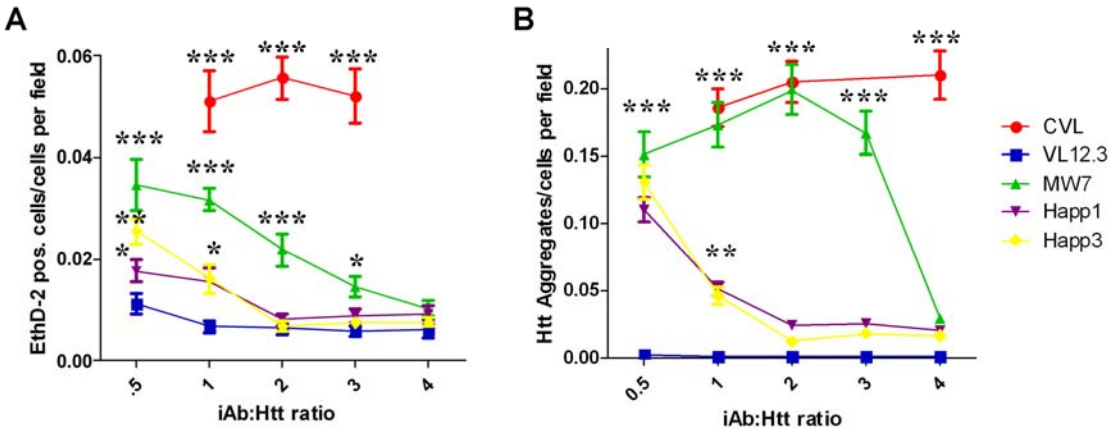

Figure 2. The anti-Htt intrabodies reduce mHDx-1-induced toxicity and aggregation in cell culture. (A) To quantify mHtt toxicity, 293 cells were co-transfected with mHDx-1-GFP and intrabody at various intrabody/Htt ratios and incubated for 48 hours. Cells were stained with EthD-2 to identify dead cell nuclei, fixed, and stained with DAPI to identify all cell nuclei. The number of dead cells was normalized to total cell number. All of the intrabodies reduce mHDx-1-induced cell death in a saturable, dose-dependent manner, with maximal effects at different intrabody/Htt ratios (1:1 for V_L12.3, 2:1 for Happ1 and 3, and 4:1 for MW7). (B) Aggregation was determined by counting GFP foci and normalizing to total cell number. * = Differ from V_L12.3 at p<.05, **=p<.01. The point labeled as 0 on the intrabody:Htt axis corresponds to the value for HDX-1 + CV_L.

Fig 3

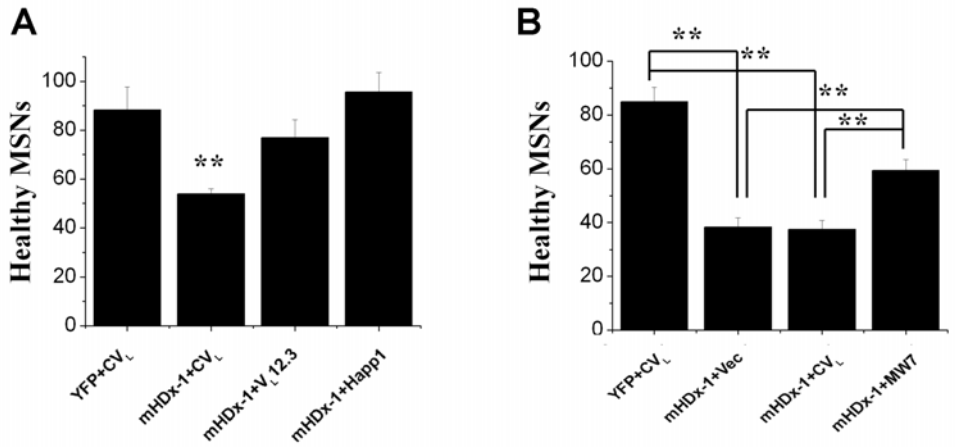

Figure 3. Anti-Htt intrabodies protect against mHDx-1-induced neurodegeneration in cortico-striatal brain slice explants. Cortico-striatal brain slices were biolistically transfected with plasmid expression constructs encoding YFP, mHDx1(N1-66 with 148 Q), and the indicated intrabody. The number of healthy medium spiny neurons in the striatal region of each slice was scored visually 4-5 days after slice preparation and transfection. (A) Slices were transfected with either YFP + CV_L; YFP + CV_L + mHDx1; YFP + mHDx1 + V_L12.3; or YFP + mHDx1 + Happ1. ** = Differ from YFP at p<.01. (B) Slices were transfected with YFP + CV_L; YFP + vector + mHDx-1; YFP + CV_L + mHDx1 or YFP + mHDx1 + MW7. ** = p<.01. The data in A and B are from independent experiments.

Fig 4

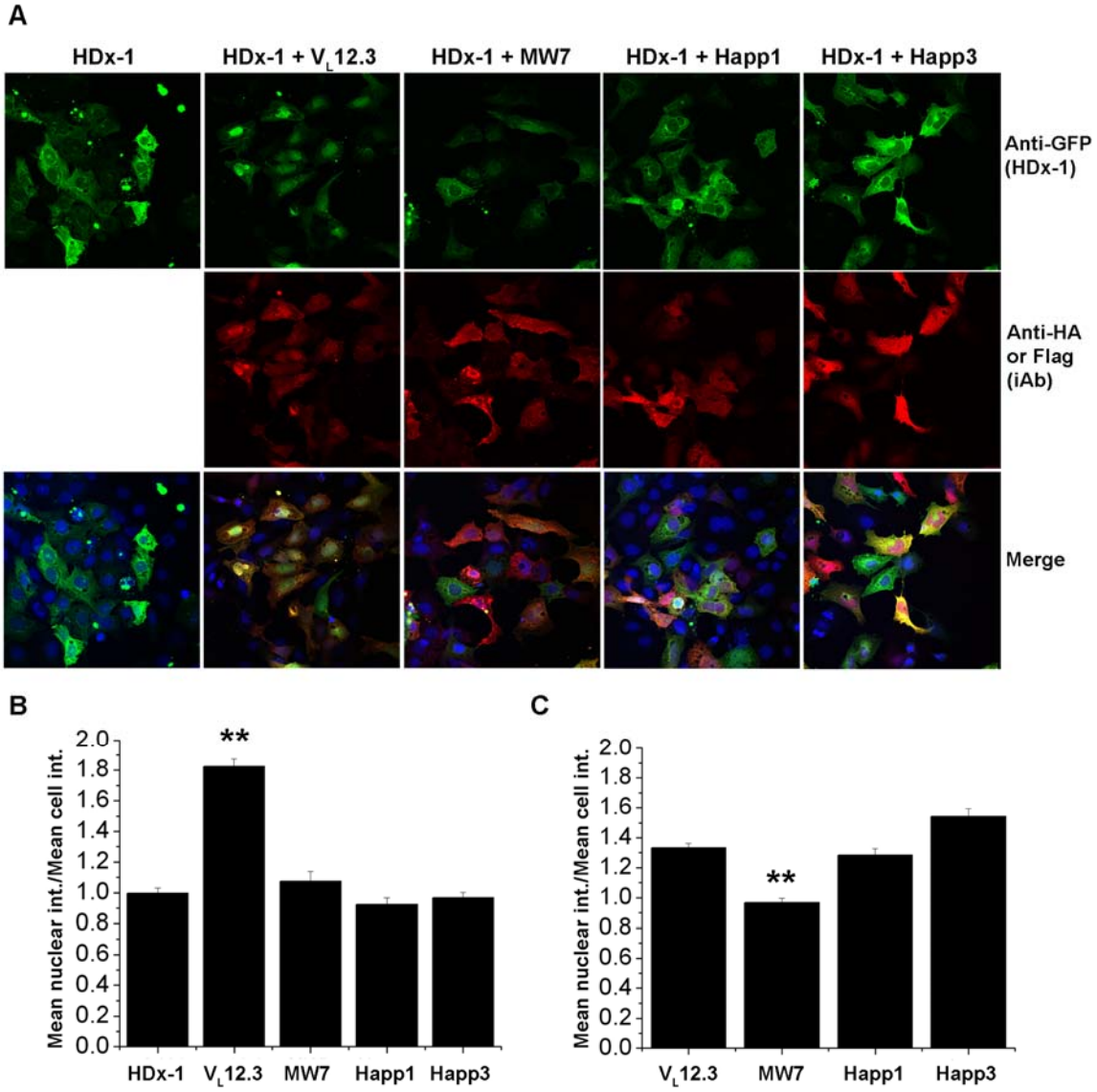

Figure 4. V_L12.3 increases the level of nuclear HDx-1. ST14A cells were co-transfected with mHDx-1Q103-GFP and intrabody (iAb) at the optimal ratio for each iAb. (A) At 48 hours post-transfection, cells were fixed, stained for the appropriate iAb and cell nuclei, and analyzed by confocal microscopy. (B) Mean whole cell fluorescence intensity (int.) and mean nuclear fluorescence intensity of HDx-1 are compared. While MW7, Happ1 and Happ3 have no effect on HDx-1 localization, V_L12.3 significantly increases nuclear HDx-1. ** = Differs from HDx-1

at p<.01. (C) Mean whole cell fluorescence intensity and mean nuclear fluorescence intensity of the iAbs themselves were compared. MW7 is slightly more cytoplasmic than the other iAbs.

Fig 5

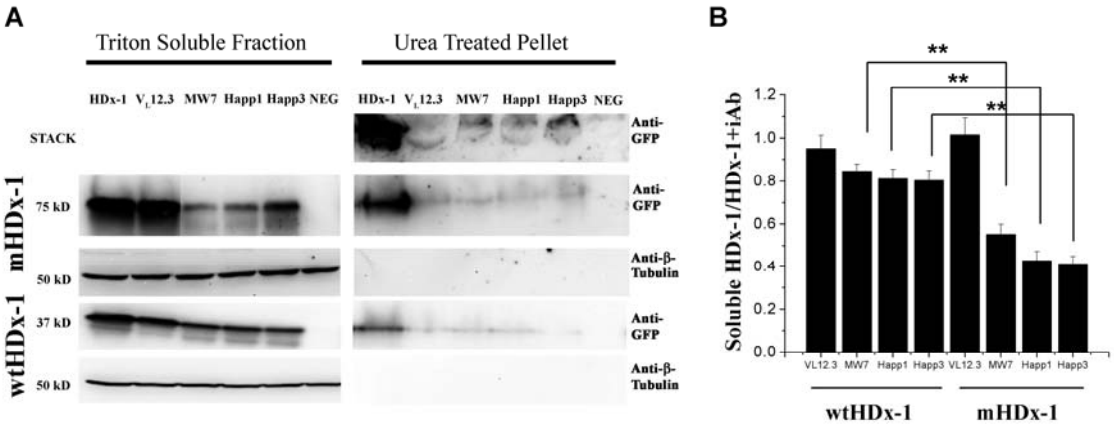

Figure 5. All of the anti-Htt intrabodies reduce insoluble mHDx-1, while only the anti-PRR intrabodies also reduce soluble mHDx-1. 293 cells were co-transfected with intrabody and mHDx-1 (76 kD) or wtHDx-1 (40 kD) at the optimal ratio for each intrabody. (A) At 48 hours post-transfection, cells were lysed with detergent. The soluble protein fraction was recovered and the insoluble fraction was treated with urea. Samples were then separated by SDS-PAGE and blotted for HDx-1. Non-transfected cells (NEG) were used as a negative control. All of the anti-Htt intrabodies reduce insoluble mHDx-1. (B) Quantification of bands shows that reduction of soluble HDx-1 by PRR-binding intrabodies is significantly greater for the mutant than the WT form of Htt. V_L12.3 does not reduce soluble mHDx-1. Chemiluminescence densitometry was used to compare the levels of soluble mHDx-1 and wtHDx-1. Each band was normalized to the level of β-tubulin (54 kD) in that sample. Bands for HDx-1 + intrabody (iAb) were then

normalized to the level of soluble HDx-1 for that blot. N = 4 independent experiments, and values for each blot were used to compile the mean +/- S.E.M. ** = p<0.01

Fig 6

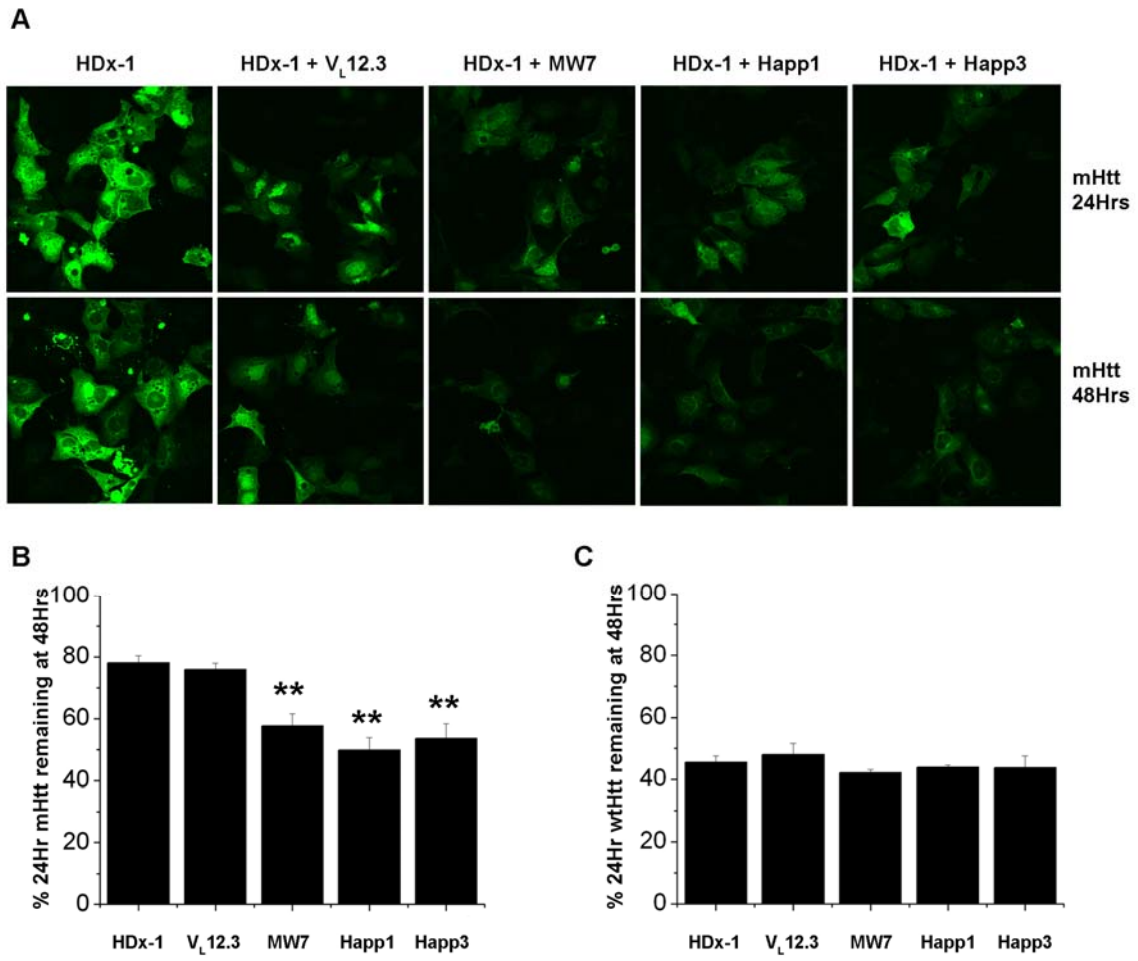

Figure 6. Anti-PRR intrabodies increase mHDx-1 turnover. ST14A cells were transfected with mHDx-1-SNAPtag 97Q (A and B) or wtHDx-1-SNAPtag 25Q (C) and intrabody at the optimal ratio for each intrabody. DAF green fluorescent SNAP substrate was added to cultures at 24 hrs post-transfection. Some cultures were then fixed and stained with Topro-3 iodide nuclear marker while others were incubated an additional 24 hrs to allow turnover of labeled HDx-1.

Mean fluorescence intensity of cells at 24 hrs was compared to intensity at 48 hrs to determine the percentage of labeled HDx-1 remaining. V_L12.3 has no effect on mHDx-1 or wtHDx-1 turnover while MW7, Happ1 and Happ3 significantly increase the rate of mHDx-1 turnover. N = 4, ** = p<.01

Chapter 3

Intrabody gene therapy ameliorates motor, cognitive and neuropathological symptoms in multiple mouse models of Huntington's disease

Southwell AL, Ko J, Patterson PH

INTRODUCTION

Intrabodies are a powerful and diverse therapeutic tool ideally suited to treatment of protein mis-folding neurodegenerative diseases. The potential for iAb design is virtually infinite. An example is the targeting of iAbs to different epitopes within the same protein. Intrabodies that recognize expanded polyglutamine in mHtt such as MW1 and 2 increase mHtt aggregation and toxicity in cultured cells while MW7, which recognizes the adjacent polyP regions, has the opposite effects (Khoshnan et al., 2002). Intrabodies can also be targeted to specific protein confirmations such as D5, an anti-α-synuclein iAb that recognizes only the highly toxic oligomeric form of the protein, and does not bind monomeric or fibrillar α-synuclein (Emadi et al., 2007).

In addition, iAbs can be fused to signaling sequences to alter the functional outcome. For example, C4, an iAb that recognizes the N-terminus of Htt and reduces aggregation and toxicity in cell culture, brain slice and *Drosophila* HD models (Murphy and Messer, 2004; Wolfgang et al., 2005; McLear et al., 2008) has no baseline effects on Htt localization. However, when C4 is fused to a nuclear localization sequence (NLS), it directs Htt, normally most abundant in the cytoplasmic and perinuclear regions, to the nucleus (Lecerf et al., 2001). Similarly, the D10 iAb recognizes α-synuclein, the mis-folded mutant

version of which can cause PD, and reduces α-synuclein-induced toxicity and aggregation in cell culture. D10 directs α-synuclein to the nucleus when fused to an NLS, but not the highly homologous β-synuclein (Zhou et al., 2004). Another example is an iAb (sFvβ1) that recognizes an epitope adjacent to the β-secretase site of amyloid precursor protein (APP), the precursor to the Aβ peptide, whose mis-folded mutant form can cause AD. This iAb shifts APP processing toward the more favorable α-secretase cleavage product, reducing Aβ production and toxicity in cell culture models of AD with no baseline effects on localization. When sFvβ1 is fused to an endoplasmic reticulum retention signal, however, it prevents newly generated APP from leaving the endoplasmic recticulum, leading to its degradation and virtually abolishing Aβ production (Paganetti et al., 2005).

Increased clearance of Htt is a common property of anti-Htt iAbs with therapeutic potential. Compared to cells infected with HDx-1 plus a control iAb, bicistronic adenoviral delivery of HDx-1 plus the C4 iAb dramatically reduces levels of both WT and mHDx-1 in infected 293 cells (Miller et al., 2005). EM48, an iAb recognizing an epitope C-terminal to the PRR of Htt, preferentially binds mHtt and increases its ubiquitination and turnover in EM48-adenovirus-infected PC12 cells. Adenoviral delivery of EM48 to the brains of R6/2 and N171-82Q HD model mice reduces striatal neuropil aggregates, increases Htt cleavage products in brain homogenates, and improves the gait and rotarod performance of N171-82Q mice. However, EM48 gene therapy has no effect on intranuclear inclusions, body weight or survival (Wang et al., 2008). This adenoviral delivery strategy is also limited to the study of short-life span HD models because of the

transient transgene expression of the adenoviral vector. The more stably expressing adeno-associated virus (AAV) vector is preferable in this regard. The AAV vector can yield long-term transgene expression in a wide range of cell types, depending on serotype. The AAV1 capsid, which displays excellent spread and transduction efficiency in the central nervous system (CNS), preferentially infects neurons, but also infects glial and ependymal cells (Wang et al., 2003a). As neuronal death and dysfunction in HD may not occur solely by a cell autonomous mechanism, transduction of glia, at least in preclinical studies, is preferable (Shin et al., 2005). The AAV2 genome under the control of the chicken β-actin promoter plus CMV promoter enhancer regions (CBA) confers long-term stable transgene expression. The combination of these properties in chimeric AAV2/1 vectors is ideal for iAb delivery to HD model mice.

Due to the clear mechanistic differences of V_L12.3 and Happ1 as potential therapeutics and the lack of a single, ideal mouse HD model (Chapter 1; Southwell et al., 2008), we tested both iAbs for therapeutic efficacy in a lentiviral model and four transgenic HD mouse lines.

RESULTS

Widespread striatal transduction is achieved with the lentiviral vector in adult mice and with the AAV vector in adult and neonatal mice. A schematic outline of the various types of gene therapy experiments is given in Fig. 1. In the lentiviral model, adult WT mice were unilaterally injected with a mixture of mHDx-1 or GFP lentivirus plus GFP, V_L12.3, or Happ1 AAV. Mice

were sacrificed 6 weeks later and coronal sections throughout the striatum were stained for mHDx-1 and iAb. Similar striatal spread is seen with both viruses (Fig. 2A). Co-localization of mHDx-1 and iAb in confocal images shows that these viruses co-transduce cells (Fig. 2B). There are a larger number of iAb-positive cells than mHDx-1-positive cells, indicating a greater transduction efficiency of AAV2/1. Adult injections of AAV2/1 were also used bilaterally in the N171-82Q, YAC128 and BACHD HD transgenic mice. Striatal iAb spread in these mice is similar to that seen in the lentiviral model (data not shown). The R6/2 model has an accelerated time frame that includes Htt inclusions at birth and onset of behavioral symptoms at less than 3 weeks of age (Mangiarini et al., 1996; Stack et al., 2005). Because of this and the 3 week delay before AAV delivered transgene expression reaches its peak (Tenenbaum et al., 2004), postnatal day 3 injections were used in this line. Striatal spread equivalent to or better than that seen with adult injections is apparent (Fig. 3).

Treatment with V_L12.3 or Happ1 prevents abnormal amphetamine-induced rotation behavior in the lentiviral HD model. Four-week old C57Bl/6 mice were injected unilaterally with mHDx-1 or GFP lentivirus plus GFP, V_L12.3 or Happ1 AAV. Six weeks after surgery, animals were injected with 10 mg/kg amphetamine i.p. After 5 min, animals were placed in an open field for 30 min and ipsilateral rotations counted (Fig. 4). Age-matched, un-injected mice were also tested as a control for surgery effects. Naïve mice were randomly assigned to right turn or left turn groups for scoring ipsilateral turns. Compared to naïve mice, injection of GFP lentivirus along with any of the AAVs does not significantly

increase the number of ipsilateral rotations. In contrast, animals injected with mHDx-1 lentivirus plus GFP AAV display a major increase in ipsilateral rotations. Co-injection of V_L12.3 or Happ1 AAV strongly reduces the number of ipsilateral rotations in mHDx-1 lentivirus-injected animals to levels not significantly different from GFP lentivirus-injected or naïve animals.

Happ1 treatment improves rotarod performance in four transgenic HD models. Mice were assessed for accelerating rotarod performance as follows: weekly from four weeks of age until death in R6/2 and WT littermates (Fig. 5A), every two weeks from six weeks of age until death in N171-82Q and WT littermates (B), monthly from 3 until 7 months of age in YAC128 and WT littermates (Fig. 5C, D), and monthly from 3 until 6 months of age in BACHD mice (Fig. 5E). Compared to WT littermates, R6/2 mice display a deficit in rotarod performance from 5 weeks of age. Compared to GFP-treated mutants, Happ1 treatment ameliorates this deficit between 9 and 12 weeks of age (Fig. 5A). In contrast, compared to GFP-treated mutants, V_L12.3 treatment *reduces* latency to fall in R6/2 mice between 10 and 12 weeks of age. Although rotarod performance is also impaired below GFP controls at 13 weeks of age, statistics cannot be performed, as only one V_L12.3-treated mutant remained alive at this time point.

Compared to WT littermates, N171-82Q mice display a motor deficit on the rotarod from 20 weeks of age. From 22 weeks of age performance is significantly improved by Happ1 treatment (Fig. 5B). Happ1-treated mutants do not differ from WT animals in their performance until 40 weeks of age.

Happ1 treatment improves rotarod performance in 3, 4 and 7 month old YAC128 mice (Fig. 5C, D). The lack of significant difference at 5 and 6 months of age appears to be related to an improvement in the performance of GFP-treated animals rather than a decline in the performance of Happ1-treated mice. YAC128 mice display a learning deficit that includes impaired learning of the rotarod task from 2 months of age (Van Raamsdonk et al., 2005). As rotarod training was performed at 3 months of age with the same number of training trials for all mice, the difference in performance between young GFP- and Happ1-treated mice could be the result of enhanced learning of the task by Happ1 treatment. By 7 months of age, the performance of GFP-treated YAC128 mice begins to decline, presumably as a result of declining motor ability. Happ1 treatment also ameliorated the motor deficit in the BACHD line. Compared to GFP-treated mice, Happ1 treatment increases the latency to fall from the rotarod in 5 and 6 month old BACHD mice (Fig. 5E).

Happ1 treatment improves beam crossing performance in four transgenic HD models. Mice were assessed for beam crossing performance as follows: weekly from four weeks of age until death in R6/2 and WT littermates (Fig. 6A-C), every two weeks from six weeks of age until death in N171-82Q and WT littermates (Fig. 6D-F), monthly from 3 until 7 months of age in YAC128 and

WT littermates (Fig. 6G-I), and monthly from 3 until 6 months of age in BACHD mice (Fig. 6J-L). Three widths of square beam were used: 28 mm, 12 mm and 6 mm. Compared to WT littermates, R6/2 mice display increased time to cross the beams from 10, 7 and 5 weeks respectively. Being the easiest to traverse, there are no significant effects of iAb treatment on time to cross the 28 mm beam. However, compared to GFP-treated mice, Happ1 treatment does reduce the time to cross the 12 mm beam in 10 and 11 week old R6/2 mice, and the 6 mm beam between 9 and 11 weeks of age. Conversely, compared to GFP-treated littermates, V_L12.3 treatment *increases* the time to cross the 12 mm beam at 11 and 12 weeks of age and the 6 mm beam at 9 and 10 weeks of age.

N171-82Q mice display increased time to cross the three beams at 22, 16, and 12 weeks respectively. Happ1 treatment significanly reduces time to cross the 28 mm beam from 22 weeks of age on, the 12 mm beam in 16, 18 and 24 weeks and older mutants, and the 6 mm beam in 18, 20, and 26 weeks and older mutants. Happ1-treated mutants only show a deficit as compared to WT mice in time to cross the 12 mm beam at 30 and 40 weeks of age and the 6 mm beam at 28, 30, 38, and 40 weeks of age.

Compared to WT littermates, YAC128 mice display impaired beam crossing performance at 7 months of age for the 28 mm beam and 3 and 4 months of age for the 12 mm and 6 mm beams. Compared to GFP-treated mice, Happ1 treatment reduces the time to cross the 28 mm beam in 7 month-old YAC128 mice and the 12 mm and 6 mm beams at 3 and 4 months. As in the rotarod test, the performance of the GFP-treated YAC128 mice appears to

improve over the earliest time points, suggesting a motor task learning deficit that is restored by Happ1 treatment. In contrast, V_L12.3 treatment appears to exacerbate this learning deficit in 3 month-old mice. Happ1 treatment of BACHD mice reduces the time to cross the beams at 5 and 6 months for the 28 mm beam, at 4 and 6 months for the 12 mm beam, and at 6 months for the 6 mm beam.

Happ1 treatment improves climbing performance in YAC128 and BACHD mice. Climbing time was assessed in 7 month-old YAC128 and WT littermates (Fig. 7A) and in 6 month-old BACHD mice (Fig. 7B). Mice were placed at the bottom of a closed-top wire mesh cylinder and observed for 5 minutes. Time spent climbing with all four feet off of the tabletop was scored. Compared to WT littermates, GFP- and V_L12.3- treated YAC128 mice investigate the wire mesh and rear on two or three legs frequently, but climbing time is reduced. Happ1 treatment increases climbing time in these mice to a level not significantly different from WT mice (Fig. 7A). Compared to GFP-treated mice, Happ1 treatment also increases climbing time in BACHD mice (Fig. 7B).

Happ1 treatment ameliorates clasping in N171-82Q mice. Twenty week-old N171-82Q and WT littermates were assayed for clasping. Mice were suspended by the tail and observed for 1 minute. Mice with normal limb extension were given a score of 0. Forelimb clasping was scored as 1, and hind limb clasping was scored as 2 (Fig. 8). WT mice do not exhibit clasping. All GFP-treated N171-82Q mice exhibit clasping, with roughly half displaying forelimb-only clasping and half displaying hind limb clasping. The majority of Happ1-

treated mutants display forelimb-only clasping, while a few display hind limb clasping or no clasping.

Happ1 treatment normalizes open field behavior in full-length Htt transgenic models of HD. Anxiety behavior of 7 month-old YAC128 and WT littermates and 6 month old BACHD mice was inferred by studying exploration of an open field (Fig. 9) and by investigation of a novel object (Fig. 10). Compared to WT littermates, GFP- and V_L12.3-treated YAC128 mice display reduced entries into, and time spent in, the center of the field. In contrast, Happ1 treatment increases center entries and time in the center to levels not significantly different from WT mice (Fig. 9A, B). In the BACHD mice, there is a trend toward an increased number of center entries as a result of Happ1 treatment, but it does not reach significance (Fig. 9C). However, compared to GFP-treated BACHD mice, Happ1 treatment significantly increases the time spent in the center of the open field (Fig. 9D).

Compared to WT littermates, there is a trend toward reduced investigation of a novel object in GFP- and V_L12.3-treated YAC128 mice, which is reversed by Happ1 treatment, although there are no statistically significant differences between any of the groups (Fig. 10A). Although there is no effect of Happ1 treatment on investigation of a novel object in male BACHD mice, Happ1 treatment increases that number in female BACHD mice (Fig. 10B).

Happ1 treatment improves learning in YAC128 mice. To assess hippocampal-dependent learning, 7 month-old YAC128 and WT littermates and 6 month-old BACHD mice were tested for preference for the novel location of a

known object (Fig. 11A)(Mumby et al., 2002). On day 1, mice were habituated to an open field. After a five minute inter trial interval (ITI) they were re-introduced to the same field now containing two novel objects in the upper corners of the box located far enough from the sides to allow free movement around the outer edge. Investigations of each object were scored for 5 minutes (trial 1, T1). In trial 2 (T2) after another 5 minute ITI, they were re-introduced to the same field with the object previously located in the upper right corner moved to the lower right corner. Investigations of each object were scored for 5 minutes, and the percent of investigations of the target object (the one that was moved) was computed. A score of 50% percent represents no preference. As expected, WT mice of the YAC128 line display no preference in T1 and a preference for the target object in T2 (Fig. 11C). In contrast, GFP- and V_L12.3-treated YAC128 mice display no preference in either trial, indicating impaired spatial learning. However, Happ1 treatment restores significant spatial learning (Fig. 11C). BACHD mice in both treatment groups show no preference for the target object, indicating impaired spatial learning and no effect of iAb treatment (Fig. 11E).

To assess cortical-dependent learning, mice were tested for preference for a novel object. (Fig. 11B)(Mumby et al., 2007). On day 2, mice were re-habituated to the same field and T1 from day 1 was repeated. In T2 they were re-introduced to the field with the object in the upper right corner replaced with a completely novel object. Investigations of each object were scored for 5 minutes, and the percent of investigations of the target object (the completely novel object) was computed. WT mice of the YAC128 line display no preference in T1 and

trended toward a preference for the target object in T2, although the difference is not significant. There are no differences between the treatment groups in WT mice, and when all WT groups are combined, the preference for the target object reaches significance ($p<.01$)(data not shown) indicating that the lack of significant preference is related to small sample size. GFP- and V_L12.3-treated YAC128 mice display no preference for the target object, indicating impaired cortical learning. In contrast, Happ1-treated YAC128 mice display a preference for the target object, indicating preserved cortical learning (Fig. 11D). In the BACHD line, GFP-treated mice display no preference for the target object in T2 while Happ1 treated-mice trended toward a preference for the target object, although this does not reach significance (Fig. 11F).

Happ1 treatment improves body weight of N171-82Q mice. Body weight was assessed as follows: weekly from four weeks of age until death in R6/2 and WT littermates (Fig. 12A), every two weeks from six weeks of age until death in N171-82Q and WT littermates (Fig. 12B) monthly from 3 until 7 months of age in YAC128 and WT littermates (Fig. 12C), and monthly from 3 until 6 months of age in BACHD mice (Fig. 12D). N171-82Q mice weigh significantly less than Wt littermates from 16 weeks of age onward. Happ1-treated mutants though still weighing less than WT littermates, display increased weight as compared to GFP-treated mutants from 22 weeks of age. Compared to WT littermates from 10 weeks of age, R6/2 mice display decreased body weight. YAC128 mice trend toward greater body weight than WT littermates. BACHD

males display greater body weight than females. There is no effect of iAb treatment on this parameter in any of these three models.

Happ1 treatment increases survival in N171-82Q mice while V_L12.3 treatment decreases survival in the R6/2 HD model. Lifespan was assessed in R6/2 mice (Fig. 13A) and N171-82Q mice (Fig. 13B). Once mice became visibly ill, they were assayed twice daily for loss of the righting reflex. Mice who did not immediately right themselves after being laid on their side were euthanized. Happ1 treatment had no effect on lifespan while V_L12.3 treatment decreased survival time of R6/2 mice. However, Happ1 treatment increased maximum lifespan of N171-82Q mice 33% from 30 weeks of age in GFP-treated mutants to 40 weeks of age in Happ1-treated mutants.

In the lentiviral HD model, treatment with V_L12.3 or Happ1 ameliorates neuron-specific mHDx-1 toxicity. Four week-old C57Bl/6 mice were injected unilaterally with mHDx-1 or GFP lentivirus plus GFP, V_L12.3 or Happ1 AAV. Six weeks after surgery, animals were perfused for histology. Mice injected with mHDx-1 lentivirus plus GFP AAV display large areas of strongly diminished DARPP-32 immunostaining. Areas of DARPP-32 loss also display loss of NeuN-positive cells, indicating death of striatal neurons (Fig. 14A). Toto-3 iodide nuclear staining does, however, show the presence of cells within lesioned areas, indicating hypersensitivity of neurons to the toxicity of mHDx-1 lentivirus (Fig. 14B). Lesioned areas also display reactive gliosis, as evidenced by an increase in GFAP staining (Fig. 14C). Co-injection of V_L12.3 or Happ1 AAV with mHDx-1 lentivirus reduces both the size and intensity of DARPP-32 loss (Fig.

14D). To quantify lesion size, the ratio of the area of total DARPP-32 loss to the area of lentivirus transduction was computed (Fig. 14E). Animals injected with GFP lentivirus and any of the AAVs display very small if any lesion areas. Injection of mHDx-1 lentivirus with GFP AAV causes a dramatic increase in lesion size, which is reduced by co-injection of V_L12.3 or Happ1 AAV to a level not significantly different from animals injected with GFP lentivirus plus any of the AAVs.

To assess the severity of DARPP-32 staining loss within the lesion, the ratio of DARPP-32 intensity in the transduced striatum to DARPP-32 intensity in the non-injected side was computed (Fig. 14F). Injection of mHDx-1 lentivirus plus GFP AAV causes a decrease in DARPP-32 intensity of the transduced striatum, which is rescued by V_L12.3 or Happ1 AAV to the level of animals injected with GFP lentivirus.

In the R6/2 model, Happ1 treatment has no effect while V_L12.3 treatment decreases DARPP-32 staining intensity. DARPP-32 staining of coronal sections was measured in 10 week-old R6/2 and WT littermates (Fig. 15A), 7 month-old YAC128 and WT littermates (Fig. 15B), and 6 month-old BACHD mice (Fig. 15C). Compared to WT littermates, R6/2 mice display reduced DARPP-32 intensity (Fig. 15A). Happ1 treatment has no effect while V_L12.3 treatment further decreases the intensity of DARPP-32 staining. There are no differences in the intensity of DARPP-32 between YAC128 and WT littermates, and there is no effect of iAb treatment (Fig. 15B). Similarly, there is no effect of Happ1 treatment in DARPP-32 intensity in BACHD mice (Fig. 15C).

Treatment with V_L12.3 or Happ1 reduces mHtt aggregation in the lentiviral and R6/2 HD models. Coronal sections from mHDx-1 lentivirus-injected animals 6 weeks post-surgery (Fig. 16A) and10 week-old R6/2 mice (Fig. 16B) were stained for Htt. Most of the Htt staining in both models was in the form of aggregates, although some diffuse staining in neurons is seen (arrows in left panel in Fig. 16A). V_L12.3 or Happ1 treatment reduces aggregates and increases the level of diffuse Htt, both in neuronal somas (arrows) and in the neuropil (Fig. 16A). The larger areas of bright staining in both the Happ1- and V_L12.3-treated R6/2 brains appear to represent neuronal cytoplasm (Fig. 16B). Happ1-treated brains appear to display lower overall levels of Htt staining in both HD models though this was not quantified. To quantify aggregation in the lentiviral model, 3 sections per animal were stained with MW8, an anti-Htt antibody that labels aggregated but not diffuse Htt. Striatal MW8-positive foci were counted and normalized to the area of HDx-1 transduction (Fig. 16C). Treatment with V_L12.3 or Happ1 dramatically reduces mHDx-1 aggregates. To quantify small neuropil aggregates in the R6/2 model, 3 sections per animal were stained with MW8 and toto-3 iodide nuclear marker. MW8-positive foci of 2-8 pixels in size that do not co-localize with toto-3 iodide in a 250 μm^2 area of the transduced striatum were counted (Fig. 16D). Treatment with V_L12.3 or Happ1 dramatically reduces the number of these neuropil aggregates. To quantify intra-nuclear inclusions, MW8-positive foci of 9-15 pixels in size that co-localize with toto-3 iodide staining were counted (Fig. 16E). There is a trend toward a reduction of intra-nuclear inclusions in V_L12.3-treated animals, and a significant

reduction in Happ1-treated animals. Htt inclusions are not observed in YAC128 or BACHD brains. This is not surprising as inclusion formation has been reported to begin at 12 months of age in YAC128 mice (Slow et al., 2005) and between 12 and 18 months of age in BACHD mice (Gray et al., 2008).

Happ1 treatment reduces ventricular enlargement in three transgenic HD models. Ventricular enlargement has been reported in R6/2 mice beginning at 3 weeks of age (Stack et al., 2005) and in 9 and 12 month-old YAC128 mice (Slow et al., 2003). Ventricle size was assessed in 10 week-old R6/2 and WT littermates (Fig. 17A, B), in 7 month-old Yac128 and WT littermates (Fig. 17C), and in 6 month-old BACHD mice (Fig. 17D). Compared to WT littermates, GFP- and V_L12.3-treated R6/2 mice display ventricular enlargement. Happ1 treatment reduces ventricle size to a level not significantly different from WT animals (Fig. 17A, B). Compared to WT littermates, GFP- and V_L12.3-treated YAC128 mice display ventricular enlargement while Happ1 treatment reduces ventricle size (Fig. 17C). In addition, Happ1-treated BACHD mice also display smaller ventricles than GFP-treated BACHD mice (Fig. 17D).

DISCUSSION

AAV is a very promising candidate vector for gene therapy in humans. Wild type AAV is widespread in human populations with 80-85% of adults being seropositive reducing the probability of host immune activation complications (Chirmule et al., 1999; Peel and Klein, 2000). It is non-pathogenic in humans and unable to replicate in the absence of a helper virus. Clinical trials using AAV

to treat neurodegenerative diseases in the human CNS have demonstrated no pathology related to the vector (McPhee et al., 2006; Kaplitt et al., 2007; Marks et al., 2008). AAV can infect both dividing and non-dividing cells and is capable of eliciting long-term transgene expression, which has been monitored for up to six years in primates (Klein et al., 2002; Bankiewicz et al., 2006). Although wtAAV commonly integrates into genomic DNA at specific sites, integration events for recombinant AAV (rAAV), which lacks 96% of the viral genome, are rare, reducing the probability of oncogenic complications (Schnepp et al., 2003). The existence of over 120 different capsid proteins also confers a wide range of tropisms allowing customization of rAAV gene therapy vectors (Mueller and Flotte, 2008).

AAV2 is the most common serotype found in humans. As a result, most early AAV gene therapy studies use this serotype. Although the AAV2 genome is capable of long-term gene expression, due to the AAV2 capsid protein this serotype has low transduction efficiency, low viral spread in the CNS as well as an inability to transduce non-neuronal cell types (McCown et al., 1996; Bartlett et al., 1998; Klein et al., 1998; Tenenbaum et al., 2000). Due to the similarity between inverted terminal repeats (ITRs), the AAV2 genome can be packaged into the capsid proteins of other AAV serotypes. Chimeric AAV2/1, consisting of the AAV2 genome and the AAV1 capsid protein, exhibits increased spread, transduction efficiency, and the ability to transduce glial and ependymal cells as well as neurons, while retaining the long-term expression capabilities of AAV2

(Wang et al., 2003a). Chimeric AAV2/1 also has a decreased lag time between infection and transgene expression (Auricchio et al., 2001).

Traditional AAV gene therapy vectors use the high expressing CMV promoter. However, gene expression from this promoter in AAV infected cells in the CNS declines over time (McCown et al., 1996; Klein et al., 1998; Tenenbaum et al., 2000). This decline is attributed to a combination of loss of non-integrated vector, death of infected cells, or 5' CpG methylation of the CMV promoter leading to silencing (Prösch et al., 1996). Use of the CBA promoter stabilizes gene expression in AAV infected cells in the CNS (Klein et al., 2002). Therefore, for our iAb gene therapy studies we have used a chimeric AAV2/1 vector, consisting of the AAV2 genome under the control of the CBA promoter and the AAV1 capsid. We observe extensive striatal iAb expression for at least 8 months (the longest post-surgical experimental time point).

V_L12.3 treatment results in improved behavior and neuropathology in the lentiviral mouse model of HD. However, in transgenic HD models, V_L12.3 either has no effect or adverse effects on symptoms. Perhaps the presence of V_L12.3 prior to or at the same time as the introduction of mHtt is required for beneficial effects of this intrabody. Conversely, the negative effects of V_L12.3 i.e. stabilizing soluble mHtt and increasing its nuclear localization may have detrimental effects in longer term studies such as the gene therapy studies in transgenic models.

Happ1 treatment, while equally beneficial to the lentiviral model, also improves motor and cognitive performance as well neuropathology in the

transgenic models. In the lentiviral model, Happ1 treatment prevents the amphetamine-induced rotation phenotype and reduces striatal lesion size and intensity as well as aggregation. Happ1 treatment increases body weight and survival of N171-82Q but not R6/2 mice. The lack of effect in the R6/2 may be related to the extremely early onset and severity of symptoms in this model. Body weight was not affected by iAb treatment in YAC128 or BACHD mice though these mice exhibit progressive weight gain uncharacteristic of human HD. Happ1 treatment improves rotarod and beam crossing performance in all four transgenic models. Unlike the other three models, the improvement to YAC128 motor performance is most significant at the earliest time points. Indicating a beneficial effect of Happ1 on the motor task learning deficit of this model. A climbing test was performed on the full-length transgenic models as a way to test motor performance independent of learning ability as this behavior is spontaneous and does not require training. Happ1 treatment increased climbing time of both YAC128 and BACHD mice. Both full-length transgenic models exhibit anxiety in the open field and deficits in spatial and cortical learning tasks. Happ1 treatment normalizes open field exploration in both models as well as learning in the YAC128 model.

Like V_L12.3 treatment, Happ1 treatment reduces mHDx-1 aggregates and inclusions in the R6/2 model. The similar effect of these iAbs on aggregation is particularly interesting as Happ1 ameliorates and V_L12.3 exacerbates the HD like phenotype in these mice. This indicates that simply preventing aggregation is not predictive of therapeutic benefit. Striatal atrophy resulting from neuronal

shrinkage and/or death and concomitant ventricular enlargement is common to human HD patients as well as all four transgenic models used in this study. Happ1 treatment decreases ventricle enlargement in R6/2, YAC128 and BACHD mice. DARPP-32 intensity, aggregation and ventricle size were not assessed in N171-82Q mice as they were used to study survival and thus euthanized at the same disease stage rather than the same age.

The overwhelmingly beneficial effects of Happ1 treatment on all five mouse models of HD supports the idea that therapies directed at the specific degradation of mHtt represent a direct and effective strategy for the treatment of HD with a low probability of off-target effects.

MATERIALS AND METHODS

Lentivirus production and purification. Ten 15 cm plates of ~80% confluent 293 GPG cells (Ory et al., 1996) were triple transfected by calcium phosphate with 20 μg pFugW lentiviral genome encoding either mHDx-1Q103-GFP or GFP, 15 μg Δ8.9 and 10 μg VSV-G plasmids (Naldini et al., 1996). Sixteen hrs post-transfection, medium was removed and replaced with medium supplemented with 2% FBS. Medium containing lentivirus was collected at 48 and 72 hrs post-transfection, filtered at .45 μm and centrifuged for 90 min at 25,000 RPM at 4^{o}C to pellet lentivirus. Pellets were then dissolved overnight at 4^{o}C in sterile PBS. Viral solutions were buffer exchanged into sterile saline (0.9% NaCl) and concentrated using Amicon ultra 4 ml tubes (MWCO 100,000)(Millipore, Billerica, MA) until a final volume of 150-250 μl was reached,

aliquotted, and stored at –80°C until use. Viral titer was determined by infection of HEK 293 cells with a dilution series and counting colonies of GFP-positive cells. Before injection, all lentiviruses were adjusted to a titer of $5x10^8$ pfu/ml.

AAV production and purification. Fifty 15 cm plates of ~80% confluent HEK 293 cells were triple transfected by calcium phosphate with 12.5 μg AAV serotype 2 genome (Stratagene, La Jolla, CA) with a modified CBA promoter encoding GFP, V_L12.3 or Happ1, 25 μg pHelper (Stratagene) and 37.5 μg AAV serotype 1 rep/cap (University of Pennsylvania viral vector core) plasmids per plate. Medium was replaced 16 hrs post-transfection. At 48 hrs post-transfection, medium was removed and cells were dislodged by pipetting, collected by centrifugation, washed with and re-suspended in 10 mM tris buffer. Cells were lysed by two rounds of freeze/thaw with vortexing and treated with DNAse I for 30 min. at 37°C. The viral fraction was then isolated by ultracentrifucation at 40,000 RPM for 2 hr at 4°C in an optiprep gradient (15-60%)(Sigma). The fraction containing the virus (40-60% interface) was collected by syringe, diluted 1:5 in 20mM tris buffer, pH 8.0 and further purified by Mustang-Q membrane ion exchange (Acrodisc, Pall corporation, East Hills, NY). Virus was eluted in 500 μl 20mM tris buffer, pH8.0 with 400 mM NaCl and stored at –80°C in 50μl aliquots. Before use each aliquot was dialyzed in a slide-a-lyzer mini dialysis unit (MWCO 7000, Pierce) for 1 hr at 4°C in 1 L sterile saline with gentle stirring. Viral titer was determined by qPCR of a dilution series using primers that recognize the inverted terminal repeats and comparison to AAV of a known titer obtained from the University of Iowa viral vector core. Prior to

injection, all AAVs were adjusted with sterile saline to a titer of $1x10^{13}$ viral particles/ml.

Animals. Mice were obtained from the Jackson laboratory (C57Bl/6 and BACHD (through W. Yang lab)) or bred in the Caltech facility from breeding pairs obtained from the Jackson laboratory (R6/2, N171-82Q and YAC128). Due to the infertility of the R6/2 line, ovarian transplant hemizygote females and WT males were used. Wild type females and hemizygote males were used for mating in the N171-82Q and YAC128 lines. Genotyping PCR was performed as specified on the Jackson laboratory website. Mice were housed in ventilated cages and all surgical and experimental procedures were carried out according to Institute Animal Care and Use Committee specifications.

Surgeries. Adult mice were anesthetized with 500 mg/kg ketamine and 100 mg/kg xylazine and placed in a sterotaxic frame. After shaving and disinfecting the scalp, an incision was made along the midline. A dental drill was used to make a burr hole at 0.75 mm anterior and 2 mm lateral to bregma. Injections were done at a depth of 3.5 mm from the dura using a 5 μl Hamilton syringe and removable 30-gauge needle with a 20^{o} bevel tip attached to an ultra micropump III and micro4 controller (World Precision Instruments, FL). After injection, the needle was left in place for five minutes and withdrawn slowly. Incisions were closed using vet bond glue (3M, St Paul, MN) and mice were allowed to recover on a heating pad. Mice were checked for general health daily for three days following surgery.

For the lentiviral model, four week-old C57Bl/6 mice were injected unilaterally in the striatum on alternating sides with 4 μl mHDx-1 or GFP lentivirus plus 1 μl GFP, V_L12.3 or Happ1 AAV at a rate of .5 μl/min (10 mice per group). Four week old male N171-82Q and WT littermates were injected bilaterally in the striatum with 1 μl of GFP or Happ1 AAV followed by 4 μl sterile saline at a rate of 0.5 μl/min (10 mice per group). The needle was loaded first with saline and then with virus so that saline is injected after the virus and serves to push virus into the brain, increasing spread. Two month-old male YAC128 and WT littermates were injected bilaterally in the striatum with 1μl GFP, V_L12.3 or Happ1 AAV followed by 4 μl sterile saline at a rate of 0.5 μl/min (10 mice per group). Two month-old male and female BACHD mice were injected bilaterally in the striatum with 1 μl of either GFP or Happ1 AAV followed by 4 μl sterile saline at a rate of 0.5 μl/min (5 females and 4 males per group).

Postnatal day 3 male R6/2 and WT littermates were anesthetized by hypothermia by submersion in ice water inside a latex glove for five minutes. Pups were then placed on an ice pack with their heads stabilized in a putty mold for the duration of the surgery. After disinfecting the scalp, a 5 μl Hamilton syringe with a removable 33-gauge needle with a 20^o bevel tip was pushed through the skin and skull at approximately the center of each forebrain hemisphere to a depth of 2.5 mm. Bilateral injections of 1 μl GFP, V_L12.3 or Happ1 AAV at a rate of 0.1 μl/min were performed using an ultra micropump III and micro4 controller. The needle was left in place for an additional five minutes and withdrawn slowly. Pups were allowed to recover on a 37^o water circulating

heating pad, and a small amount of the dam's urine was rubbed on their rump to prevent subsequent cannibalism. Pups were checked for the presence of a milk spot two hours after surgery and for general health daily for three subsequent days. After weaning, genotyping was performed to determine how many mice from each of the 6 groups had been injected until a minimum of 20 per group was reached. Ten mice per group were sacrificed for histology at 10 weeks of age while the remaining mice were studied until the point of mortality.

Behavioral assays. All behavioral experiments were conducted during the light cycle by a researcher blind to genotype and treatment group. Repeated tests were conducted at approximately the same time of day. Single time point behaviors were compared using ANOVA. Repeated behavior tests were compared using repeated measures ANOVA for lines where all animals were sacrificed at the same age (YAC128 and BACHD) and 2 way ANOVA at individual time points for lines where animals were tested until a disease related endpoint was reached and therefore not sacrificed at the same age (R6/2 and N171-82Q). Bonferroni post-hoc tests were used to determine significance.

Amphetamine-induced rotation. Mice were injected i.p. with 10 mg/Kg amphetamine in sterile saline and placed in a 50x50 cm open white plexiglass box with 16 cm sides. Activity was recorded for 30 minutes beginning 5 minutes after amphetamine injection by a ceiling-mounted video camera. The number of ipsilateral rotations was counted. Only rotations with a diameter similar to the animal's body length or smaller (as opposed to large circles around the edge of the box) were scored.

Rotarod. The latency to fall from an accelerating rotarod (Ugo Basile,Italy) beginning at 5 RPM and accelerating to 40 RPM over 240 seconds was scored. Mice were allowed to stay on the rotarod for a maximum of 300 seconds. Mice were trained prior to the initial test for 2 consecutive days for R6/2, N171-82Q and YAC128 lines, and 3 consecutive days for the BACHD line. Two trials were performed per training day with a 10 minute ITI. On testing days, 2 trials were performed separated by a 10 minute ITI. Only the second trial was scored.

Beam Crossing. The time to cross the center 80 cm of a 1 m beam was scored. Three square beams of different widths were used (28 mm, 12 mm, and 6 mm). The beams were mounted atop poles (50 cm above the tabletop) with a bright light at the starting end and a dark box containing the animal's home cage nest material at the far end. A nylon hammock 7.5 cm above the tabletop was used to prevent injury to mice falling from the beam. Mice were placed at the end of the beam with the bright light and the time from when the entire body of the mouse entered to the time that the nose of the mouse exited the center 80 cm was measured using an electronic infrared interrupt sensor. The 80 cm section is used because the mice sometimes hesitate before starting and before entering the dark box. Mice were trained prior to the initial test for 3 consecutive days on all beams with a 10 minute ITI between beams. During training, mice were encouraged to keep moving across the beam by nudging and tail pinching. Training trials were repeated until each animal crossed the beam 3 times without stopping or turning around. On testing days, 3 trials were performed per mouse for each beam with a 10 minute ITI between beams. Trials in which the animal

took longer than 60 s to cross or fell off the beam were scored as 60 s. Trials in which the animal stopped or turned around were repeated. The average of the trials was scored.

Climbing. Mice were placed at the bottom end of a closed topped wire mesh cylinder (10x15 cm) on the tabletop and recorded with a video camera for 5 minutes. The time from when a mouse's fourth foot left the tabletop to the time when the first foot was replaced on the tabletop was scored as time spent climbing. The sum of climbing time for the 5 minute trial was compared.

Clasping. Animals were suspended by the tail approximately 30 cm above the tabletop for 1 min and recorded with a video camera. No clasping was scored as 0, front limb clasping was scored as 1, and hind limb clasping was scored as 2.

Open field, novel object, novel object location and novel object preference. Mice were placed in the lower left corner of a 50x50 cm open white plexiglass box with 16 cm sides in a room brightly lit by fluorescent ceiling lights. Open field activity was recorded for 10 minutes by a ceiling-mounted video camera. Center entries and time spent in the center were scored. Mice were then removed from the box for a 5 minute ITI and two different novel objects were placed in the upper two corners of the box, far enough from the sides so as to not impede movement around the outer edge (approximately 7 cm). The mouse was re-introduced to the box in the lower left corner and recorded for 5 minutes during which the number of investigations of the novel objects was scored. Episodes involving the mouse in close proximity to the objects but not

facing or sniffing them were not considered investigations. Circling or rearing on the objects with continued sniffing was considered a single investigation while episodes in which the mouse sniffed the object, turned away or reared against the wall and subsequently turned back to sniff the object again were considered separate investigations. Combined investigations of both objects were scored for novel object testing. Mice were then removed from the box a 5 minute ITI and the object at the top right corner of the box was moved to the lower right corner of the box. Mice were re-introduced to the box and recorded for 5 minutes, and the number of investigations of the objects was scored. For novel object location testing, the percent of investigations of the target object (the one in the new location) was computed. For novel object preference testing, the experiment was repeated on the subsequent day with the exception that rather than moving the position of the object in the top right corner, it was replaced by a different, unfamiliar object in the same location. The percent of investigations of the target object (the unfamiliar one) was computed.

Survival. When animals became obviously ill, they were assessed twice daily for the loss of righting reflex. If animals failed to right themselves immediately after being laid on their side in the home cage they were euthanized.

Histology. Brain tissue was fixed by transcardiac perfusion of 4% PFA in PBS. Brains were post-fixed in ice cold 4% PFA in PBS for 45 minutes and then placed in 30% sucrose at 4^{o}C overnight until they sunk. Brains were then embedded in optimal cutting temperature (OCT) embedding medium and cut in 16 μm slide mounted coronal sections. Sections were stored at –20^{o}C until

immunohistochemistry (IHC). For IHC, sections were blocked for 30 minutes at room temperature in 3% BSA, 10% normal goat serum, 0.1% triton-X100 and .02% sodium azide in PBS. Antibodies were diluted in the blocking solution. Primary antibodies were incubated on sections overnight or for 48 hrs (anti-HA) at 4^{o}C. Secondary antibodies were incubated on sections for 2 hrs at room temperature. Primary antibodies used include rabbit anti-DARPP-32 (1:500, Chemicon, Billerica, MA), mouse anti-Htt MW8 (Ko et al., 2001),mouse anti-Htt EM48 (1:1000, Chemicon), rabbit anti-GFP (1:400, Invitrogen), mouse anti-NeuN (1:500, DAKO, Carpinteria CA), rabbit anti-GFAP (1:500 Chemicon) and mouse anti-HA (1:200, Covance, Princeton, NJ). Secondary antibodies used include Alexa-fluor 350 (blue)-, 488 (green)- and 568 (red)-labeled goat anti-mouse or anti-rabbit (1:250, Invitrogen). Topro-3 iodide nuclear stain (Invitrogen) was incubated at 1:5000 in PBS for 5 min at RT after secondary antibody. Animals with less than 50% of the striatal area transduced at 0.75 mm anterior to bregma were eliminated from all behavioral and histological analyses. Quantification of IHC was compared using 2 way ANOVA and Bonferroni post-hoc tests for significance.

Lentiviral HD model. Three sections per mouse selected from the anterior region of the forebrain (1.7-2 mm anterior to bregma), the injection site (0.75 mm anterior to bregma), and the posterior region of the forebrain (0.8-1 mm posterior to bregma) were stained for GFP (green) and HA (iAb, red) to determine the extent of viral transgene spread. In the case of the iAb-treated groups, these sections were also used to determine the similarity of spread and

co-transduction efficiency of the mHDx-1 lentivirus and iAb AAV. Three sections per mouse selected near the injection site were stained for Htt inclusions (MW8, green), DARPP-32 (red) and all nuclei (blue). Striatal Htt inclusions were quantified by counting green foci larger than 2 pixels at 40X magnification for each section. Striatal DARPP-32 staining was assessed both for the area of the lesion and for the intensity of staining within the lesion. For lesion area, the ratio of the area of total DARPP-32 loss to the area of striatal lentiviral transgene spread was calculated. For staining intensity, the ratio of DARPP-32 (red fluorescence) staining in the transduced area of the injected striatum to DARPP-32 staining in the same area of the contralateral, un-injected striatum was calculated. Image J was used for all three quantifications. To further characterize lesions, 2 sections per mouse were stained for DARPP-32 (red), GFAP (green), and NeuN (blue) or all nuclei (topro-3 iodide, blue).

R6/2 HD model. Three sections per mouse selected from the anterior region of the forebrain, the injection site (~0.75 mm anterior to bregma), and the posterior region of the forebrain from both the group sacrificed at 10 weeks of age and the group used to assess survival were stained for GFP (green), and HA (red) to determine the extent of viral transgene spread. Three sections per mouse at approximately bregma from the group sacrificed at 10 weeks of age were stained for Htt inclusions (MW8, green), DARPP-32 (red), and all nuclei (topro-3-iodide, blue). Small Htt aggregates were quantified by counting green foci 2-8 pixels in size within a 250 μm^2 area of the transduced striatum. Intranuclear inclusions were quantified by counting green foci 9-15 pixels in size

that co-localized with topro-3-iodide staining. DARPP-32 was quantified by mean red fluorescence intensity of the entire striatal area of both hemispheres. Ventricle area was also measured for both hemispheres of these sections by tracing its outline (area computed in arbitrary units). Image J was used for all three of these measures.

N171-82Q HD model. Three sections per mouse selected from the anterior region of the forebrain, the injection site (0.75 mm anterior to bregma), and the posterior region of the forebrain were stained for GFP (green), and HA (red) to determine the extent of viral transgene spread. Neuropathological markers were not assessed for these animals as they were used to assess survival and were therefore not euthanized at the same age but at the same disease stage.

YAC128 and BACHD HD models. Three sections per mouse selected from the anterior region of the forebrain, the injection site (0.75 mm anterior to bregma), and the posterior region of the forebrain were stained for GFP (green), and HA (red) to determine the extent of viral transgene spread. Three sections per mouse at approximately bregma were stained for Htt inclusions (EM48, green), DARPP-32 (red), and all nuclei (blue). DARPP-32 was quantified by mean red fluorescence intensity of the entire striatal area of both hemispheres. Ventricle size was also measured for both hemispheres of these sections. Image J was used for these measures.

REFERENCES

Auricchio A, Kobinger G, Anand V, Hildinger M, O'Connor E, Maguire AM, Wilson JM, Bennett J (2001) Exchange of surface proteins impacts on viral vector cellular specificity and transduction characteristics: the retina as a model. Human molecular genetics 10:3075-3081.

Bankiewicz KS, Forsayeth J, Eberling JL, Sanchez-Pernaute R, Pivirotto P, Bringas J, Herscovitch P, Carson RE, Eckelman W, Reutter B, Cunningham J (2006) Long-term clinical improvement in MPTP-lesioned primates after gene therapy with AAV-hAADC. Molecular therapy 14:564-570.

Bartlett JS, Samulski RJ, McCown TJ (1998) Selective and rapid uptake of adeno-associated virus type 2 in brain. Human gene therapy 9:1181-1186.

Chirmule N, Propert K, Magosin S, Qian Y, Qian R, Wilson J (1999) Immune responses to adenovirus and adeno-associated virus in humans. Gene therapy 6:1574-1583.

Emadi S, Barkhordarian H, Wang MS, Schulz P, Sierks MR (2007) Isolation of a human single chain antibody fragment against oligomeric alpha-synuclein that inhibits aggregation and prevents alpha-synuclein-induced toxicity. Journal of molecular biology 368:1132-1144.

Gray M, Shirasaki DI, Cepeda C, André VM, Wilburn B, Lu X-H, Tao J, Yamazaki I, Li S-H, Sun YE, Li X-J, Levine MS, Yang XW (2008) Full-length human mutant huntingtin with a stable polyglutamine repeat can elicit progressive

and selective neuropathogenesis in BACHD mice. The journal of neuroscience 28:6182-6195.

Kaplitt MGMG, Feigin AA, Tang CC, Fitzsimons HLHL, Mattis PP, Lawlor PAPA, Bland RJRJ, Young DD, Strybing KK, Eidelberg DD, During MJMJ (2007) Safety and tolerability of gene therapy with an adeno-associated virus (AAV) borne GAD gene for Parkinson's disease: an open label, phase I trial. Lancet 369:2097-2105.

Khoshnan A, Ko J, Patterson PH (2002) Effects of intracellular expression of anti-huntingtin antibodies of various specificities on mutant huntingtin aggregation and toxicity. Proceeding of the national academy of sciences of the United States of America 99:1002-1007.

Klein RL, Meyer EM, Peel AL, Zolotukhin S, Meyers C, Muzyczka N, King MA (1998) Neuron-specific transduction in the rat septohippocampal or nigrostriatal pathway by recombinant adeno-associated virus vectors. Experimental neurology 150:183-194.

Klein RL, Hamby ME, Gong Y, Hirko AC, Wang S, Hughes JA, King MA, Meyer EM (2002) Dose and promoter effects of adeno-associated viral vector for green fluorescent protein expression in the rat brain. Experimental neurology 176:66-74.

Ko J, Ou S, Patterson PH (2001) New anti-huntingtin monoclonal antibodies: implications for huntingtin conformation and its binding proteins. Brain research bulletin 56:319-329.

Lecerf JJM, Shirley TTL, Zhu QQ, Kazantsev AA, Amersdorfer PP, Housman DDE, Messer AA, Huston JJS (2001) Human single-chain Fv intrabodies counteract in situ huntingtin aggregation in cellular models of Huntington's disease. Proceedings of the national academy of sciences of the United States of America 98:4764-4769.

Mangiarini L, Sathasivam K, Seller M, Cozens B, Harper A, Hetherington C, Lawton M, Trottier Y, Lehrach H, Davies SW, Bates GP (1996) Exon 1 of the HD gene with an expanded CAG repeat is sufficient to cause a progressive neurological phenotype in transgenic mice. Cell 87:493-506.

Marks WJ, Ostrem JL, Verhagen L, Starr PA, Larson PS, Bakay RA, Taylor R, Cahn-Weiner DA, Stoessl AJ, Olanow CW, Bartus RT (2008) Safety and tolerability of intraputaminal delivery of CERE-120 (adeno-associated virus serotype 2-neurturin) to patients with idiopathic Parkinson's disease: an open-label, phase I trial. Lancet neurology 7:400-408.

McCown TJ, Xiao X, Li J, Breese GR, Jude Samulski R (1996) Differential and persistent expression patterns of CNS gene transfer by an adeno-associated virus (AAV) vector. Brain research 713:99-107.

McLear JA, Lebrecht D, Messer A, Wolfgang WJ (2008) Combinational approach of intrabody with enhanced Hsp70 expression addresses multiple pathologies in a fly model of Huntington's disease. FASEB J 22:2003-2011.

McPhee SWJ, Janson CG, Li C, Samulski RJ, Camp AS, Francis J, Shera D, Lioutermann L, Feely M, Freese A, Leone P (2006) Immune responses to

AAV in a phase I study for Canavan disease. The journal of gene medicine 8:577-588.

Miller TWTW, Zhou CC, Gines SS, MacDonald MEME, Mazarakis NDND, Bates GPGP, Huston JSJS, Messer AA (2005) A human single-chain Fv intrabody preferentially targets amino-terminal Huntingtin's fragments in striatal models of Huntington's disease. Neurobiology of disease 19:47-56.

Mueller C, Flotte TR (2008) Clinical gene therapy using recombinant adeno-associated virus vectors. Gene therapy 15:858-863.

Mumby DG, Piterkin P, Lecluse V, Lehmann H (2007) Perirhinal cortex damage and anterograde object-recognition in rats after long retention intervals. Behavioural brain research 185:82-87.

Mumby DG, Gaskin S, Glenn MJ, Schramek TE, Lehmann H (2002) Hippocampal damage and exploratory preferences in rats: memory for objects, places, and contexts. Learning and memory 9:49-57.

Murphy RC, Messer A (2004) A single-chain Fv intrabody provides functional protection against the effects of mutant protein in an organotypic slice culture model of Huntington's disease. Molecular brain research 121:141-145.

Naldini L, BlÃ¶mer U, Gallay P, Ory D, Mulligan R, Gage FH, Verma IM, Trono D (1996) In vivo gene delivery and stable transduction of nondividing cells by a lentiviral vector. Science 272:263-267.

Ory DS, Neugeboren BA, Mulligan RC (1996) A stable human-derived packaging cell line for production of high titer retrovirus/vesicular stomatitis virus G

pseudotypes. Proceedings of the national academy of sciences of the United States of America 93:11400-11406.

Paganetti P, Calanca V, Galli C, Stefani M, Molinari M (2005) {beta}-site specific intrabodies to decrease and prevent generation of Alzheimer's A{beta} peptide. Journal of cell biology 168:863-868.

Peel AL, Klein RL (2000) Adeno-associated virus vectors: activity and applications in the CNS. Journal of neuroscience methods 98:95-104.

Prösch S, Stein J, Staak K, Liebenthal C, Volk HD, Krüger DH (1996) Inactivation of the very strong HCMV immediate early promoter by DNA CpG methylation in vitro. Biological chemistry Hoppe-Seyler 377:195-201.

Schnepp BC, Clark KR, Klemanski DL, Pacak CA, Johnson PR (2003) Genetic fate of recombinant adeno-associated virus vector genomes in muscle. Journal of virology 77:3495-3504.

Shin J-Y, Fang Z-H, Yu Z-X, Wang C-E, Li S-H, Li X-J (2005) Expression of mutant huntingtin in glial cells contributes to neuronal excitotoxicity. Journal of cell biology 171:1001-1012.

Slow EJ, Graham RK, Osmand AP, Devon RS, Lu G, Deng Y, Pearson J, Vaid K, Bissada N, Wetzel R, Leavitt BR, Hayden MR (2005) Absence of behavioral abnormalities and neurodegeneration in vivo despite widespread neuronal huntingtin inclusions. Proceedings of the national academy of sciences of the United States of America 102:11402-11407.

Slow EJ, van Raamsdonk J, Rogers D, Coleman SH, Graham RK, Deng Y, Oh R, Bissada N, Hossain SM, Yang Y-Z, Li X-J, Simpson EM, Gutekunst C-

A, Leavitt BR, Hayden MR (2003) Selective striatal neuronal loss in a YAC128 mouse model of Huntington disease. Human Molecular Genetics 12:1555-1567.

Stack EC, Kubilus JK, Smith K, Cormier K, Del Signore SJ, Guelin E, Ryu H, Hersch SM, Ferrante RJ (2005) Chronology of behavioral symptoms and neuropathological sequela in R6/2 Huntington's disease transgenic mice. Journal of comparative neurology 490:354-370.

Tenenbaum L, Chtarto A, Lehtonen E, Velu T, Brotchi J, Levivier M (2004) Recombinant AAV-mediated gene delivery to the central nervous system. The journal of gene medicine 6:S212-S222.

Tenenbaum L, Jurysta F, Stathopoulos A, Puschban Z, Melas C, Hermens WT, Verhaagen J, Pichon B, Velu T, Levivier M (2000) Tropism of AAV-2 vectors for neurons of the globus pallidus. Neuroreport 11:2277-2283.

Van Raamsdonk JM, Pearson J, Slow EJ, Hossain SM, Leavitt BR, Hayden MR (2005) Cognitive dysfunction precedes neuropathology and motor abnormalities in the YAC128 mouse model of Huntington's disease. The journal of neuroscience 25:4169-4180.

Wang C-E, Zhou H, McGuire JR, Cerullo V, Lee B, Li S-H, Li X-J (2008) Suppression of neuropil aggregates and neurological symptoms by an intracellular antibody implicates the cytoplasmic toxicity of mutant huntingtin. Journal of cell biology 181:803-816.

Wang C, Wang CM, Clark KR, Sferra TJ (2003) Recombinant AAV serotype 1 transduction efficiency and tropism in the murine brain. Gene therapy 10:1528-1534.

Wolfgang WJ, Miller TW, Webster JM, Huston JS, Thompson LM, Marsh JL, Messer A (2005) Suppression of Huntington's disease pathology in Drosophila by human single-chain Fv antibodies. Proceeding of the national academy of sciences of the United States of America 102:11563-11568.

Zhou C, Emadi S, Sierks MR, Messer A (2004) A human single-chain Fv intrabody blocks aberrant cellular effects of overexpressed alpha-synuclein. Molecular therapy 10:1023-1031.

FIGURES

Fig 1

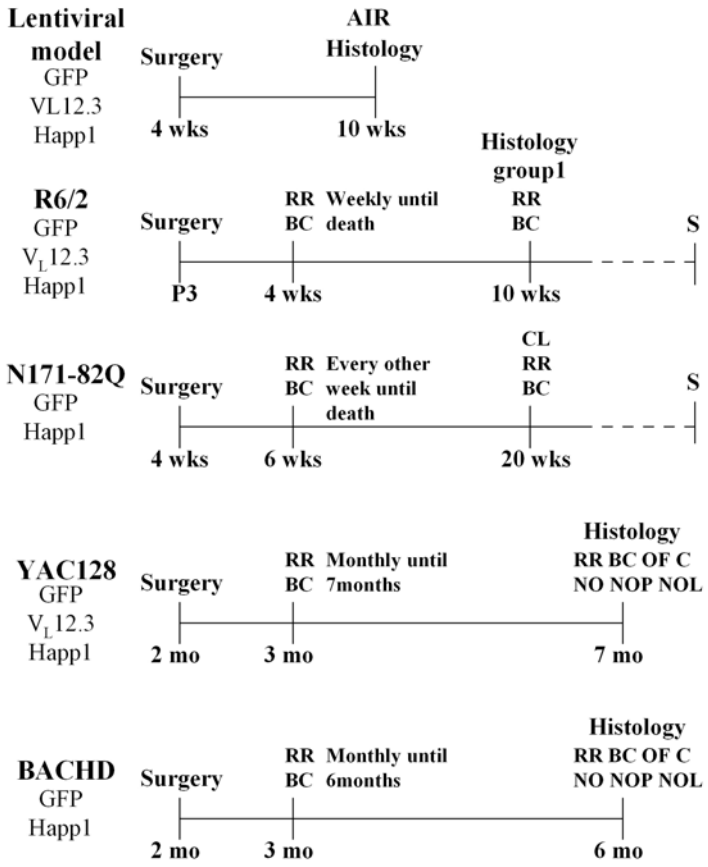

Figure 1. Schematic of intrabody gene therapy experiment in HD mice. Viral vectors used in each case are listed below model names. Abbreviations used: AIR, amphetamine-induced rotation; BC, beam crossing; C, climbing; CL, clasping; NO, novel object; NOL, novel object location; NOP, novel object preference; OF, open field; RR, rotarod; S, survival. Dotted line indicates that RR and BC were continued until death.

Fig 2

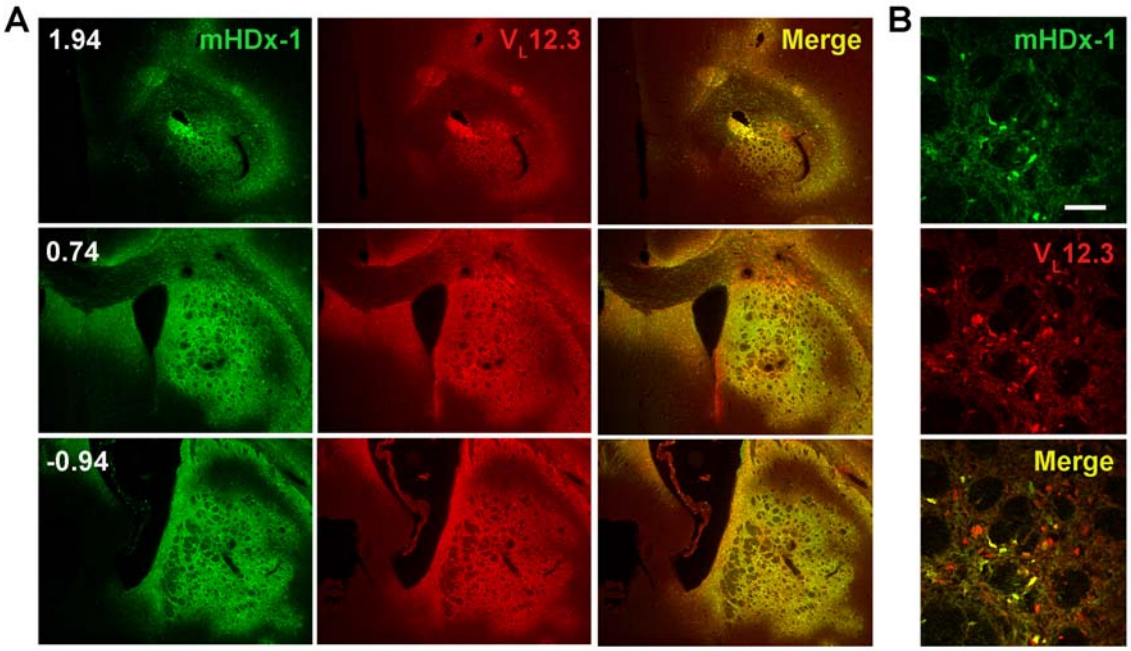

Figure 2. Lentivirus and AAV2/1 vectors co-transduce cells and display similar spread. Coronal sections from a mouse injected unilaterally with a mixture of mHDx-1 lentivirus and V_L12.3 AAV were stained for Htt (green) and intrabody (red). (A) Three different anterior/posterior levels show a similar spread between the two viruses. Numbers indicate mm from bregma. (B) Confocal images show co-localization of mHDx-1 and V_L12.3 with more cells being V_L12.3 positive than mHDx-1 positive, indicating co-transduction of cells and greater transduction efficiency for AAV. scale bar = 50 μm

Fig 3

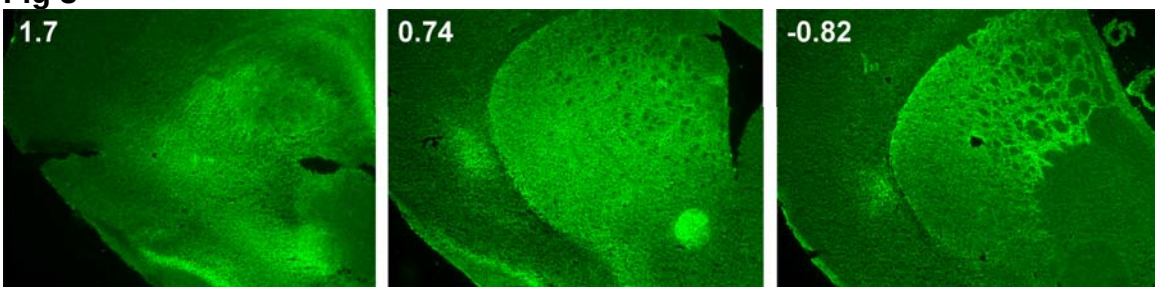

Figure 3. Spread of GFP AAV injected on postnatal day 3. Coronal sections from an R6/2 mouse injected with AAV-GFP on postnatal day 3 and sacrificed at 10 weeks of age. Three different anterior/posterior levels show striatal spread equivalent to, or better than, that seen for adult injections. Numbers indicate mm from bregma.

Fig 4

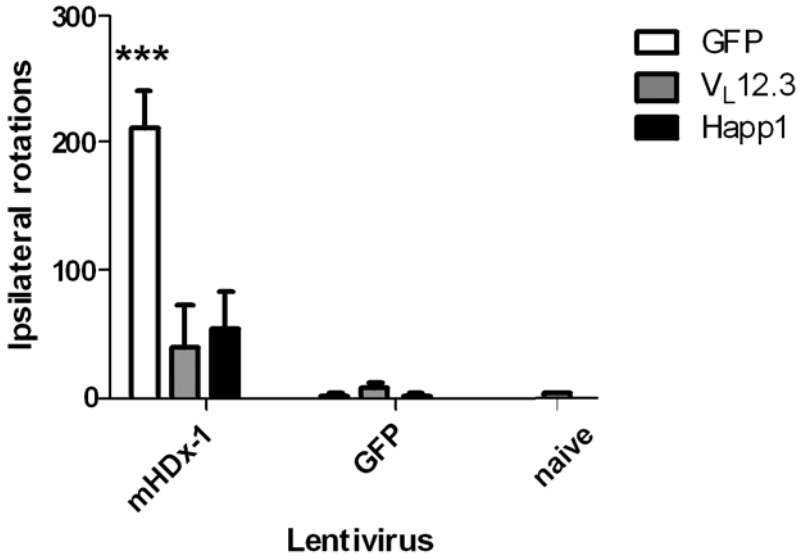

Figure 4. Co-injection of V_L12.3 or Happ1 AAV prevents the amphetamine-induced rotation phenotype caused by mHDx-1 lentivirus. Wild type mice were injected unilaterally at 4 weeks of age with mHDx-1 or GFP lentivirus plus GFP, V_L12.3 or Happ1 AAV. At 10 weeks of age mice were assayed for amphetamine-induced rotation. Un-injected (naïve) animals were tested as a

negative control. Animals injected with mHDx-1 lentivirus and GFP AAV exhibit many ipsilateral rotations in response to amphetamine. V_L12.3 or Happ1 prevents this phenotype. ***=p<.001

Fig 5

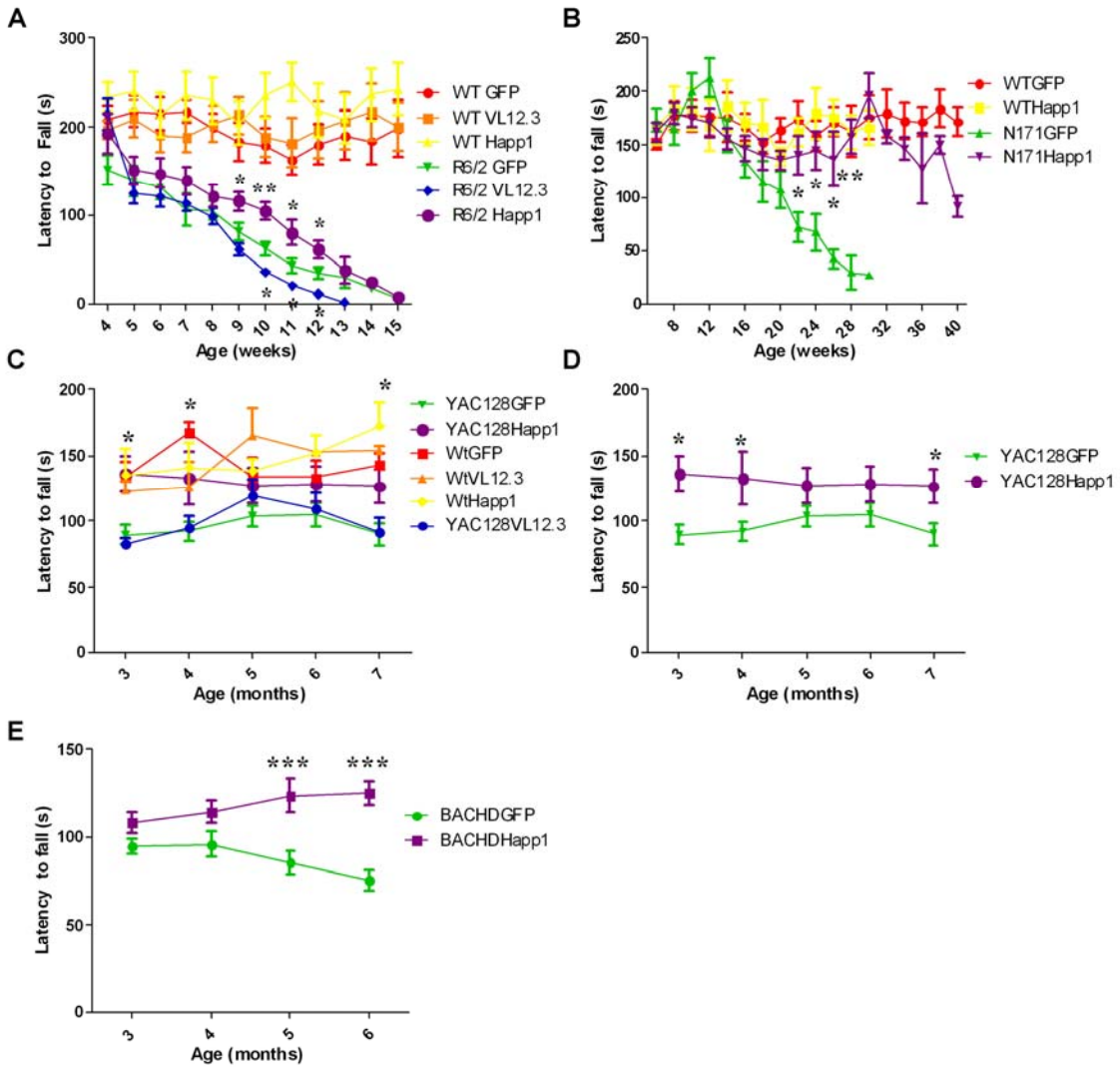

Figure 5. Happ1 treatment improves rotarod performance in four HD mouse models. Mice were tested on an accelerating rotarod for a maximum of 300 seconds. (A) Male R6/2 and WT littermates were tested weekly and Happ1 treatment significantly improves performance during weeks 9-12 while V_L12.3

treatment degrades performance during weeks 10-12. (B) Male N171-82Q and WT littermates were tested every other week. Happ1 treatment improves performance to a level not different from WT animals from 22 weeks until 38 weeks. (C) Male YAC128 and WT littermates were tested monthly and Happ1 (but not V_L12.3) treatment significantly improves performance at months 3, 4 and 7. (D) YAC128 rotarod performance showing only GFP- and Happ1-treated groups. (E) Male and female BACHD mice were tested monthly and Happ1 treatment significantly improves performance at months 5 and 6. Asterisks indicate difference between GFP- and iAb-treated mutants. *=p<.05, **=p<.01, ***=p<.001

Fig 6

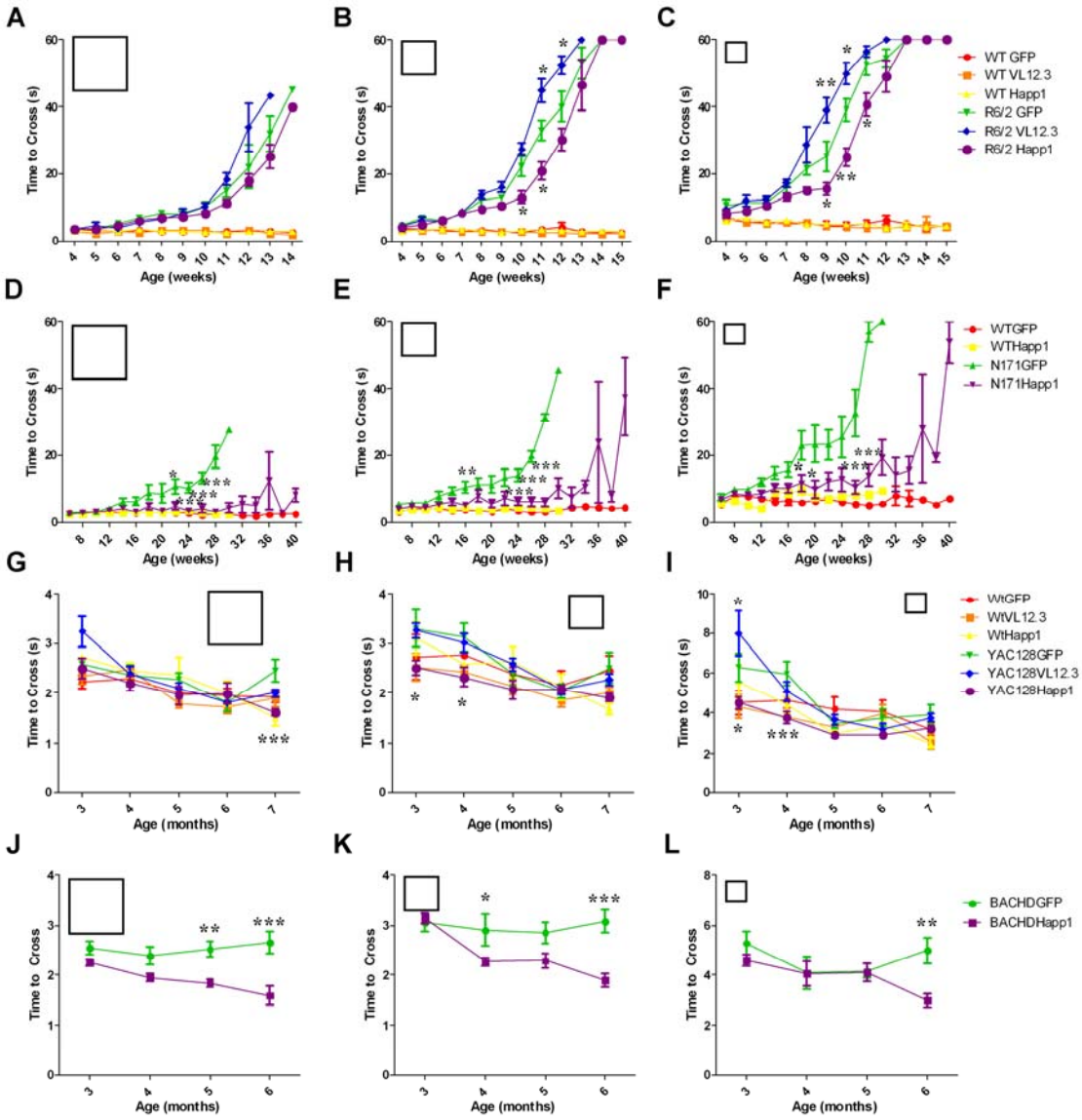

Figure 6. Happ1 treatment improves beam crossing performance in four HD mouse models. Time to cross the center 80 cm of a square 1 m long, 28 mm, 12 mm or 6 mm wide (indicated by the different sizes of open boxes in each panel) beam was measured. (A-C) Male R6/2 and WT littermates were tested weekly, and Happ1 treatment improved while V_L12.3 treatment degraded performance. (D-F) Male N171-82Q and WT littermates were tested every other week and Happ1 treatment improved performance. (G-I) Male YAC128 and WT littermates

were tested monthly, and Happ1 treatment improved performance. (J-L) Male and female BACHD mice were tested monthly, and Happ1 treatment improved performance. Asterisks indicate difference between GFP- and iAb-treated mutants. *=p<.05, **=p<.01, ***=p<.001

Fig 7

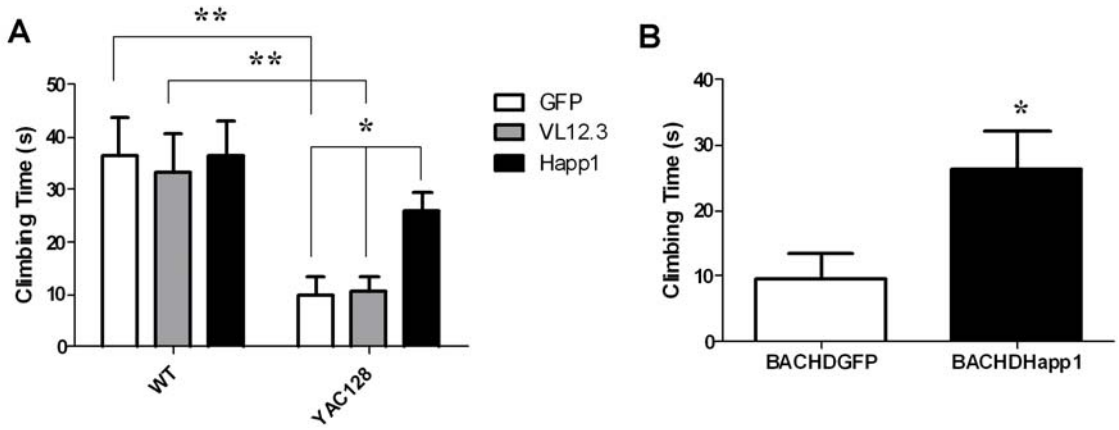

Figure 7. Happ1 treatment improves climbing performance in HD transgenic mice. To assay climbing performance, mice were placed at the bottom of a vertical wire mesh tube and observed for 5 minutes. Time when all four feet were off the ground was scored as climbing time. (A) 7 month old GFP- and V_L12.3-treated YAC128 mice have impaired climbing compared to WT mice. This is rescued by Happ1 treatment. (B) Happ1 treatment improves climbing time in 6 month old BACHD mice. *=p<.05, **=p<.01

Fig 8

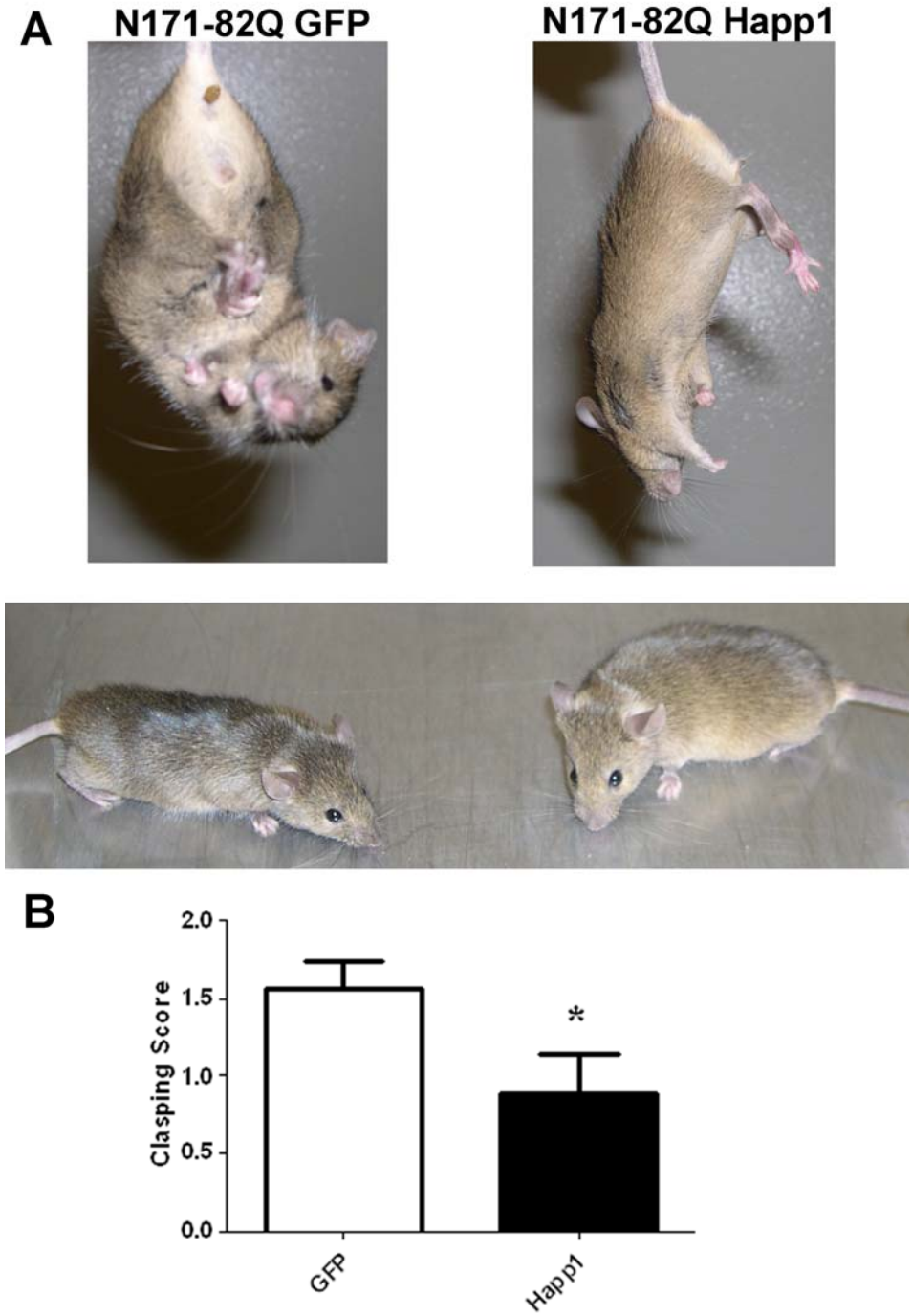

Figure 8. Happ1 treatment reduces clasping in N171-82Q HD mice. (A) The GFP-treated N171-82Q mouse (left) displays forelimb and hind limb clasping and reduced body weight while the Happ1-treated N171-82Q mouse (right) displays normal limb extension and body weight. (B) 20 week old male N171-82Q and WT

littermates were tested for clasping. Mice were suspended by the tail, observed for 1 minute, and given a clasping score as follows: no clasping=0, forelimb clasping=1, hind limb clasping=2. *=p<.05

Fig 9

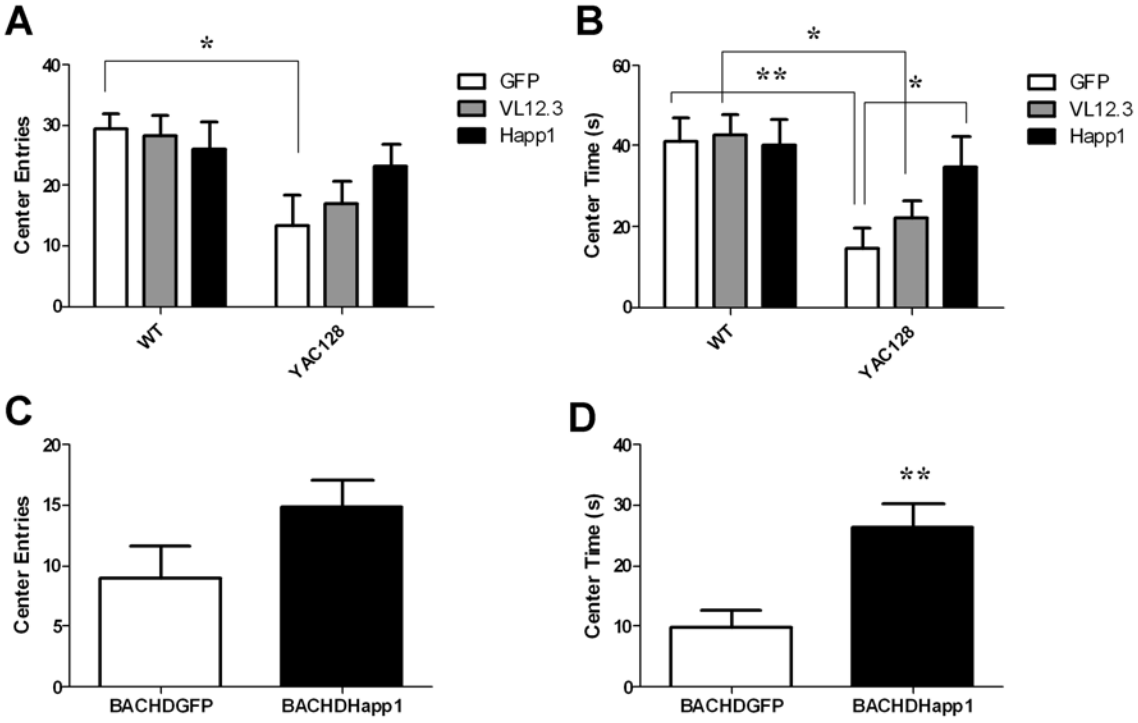

Figure 9. Happ1 treatment normalizes open field behavior in full-length transgenic models of HD. Mice were observed for 10 minutes during exploration of an open field. Anxiety was inferred by scoring entries into, and time spent in, the center of the open field. (A, C) There was a trend toward increased center entries for both models in response to Happ1 treatment, but it was not significant. (B, D) Happ1 treatment increases time spent in the center of the open field in (B) 7 month old YAC128 mice and (D) 6 month old BACHD mice. *=p<.05, **=P<.01

Fig 10

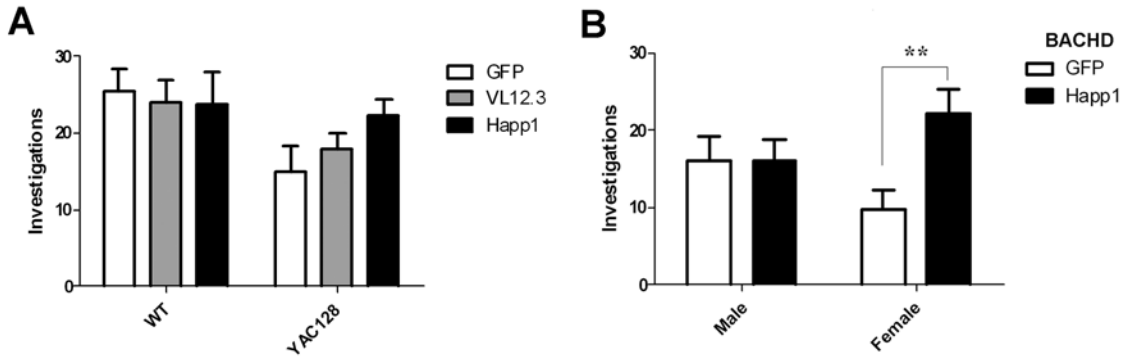

Figure 10. Happ1 treatment increases investigation of a novel object in female BACHD mice. Mice were habituated to an open field for 10 min, removed for 5 min, and then re-introduced to the same field now containing a novel object in each upper corner. Investigation of the novel objects was scored for 5 min. (A) There is a trend toward increased investigation of the novel objects as a result of Happ1 treatment in 7 month old YAC128 mice. (B) Happ1 treatment increases investigation of the novel objects in female but not male 6 month old BACHD mice. **=p<.01

Fig 11

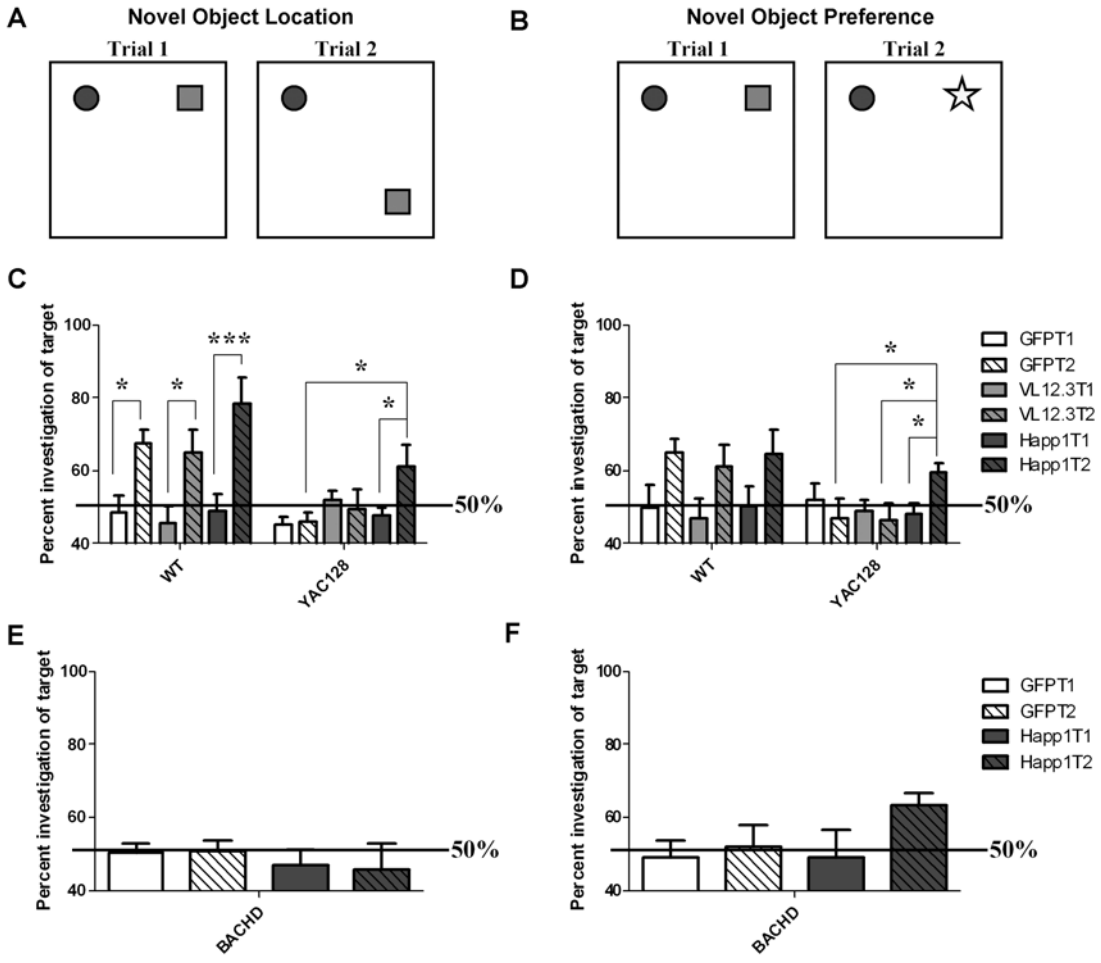

Figure 11. Happ1 treatment improves the learning deficit of YAC128 mice. (A) To assay for preference of a known object in a novel location mice were habituated to an open field for 10 min. After a 5 min inter-trial interval (ITI), they were exposed for 5 min to novel objects in the upper corners of the open field (T1). Investigation of the novel objects was scored. After another 5 min ITI, the mice were re-introduced to the same field with the object previously in the upper right corner moved to the lower right corner (T2) for 5 min. The percent of investigations of the target object (the one in the new location) was scored. A score of 50% would indicate no preference. (B) On the next day mice were tested

for preference for a novel object. Mice were re-habituated to the open field for 10 min. After a 5 min ITI, they were exposed for 5 min to 2 objects in the upper corners of the open field (T1). Investigation of the objects was scored. After another 5 min ITI the mice were re-introduced to the same field with the object in the upper right corner replaced with a completely novel object in the same location. The percent of investigation of the target object (the completely novel one) was scored. A score of 50% would indicate no preference. (C, D) 7 month old YAC128 and WT littermates were tested. WT mice display a preference for the novel object location (C) and a trend toward a preference for the novel object (D). This does not reach significance, but when data from the 3 WT treatment groups is pooled, the preference is significant ($p<.01$). GFP- and $V_L12.3$-treated YAC128 mice show no preference for either object in either paradigm, indicating a learning deficit. Happ1 treatment improves this deficit. (E, F) GFP- and Happ1-treated BACHD mice show no preference for either object in either paradigm. There is a trend toward a preference for the novel object in Happ1 treated BACHD mice, but it does not reach significance. *=$p<.05$, ***=$p<.001$

Fig 12

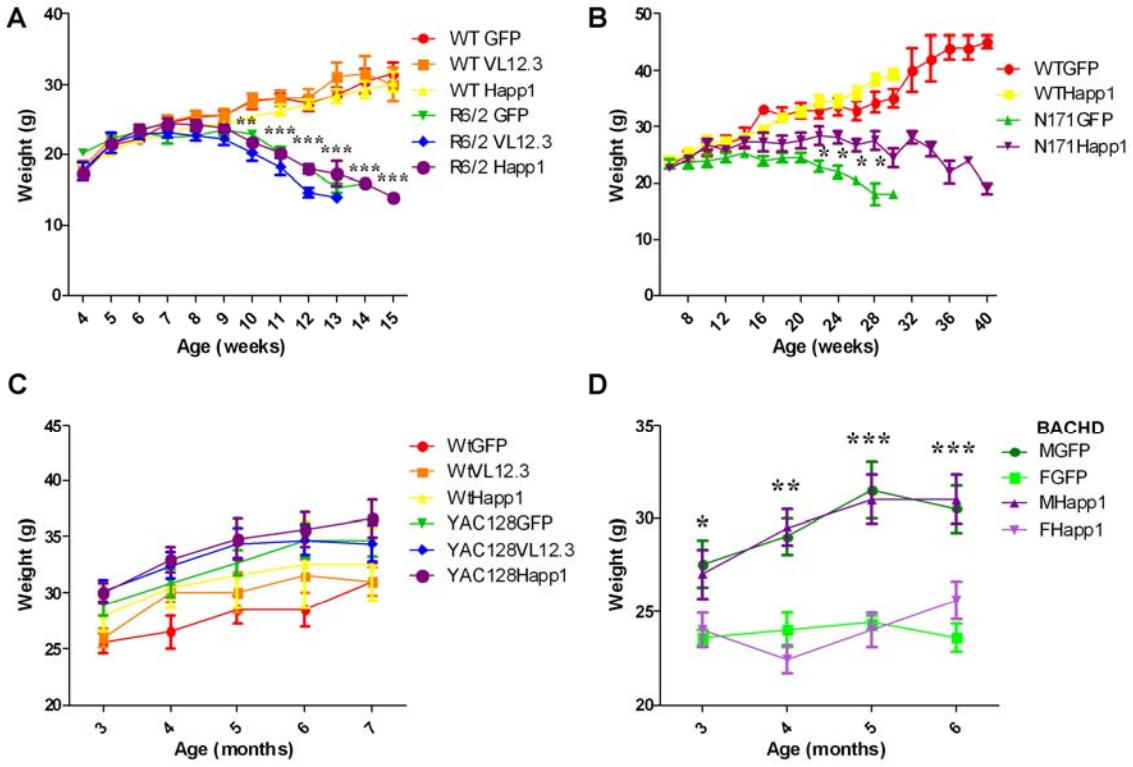

Figure 12. Happ1 treatment improves body weight of N171-82Q mice. (A) While R6/2 mice weigh significantly less than WT mice from 10 weeks of age until death, there is no effect of intrabody treatment. Asterisks indicate difference between GFP-treated WT and R6/2 mice. (B) While Happ1 treated N171-82Q mice weigh less than WT littermates, they also weigh more than GFP treated mutants. Asterisks indicate difference between GFP- and Happ1-treated N171-82Q mice. (C) While YAC128 mice trend toward weighing more than WT mice, there is no effect of intrabody treatment. (D) While male BACHD mice weigh more than female mice, there is no effect of intrabody treatment. Asterisks indicate difference between GFP-treated male and female mice. *=p<.05, **=p<.01, ***=p<.001

Fig 13

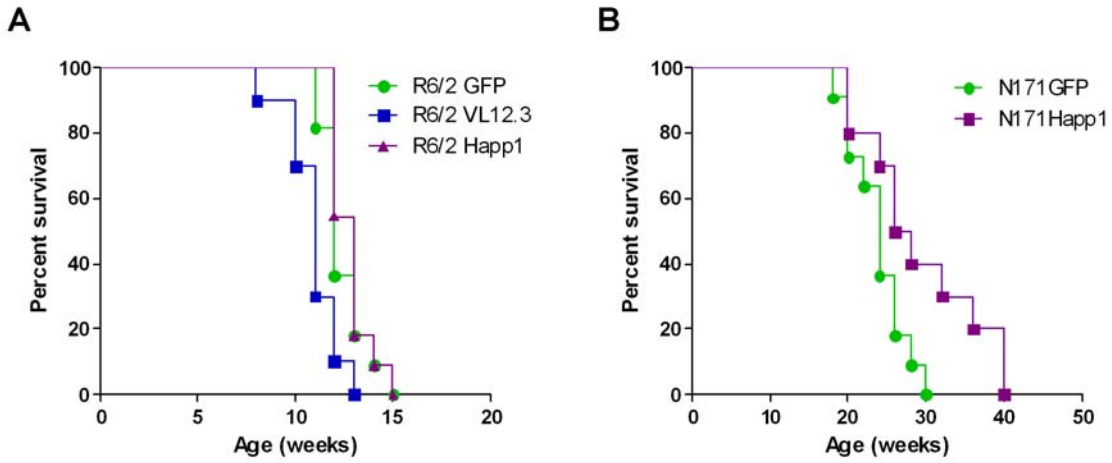

Figure 13. Happ1 treatment increases survival of N171-82Q mice. (A) Happ1 treatment has no effect on while V_L12.3 decreases survival of R6/2 mice. (B) Happ1 treatment increases maximum survival of N171-82Q mice 33% from 30 weeks to 40 weeks of age ($p<.05$).

Fig 14

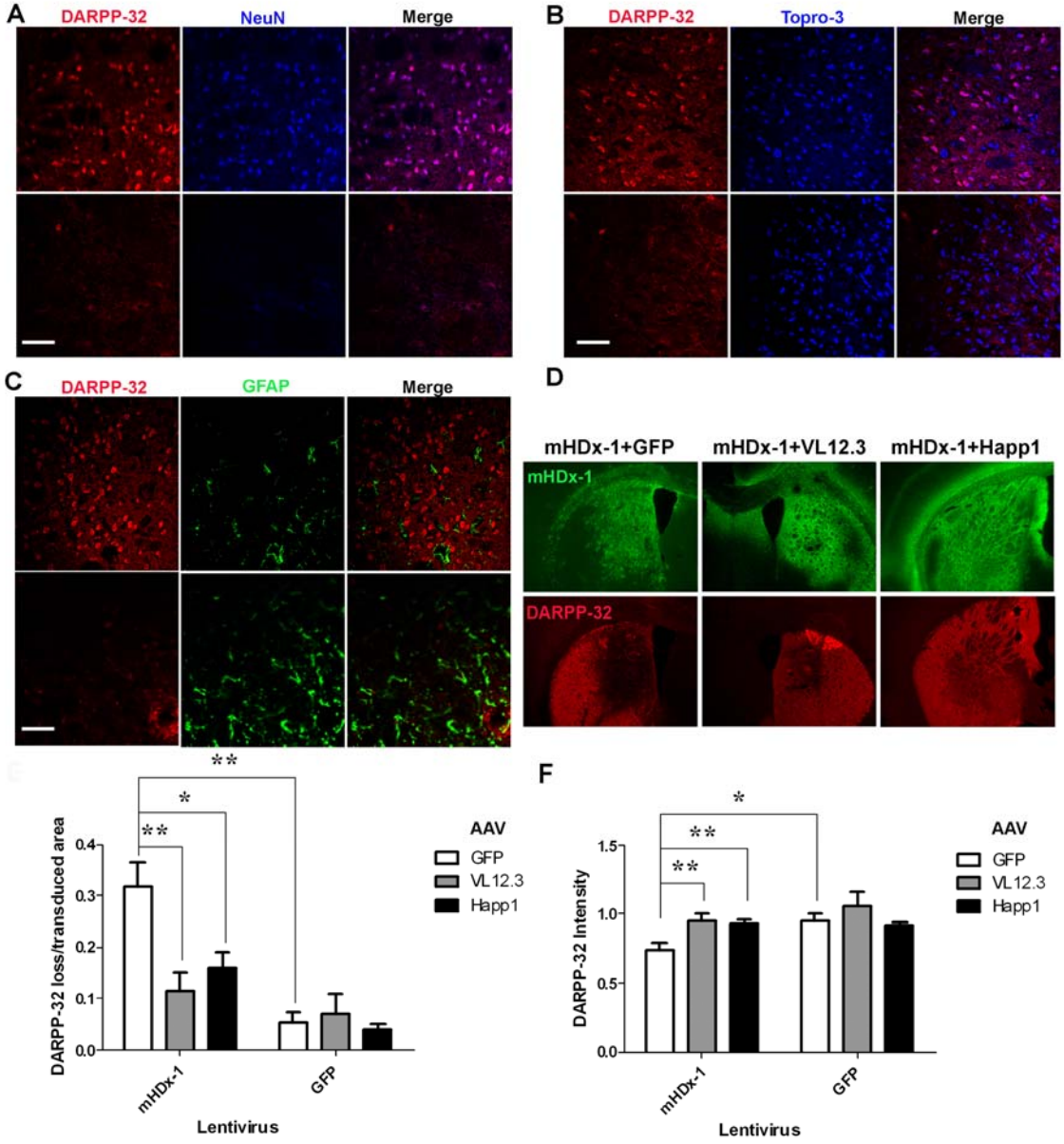

Figure 14. mHDx-1 lentivirus causes neuron-specific toxicity in the striatum, which is reduced by V_L12.3 or Happ1. Mice were injected unilaterally with mHDx-1 or GFP lentivirus plus GFP, V_L12.3 or Happ1 AAV. Areas with loss of DARPP-32 staining were analyzed. (A) Areas of DARPP-32 loss (lower panels) also show loss of NeuN-positive cells, indicating death of neurons in these areas. (B) Topro-3 iodide nuclear stain shows the presence of cells in

lesioned areas, indicating that toxicity is neuron-specific. (C) Areas of DARPP-32 loss show increased GFAP staining, indicating increased inflammation in lesioned areas. (D-F) Co-injection of either Happ1 or V_L12.3 with mHDx-1 reduces the area and intensity of DARPP-32 loss. (D) Adjacent coronal sections stained either for mHDx-1 (green) or DARPP-32 (red). DARPP-32 loss is reduced in the presence of either intrabody. (E) The ratio of the area of total DARPP-32 loss to the transduced area was compared to assess lesion size. Lesions are significantly smaller in the presence of either intrabody. Three sections per mouse were analyzed. (F) The ratio of DARPP-32 staining fluorescence intensity in the transduced area of the striatum to DARPP-32 staining fluorescence intensity in the same sized area of the un-injected striatum was compared to assess the severity of the lesion. Lesions are more severe in the absence of intrabody. Three sections per mouse were analyzed. *=p<.05 **=p<.01, scale bar = 50 μm

Fig15

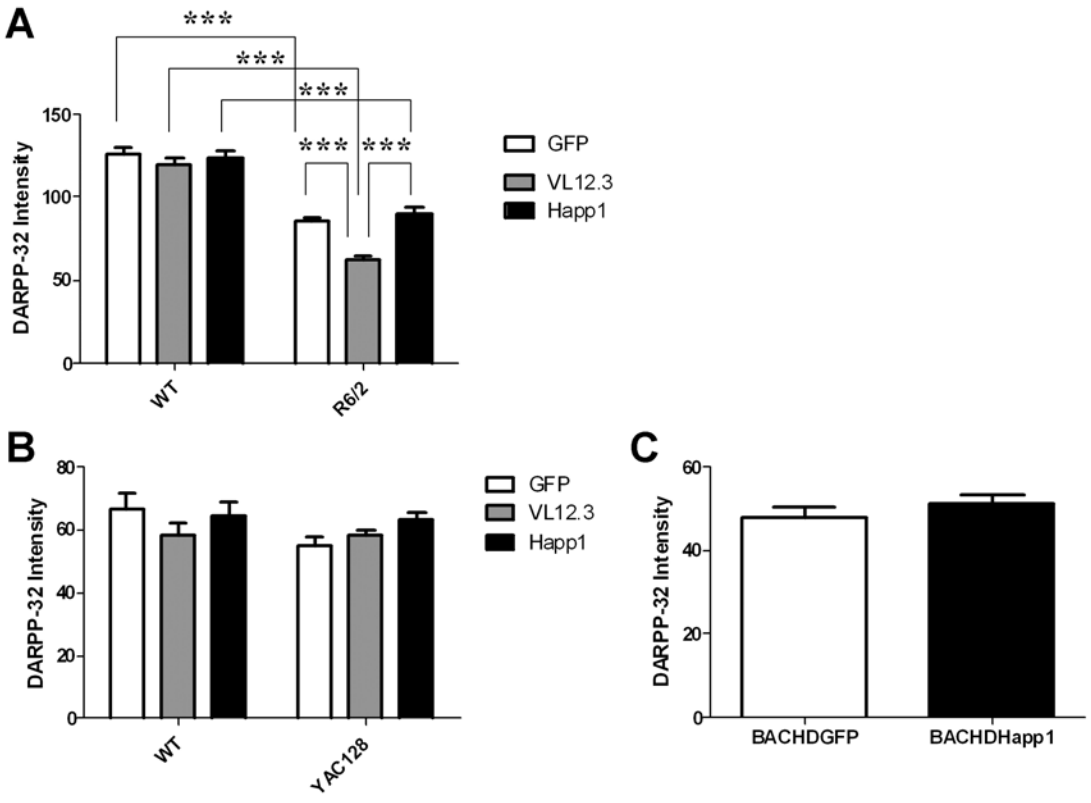

Figure 15. V_L12.3 treatment decreases DARPP-32 staining in R6/2 mice. DARPP-32 staining intensity of the entire striatum in 3 sections each at approximately bregma was measured in (A) 10 week old R6/2 and WT littermates, (B) 7 month old YAC128 and WT littermates, and (C) 6 month old BACHD mice. (A) Compared to WT littermates, R6/2 mice display decreased DARPP-32 staining, which is exacerbated by V_L12.3 treatment. There is no significant loss of DARPP-32 staining and no effect of iAb treatment in (B) YAC128 or (C) BACHD mice. ***=p<.001

Fig 16

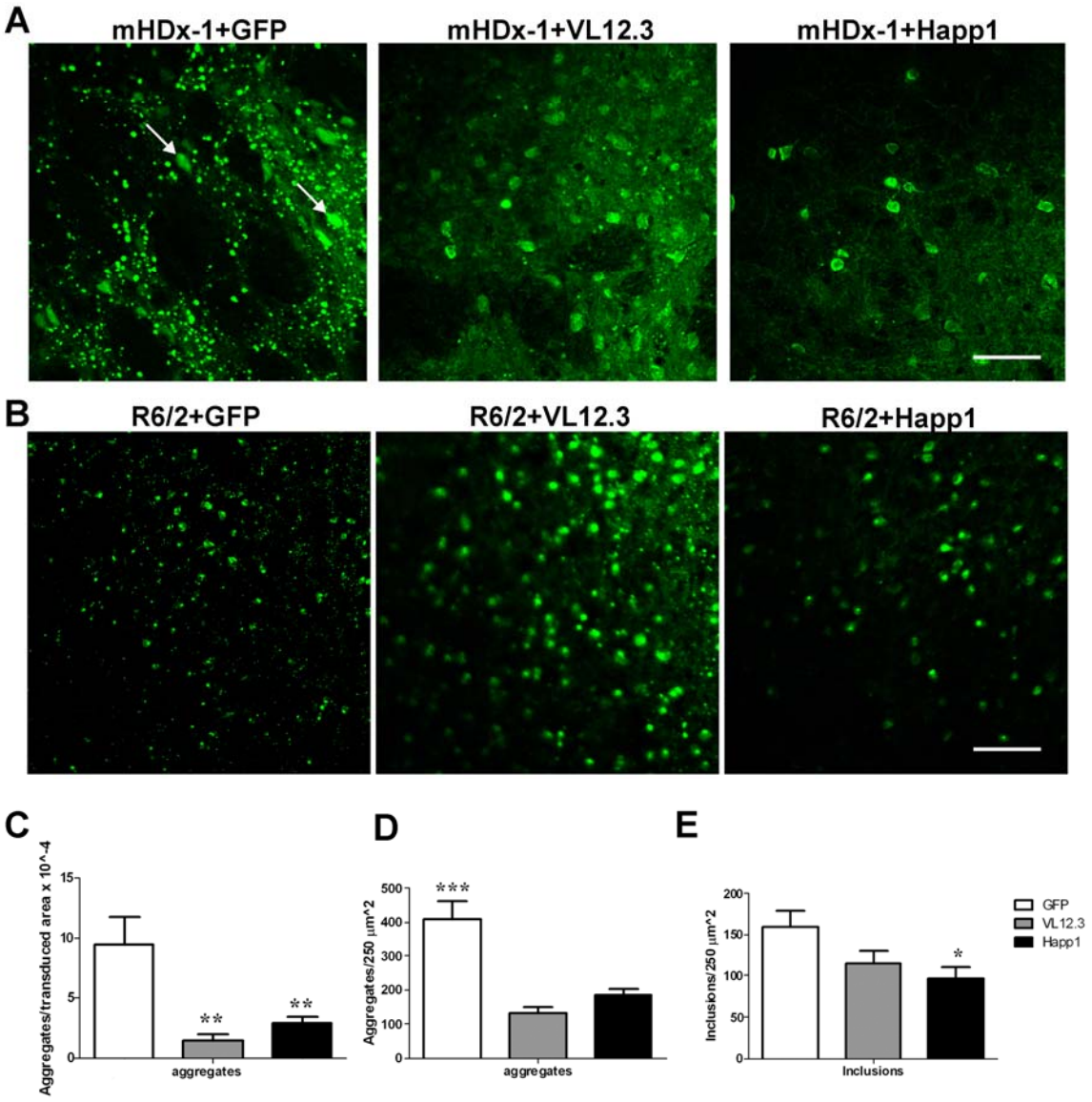

Figure 16. V_L12.3 or Happ1 decreases Htt aggregation in the lentiviral and R6/2 HD models. Three sections each of (A) mHDx-1 lentivirus-injected and (B) 10 week old R6/2 brains were stained for Htt. Following GFP-AAV injection in both models, the majority of the Htt is aggregated although some diffuse staining in neurons is seen (arrows in left panel A). With injection of V_L12.3 or Happ1 there is a reduction in aggregated Htt and an increase in diffuse Htt staining. In the presence of Happ1, total Htt staining appears reduced. (C) The ratio of

striatal aggregates to transduced area is reduced by both intrabodies. (D) The number of small Htt aggregates per 250 μm^2 is reduced by both intrabodies. (E) Happ1 treatment reduces the number of intranuclear inclusions per 250 μm^2. *=p<.05, **=P<.01, ***=p<.001, scale bars = 50 μm

Fig 17

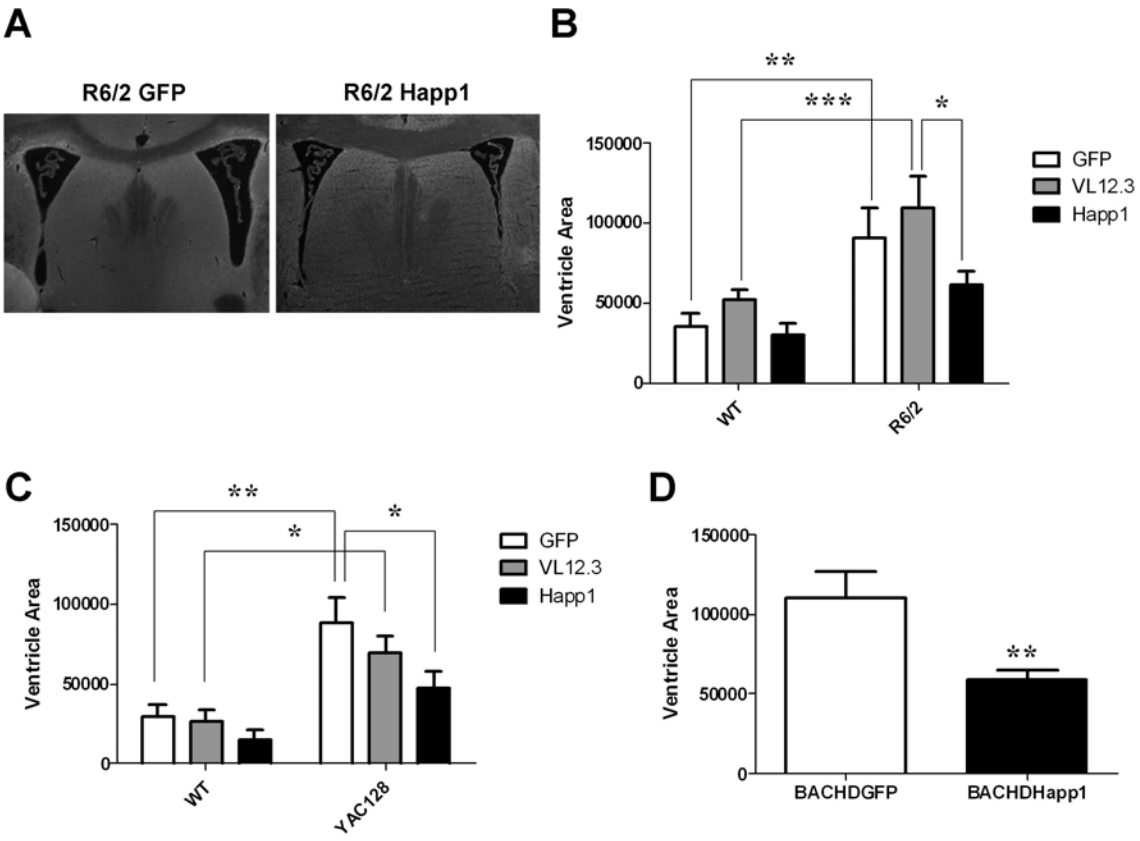

Figure 17. Happ1 treatment reduces ventricular enlargement in three HD mouse models. Ventricle area was measured at approximately bregma in 3 sections each from (A, B) 10 week old male R6/2 and WT littermates, (C) 7 month old male YAC128 and WT littermates, and (D) 6 month old male and female BACHD mice. Both R6/2 and YAC128 mice display increased ventricle size compared to WT littermates. (B) There is a trend toward reduced ventricular

enlargement in response to Happ1 treatment. (C) Happ1 treatment reduces ventricular enlargement in YAC128 mice. (D) Happ1 treatment reduces ventricular enlargement in BACHD mice. *=p<.05, **=p<.01, ***=p<.001

Appendix A

Recombinant Intrabodies as Molecular Tools and Potential Therapeutics for Huntington's Disease

Ali Khoshnan, Amber Southwell, Charles Bugg, Jan Ko and Paul H. Patterson

"New therapeutics in Huntington's disease", eds. RE Hughes and DC Lo. Taylor & Francis group, in press.

The therapeutic potential of intracellularly expressed, recombinant or single-chain fragment variable (scFv) antibodies (intrabodies) is being explored for several diseases including cancer, HIV and neurodegenerative disorders. Intrabodies can bind and inactivate toxic intracellular proteins, prevent misfolding, promote degradation and block aberrant protein-protein interactions with extreme molecular specificity. Neurodegenerative disorders are particularly attractive candidates for these reagents, since many of these diseases involve protein misfolding, oligomerization and aggregation (1). In particular, intrabodies have shown efficacy in blocking the toxicity of the amyloidogenic protein fragment Aβ in cell culture and mouse models of Alzheimer's disease, paving the way for clinical trials of these reagents in brain disorders (2). In addition to their therapeutic potential, intrabodies are also useful molecular tools to identify the pathogenic epitopes in toxic proteins, which can be targets for other types of therapy. In this chapter, we will review the strategies that have been used to develop intrabodies specific for the huntingtin (htt) protein, and describe their testing in models of Huntington's disease (HD) and their development as potential therapeutics for clinical use in HD.

STRATEGIES FOR INTRABODY CONSTRUCTION

Intrabodies are recombinant antibody molecules usually derived from a monoclonal antibody of interest by cDNA cloning of the antigen binding domain; the variable heavy and light chains (V_H and V_L) from the monoclonal antibody are then joined together by a synthetic cDNA encoding a flexible polypeptide linker (Fig. 1A). Alternatively, naïve intrabody libraries have been constructed and cloned in phage or displayed on yeast for selection and binding to specific antigens (Fig 1B).

A major problem with intracellular expression of intrabodies is, however, proper folding and low solubility in the reducing cytoplasmic environment ((Biocca et al., 1995). This is due to the presence of disulfide bonds in both the V_H and V_L, which are required for efficient folding. While some intrabodies are inherently stable in the cytoplasm, selection of stable intrabody frameworks, which fold efficiently in the absence of disulfide bonds, has also been achieved (4). Additionally, a process known as *in vitro* maturation or re-engineering, where the disulfide bonds are removed, can be used to correct low solubility through several rounds of random mutagenesis and antigen binding selection (5).

Single domain intrabodies. Recently, functional single domain (V_H or V_L) intrabodies have also been developed and selected for specific targets. These single domain intrabodies can block protein-protein interaction and are favored for their stability and better folding (6). Moreover, *in vitro* maturation of single domain intrabodies can further enhance their folding, specificity and solubility (5).

DEVELOPMENT OF EPITOPE-SPECIFIC INTRABODIES AGAINST HTT

Epitopes in mutant huntingtin for intrabody development.

Intrabodies recognizing a variety of epitopes within mutant huntingtin (Htt) exon-1 (HDx1) have been isolated and tested for their ability to block toxicity and aggregation (Fig. 2). Lecerf and colleagues have isolated an intrabody recognizing the 17 N-terminal AA of Htt (C4) from a synthetic phage library and tested this intrabody for efficacy in cell culture (7). C4 was found to block aggregation and interfere with malonate-enhanced toxicity of mutant HDx1 (Murphy and Messer, 2004). Due to its modest efficacy, C4 was further matured and examined in a fly model of HD, where it was found to protect against the toxicity of HDx1 during the larval stage and significantly increase life span (Wolfgang et al., 2005).

Surprisingly, C4 increased the level of soluble mutant HDx1 in both fly and culture models (9). This property of C4 raises the possibility that long-term exposure to this intrabody could lead to buildup of soluble HDx1 and promote oligomerization and toxicity. Recent studies suggest that mutant HDx1 monomers can acquire a toxic conformation by switching from an α-helical to a β-sheet conformation (10). Furthermore, blocking the 17 N-terminal AA of Htt may also have other undesirable consequences; for example, this motif is essential for vesicle localization as well as Htt cytoplasmic retention and turnover (11, 12) and removal of the N-terminal domain results in nuclear localization of HDx1, which has been associated with enhanced toxicity (11, 12). Therefore, long-term expression studies in transgenic HD mice will be important to examine if binding

of C4 to the 17 N-terminal AA of Htt has any detrimental effects in a therapeutic setting.

Another intrabody that binds the N1-17 domain of Htt (V_L12.3) was isolated from a yeast surface display library as a single domain light chain and matured *in vitro* through random mutagenesis and selection by yeast surface display (5). V_L12.3, engineered for efficient intracellular expression and folding by removal of its disulfide bond, is a more potent inhibitor of mutant HDx1 aggregation and toxicity in cell culture than C4 (13). However, like C4, V_L12.3 increases the level of soluble mutant HDx1; moreover, V_L12.3 promotes nuclear localization of mutant HDx1 (14). This paradoxical inhibition of toxicity and aggregation together with enhancement of nuclear localization of Htt may eventually shed light on the role of nuclear Htt in toxicity. In fact, intrabodies such as V_L12.3 may have important research and clinical potential in blocking association of soluble mutant HDx1 with nuclear targets. Examination of V_L12.3 in animal models of HD is crucial for validating its protective effects and further understanding of the role of N-17 AA in mutant Htt toxicity.

The polyglutamine and polyproline domains of Htt. Intrabodies recognizing the polyglutamine (polyQ) and proline-rich motifs of HDx1 have also been shown to influence toxicity. We generated a number of monoclonal antibodies using either polyQ peptides or HDx1 recombinant proteins as antigens (15). The intrabodies cloned from these antibodies display striking, epitope-specific differences in their effects on mutant HDx1 toxicity. The MW7 intrabody, which recognizes the polyproline (polyp) motifs of mutant HDx1, protects against

toxicity in several models of HD, including cell culture (Fig. 3), acute brain slice culture, and *Drosophila* models (16, 17, Reinhart et al., unpublished data). This protection is correlated with reduced aggregation and increased turnover of mutant HDx1 (14, 16).

In contrast, intrabodies that bind the expanded polyQ domain exacerbate the toxicity and aggregation of mutant HDx1 in cell culture (16**).** One possible explanation for this effect is that the MW1 and MW2 intrabodies may bind and stabilize a novel confirmation in HDx1 with expanded polyQ. In fact, several anti-polyQ antibodies bind Htt in different cellular compartments, supporting the presence of distinct conformations of expanded polyQ (15). On the other hand, anti-polyQ intrabody binding could aid in nucleation of monomeric mutant HDx1 and accelerate oligomerization**.** In a study of the crystal structure of MW1 bound to polyQ, the polyQ domain adopts an extended, coil-like structure with short sections of polyproline type II helix and β-strand. Consistent with the linear lattice model (18) for polyQ, linking MW1 intrabodies together in a multimeric form results in tighter binding to longer compared to shorter polyQ domains and, compared with monomeric Fv, binds expanded polyQ with higher apparent affinity (19). Whether the affinity of the monomeric vs. multimeric form of MW1 could influence the oligomerization of mutant Htt, remains unknown.

Clearly, a unified view on the role of aggregates in HD pathology will be required to understand better how anti-polyQ intrabodies could be used to regulate mutant htt toxicity. The initial studies of the effects of MW1 and MW2 on HDx1 toxicity and aggregation were done in non-neuronal cells and with 103

polyQ HDx1, which may require a high concentrations of intrabody to counteract its toxicity. Thus, reevaluation of anti-polyQ intrabodies is worthy of investigation, possibly with shorter polyQ repeats or a multimeric form of MW1 (18). Indeed, in light of recent findings that mutant HDx1 aggregation can be neuroprotective, anti-polyQ intrabodies will be ideal tools to dissect the role of aggregation and toxicity in neuronal models (20).

The proline-rich domain of Htt. Finally, we have recently isolated two V_L domain intrabodies from a human scFv phage display library (24) that specifically bind to the proline-rich epitope in HDx1 (which is between the two pure polyP domains discussed above)(14). These single-domain intrabodies (Happ1 and 3, Fig. 1) are efficient in reducing HDx1 toxicity and aggregation. A novel feature of these intrabodies, and of the anti-polyP intrabody MW7, is their reduction of soluble mutant HDx1 levels by increasing its turnover. It is intriguing that although the proline-rich epitope is identical in mutant and wild-type (WT) Htt, the Happ intrabodies have a greater effect on turnover of the mutant versus WT Htt (14). In addition, the inhibitory effects of Happ1 and 3 suggest that the proline-rich domain of Htt also contributes to Htt toxicity and may be involved in the misfolding of mutant HDx1 or in its binding to partners critical for toxicity.

Conformation-specific intrabodies. Isolation of conformation specific polyQ intrabodies may help in determining whether expanded polyQ can be a potential target for intrabody therapy. This approach has recently been reported for α-synuclein oligomers (21). These oligomer-specific intrabodies inhibit both aggregation and toxicity of α-synuclein and have been useful tools for identifying

the pathogenic epitopes. Our laboratory, in collaboration with Ron Wetzel's group, isolated a panel of monoclonal antibodies that specifically recognize oligomeric forms of polyQ proteins. Interestingly, some of these antibodies also react with fibrils formed by prion proteins and Aβ amyloid (22). This cross-reactivity suggests the presence of common structural motifs in the fibrils of misfolded proteins that cause neurodegeneration. A similar antiserum that also reacts with amyloid fibrils of various misfolded proteins has been reported by Glabe's laboratory (23). It will be interesting to see if intrabodies derived from these antibodies can block oligomerization and the toxicity of these diverse proteins *in vivo*.

INTRABODIES AS RESEARCH TOOLS TO DISSECT MECHANISMS OF HTT DISEASE PATHOGENESIS.

While the therapeutic potential of intrabodies in mouse HD models remains to be explored, anti-Htt intrabodies are powerful molecular tools that can be used to identify and characterize the pathogenic epitopes in HDx1 that regulate oligomerization, toxicity, and interactions with other disease mechanisms and pathways. The findings that intrabodies directed against various epitopes of HDx1 can either block or enhance aggregation and toxicity underscore the importance of these domains.

For example, it is known that the first 17 amino acids of HDx1 regulate not only its nuclear targeting but also its endoplasmic reticulum and mitochondrial localization (11, 12). One hypothesis is thus that V_L12.3 reduces toxicity by

blocking the localization of mutant HDx1 to mitochondria and thereby reducing mitochondrial permeability. On the other hand, consistent with the role of the first 17 AA in cytoplasmic retention of HDx1, co-expression of V_L12.3 with HDx1 also promotes HDx1 nuclear localization (14). Thus, as noted above, while studies with V_L12.3 confirm the importance of 17 N-terminal AA in cellular distribution of Htt and the contribution of this motif to aggregation and toxicity (11, 12), they also raise questions regarding whether and how nuclear localization contributes to toxicity. One possibility is that although V_L12.3 promotes nuclear localization of HDx1, it may also prevent its association with the transcriptional apparatus.

Similarly, the ability of anti-polyQ intrabodies to promote aggregation and toxicity of mutant HDx1 (16) may be relevant for understanding the mechanism of *in vivo* oligomerization. One theory is that anti-polyQ intrabodies function as nucleating centers and recruit soluble HDx1, which then forms oligomers and eventually aggregates. Alternatively, binding of anti-polyQ intrabodies may induce or stabilize a conformation in the expanded polyQ domain that enhances oligomerization. If so, this raises the question of whether there are endogenous cellular modifiers that induce such conformation changes in this domain. Understanding how MW1 and 2 promote aggregation may thus shed light on this process *in vivo* and enable discovery of modifiers of polyQ oligomerization. In this context, it is intriguing that intracellular expression of a polyQ binding peptide (PQBP1) blocks the toxicity of mutant HDx1 in tissue culture (25); this peptide interferes with conversion of a non-toxic α-helical structure of polyQ to a toxic β-sheet conformation (10). While this conformation switch occurs *in vitro* with

purified protein, the existence of an endogenous modifier of polyQ toxicity is an attractive area of investigation and intrabodies will help with the identification of these potential regulators of toxicity.

The MW7 intrabody, on the other hand, was instrumental in identifying the HDx1 polyP domain as a pathogenic epitope (16, 26). Several important signaling proteins including NEMO /IKKγ, CBP, WW domain proteins, dynamin and FIP-2 require the HDx1 polyP domain for binding to HDx1 (26-29). Therefore, the protective mechanism of the MW7 intrabody may work through its reducing the sequestration of important cellular proteins by mutant HDx1. In fact, we have shown that MW7 blocks binding of the IκB-kinase (IKK) complex to the proline-rich domain of mutant HDx1 and subsequently reduces HDx1-induced NF-κB activation (26; Fig. 4). Moreover, both MW7 and genetic inhibitors of the IKK complex have similar inhibitory effects on mutant HDx1 in cell and brain slice cultures (26). These findings underscore the importance of intrabodies as molecular tools that can lead to the identification of novel pathogenic epitopes and therapeutic targets.

NOVEL TARGETS FOR INTRABODY THERAPY IN HD

To date, most of the intrabodies developed to perturb Htt function have been targeted to HDx1, which is generated by proteolytic processing of full-length Htt. However, a more upstream, primary therapeutic goal would be to prevent proteolytic processing of mutant Htt using specific intrabodies. Htt is cleaved by several proteases, including caspases 3 and 6, and the calpains (30, 31).

Cleaved mutant Htt fragments are precursors to oligomers, and the species that accumulate in the nucleus likely contribute to transcriptional dysregulation (2). Therefore, blocking the cleavage of full length Htt by intrabodies may be an effective strategy to reduce the generation of fragments that misfold and induce toxicity.

Indeed, such inhibition of Htt cleavage by intrabody binding to cleavage sites may be preferred over small molecule inhibitors of the relevant proteases because of the target specificity of antibody binding, and because small molecule inhibitors can have systemic side effects. This technology has already been applied to reduce production of β-amyloid in AD models. Intracellular expression of an intrabody that binds an epitope in close proximity to the β-secretase cleavage site of amyloid precursor protein (APP) blocks production of amyloidogenic fragments and promotes cleavage with α-secretase, which generates non-amyloidogenic Aβ **(**32). For HD, intrabodies specific to Htt cleavage sites can readily be isolated from phage display libraries and tested in tissue culture for their effects on Htt processing. This approach could be used to validate the role of these caspases on Htt processing and toxicity and, importantly, would generate potential therapeutics for HD.

DELIVERY OF INTRABODIES TO THE HD BRAIN.

In principle, viral vector-based gene therapy is the ideal method for the delivery of therapeutic intrabodies to the brain. Optimal delivery of gene therapy vectors into the diseased brain remains an important research area and

represents the best mode of delivery for long-term expression. Among these, adeno-associated viruses (AAV) are the most promising vectors, since they are largely non-pathogenic and the virus is already widespread and non-toxic in human populations. AAV is capable of infecting both dividing and non-dividing cells and generating long-term expression of transgenes. The existence of several serotypes offers varied tropism allowing expression in a wide range of cell and tissue types. Delivery of AAV vectors also appears to be safe and well tolerated, as no obvious side effects have been reported following a phase 1 clinical trial of AAV mediated delivery of glutamic acid decoarboxylase (GAD) to the brains of human Parkinson's disease patients (33)(2); intracerebral delivery may also avoid systemic complications outside of the CNS.

In animal models of AD, several successful approaches have been reported for delivery of anti-Aβ intrabodies (2, 34). Intracranial delivery of AAV encoding anti-Aβ scFvs, which can be secreted and enter the circulation, has been effective in reducing amyloid plaque loads, neurotoxicity and correcting behavioral abnormalities (2). Viral injections in this model were performed at P0, which allowed widespread distribution and expression. Intrabody delivery to HD models may be more challenging, since the toxic protein remains intracellular, in contrast to Aβ, which is secreted. Nonetheless, success has been obtained with systemic vaccination approaches in mouse models of Parkinson's disease, in which the targeted antigen, □-synuclein, is also thought to be intracellular (35). Moreover, we find that anti-Htt antibodies display specific binding to the surfaces of live cells expressing mutant HDx1, suggesting that systemic and/or

extracellular delivery of intrabodies may also be beneficial in combating Htt toxicity (Fig. 5).

Direct viral delivery to the striatum has also proven to be effective. A single injection of an AAV vector encoding an RNAi targeted against Htt results in extensive spread, reduced HDx1 oligomerization, enhanced DARPP-32 expression in striatal neurons, and amelioration of HD neuropathology (36, 37). Significant neuroprotection by AAV-mediated delivery of the neurotrophins GDNF and BDNF to striatum has also been demonstrated in the quinolinic acid model of HD (38). Thus, direct delivery of intrabody viral vectors to the striatum may be realistic and it is expected that intrabodies will have fewer off-target effects than either RNAi or neurotrophins, due to the high degree of specificity of antibodies. In fact, an intrabody constructed from the EM48 monoclonal antibody, which targets the C-terminus of HDx1, has been tested in an HD mouse model and preliminary data suggest that expression of this intrabody provides significant protection against mutant HDx1 (38). Injection of an adenvovirus expressing EM48 intrabody in the striatum of N-171-82Q HD mice reduces the overall toxicity and decreases the aggregation of mutant Htt in the neuropils. Moreover, expression of EM48 in the striatum improves some of the behavioral deficits of these mice. EM48 however, does not extend the life span of these mice (39). In a lentiviral model of HDx1, intrastriatal injection of adeno-associated virus (AAV) expressing V_L12.3- or Happ1 reduces aggregation of mutant Htt in the adult mice and ameliorates the loss of DARPP-32 expression caused by injection of mHtt-lentivirus. AAV-V_L12.3 and AAV-HAPP1 also improve the amphetamine-induced

rotation bias seen with unilateral mHtt lentivirus injection.

FUTURE DIRECTIONS FOR INTRABODIES IN HD THERAPY

Development of intrabodies for therapeutic purposes and as novel molecular tools to perturb protein function *in vivo* is an exciting emerging field. Some intrabodies have already reached clinical trials and others have been used as novel diagnostic tools (40). As optimization of delivery vehicles progresses, anti-Htt intrabodies will hold great promise for HD therapy in the future. However, many milestones, including the identification of the best targets, the most potent and effective intrabodies, and the most effective methods to ensure a safe, widespread delivery to the CNS must first be achieved. With rapid progress in proteomics, intrabodies can also serve as excellent tools for *in vivo* functional knock-down, for inactivating specific protein domains, and for inhibiting interactions between particular proteins. The HD field can also benefit from intrabody technology for inactivating other intracellular targets that enhance Htt toxicity such as caspases, p53, and IKKs.

REFERENCES

1. Ross CA, Poirier MA (2005) What is the role of protein aggregation in neurodegeneration? *Nat Rev Mol Cell Biol* 6:891-8.

2. Levites Y, Jansen K, Smithson LA, l Dakin R, Holloway VM, Das P, Golde TE (2006) Intracranial adeno-associated virus-mediated delivery of anti-pan amyloid beta, amyloid beta40, and amyloid beta42 single-chain variable fragments attenuates plaque pathology in amyloid precursor protein. *J Neurosci,* 26:11923 -8.

3. Biocca S, Ruberti, F, Tafani, M, Pierandrei-Amaldi, P, Cattaneo A (1995) Redox state of single chain Fv fragments targeted to the endoplasmic reticulum, cytosol and mitochondria. *Biotechnology* 13:1110-5.

4. Tanaka T, Rabbitts TH (2003) Intrabodies based on intracellular capture frameworks that bind the RAS protein with high affinity and impair oncogenic transformation.

EMBO J 22:1025-35.

5. Colby DW, Garg P, Holden T, Chao G, Webster JM, Messer A, Ingram VM, Wittrup KD (2004) Development of a human light chain variable domain (V(L)) intracellular antibody specific for the amino terminus of huntingtin via yeast surface display. *J Mol Biol* 342:901-12.

6. Tanaka T, Lobato MN, Rabbitts TH (2003) Single domain intracellular antibodies: a minimal fragment for direct in vivo selection of antigen-specific intrabodies. *J Mol Biol* 331:1109-20.

7. Lecerf JM, Shirley TL, Zhu Q, Kazantsev A, Amersdorfer P, Housman DE, Messer A, Huston JS (2001) Human single-chain Fv intrabodies counteract in situ

huntingtin aggregation in cellular models of Huntington's disease. *Proc Natl Acad Sci* 98:4764-9.

8. Murphy RC, Messer A (2004) A single-chain Fv intrabody provides functional protection against the effects of mutant protein in an organotypic slice culture model of Huntington's disease. *Molec Brain Res* 121: 141-5.

9. Wolfgang WJ, et al. (2005) Suppression of Huntington's disease pathology in Drosophila by human single-chain Fv antibodies. *Proc Natl Acad Sci* 102: 11563-8.

10. Nagai Y, Inui T, Popiel HA, Fujikake N, Hasegawa K, Urade Y, Goto Y, Naiki H, Toda T (2007) A toxic monomeric conformer of the polyglutamine protein. *Nat Struct Mol Biol* 14:332-40.

11. Rockabrand E, Slepko N, Pantalone A, Nukala VN, Kazantsev A, Marsh JL, Sullivan PG, Steffan JS, Sensi SL, Thompson LM (2007) The first 17 amino acids of Huntingtin modulate its sub-cellular localization, aggregation and effects on calcium homeostasis. *Hum Mol Genet* 16:61-77.

12. Atwal RS, Xia J, Pinchev D, Taylor J, Epand RM, Truant R (2007) Huntingtin has a membrane association signal that can modulate huntingtin aggregation, nuclear entry and toxicity. *Hum Mol Genet* 16:2600-15.

13. Colby DW, et al. (2004) Potent inhibition of huntingtin aggregation and cytotoxicity by a disulfide bond-free single-domain intracellular antibody. *Proc Natl Acad Sci* 101:17616-21.

14. Southwell, AL, Khoshnan A, Patterson PH. Novel intrabodies block aggregation and toxicity of mutant huntingtin by increasing its turnover. Submitted.

15. Ko J, Ou S, Patterson PH (2001) New anti-huntingtin monoclonal antibodies: implications for huntingtin conformation and its binding proteins. *Brain Res Bull.* 56:319-29.

16. Khoshnan A, Ko J, Patterson PH (2002) Effects of intracellular expression of anti-huntingtin antibodies of various specificities on mutant huntingtin aggregation and toxicity. *Proc Natl Acad S*ci 99:1002-7.

17. Jackson GR, Sang TK, Ko J, Khoshnan A, Patterson PH (2004) Inhibition of mutant huntingtin-induced neurodegeneration in vivo by expression of a polyproline-binding single chain antibody. *Soc Neurosci* abstr 938.5.

18. Bennett MJ, Huey-Tubman KE, Herr AB, West AP Jr, Ross SA, Bjorkman PJ (2002) A linear lattice model for polyglutamine in CAG-expansion diseases. *Proc Natl Acad Sci* 99:11634-9.

19. Li P, Huey-Tubman KE, Gao T, Li X, West AP Jr, Bennett MJ, Bjorkman PJ (2007) The structure of a polyQ-anti-polyQ complex reveals binding according to a linear lattice model. *Nat Struct Mol Biol* 14:381-7.

20. Arrasate M, Mitra S, Schweitzer ES, Segal MR, Finkbeiner S (2004) Inclusion body formation reduces levels of mutant huntingtin and the risk of neuronal death. *Nature* 431:805-10.

21. Emadi S, Barkhordarian H, Wang MS, Schulz P, Sierks MR (2007) Isolation of a human single chain antibody fragment against oligomeric alpha-synuclein that inhibits aggregation and prevents alpha-synuclein-induced toxicity. *J Mol Biol* 368:1132-44.

22. Geva M, Wetzel R et al. (2005) Monoclonal antibodies that bind different polyglutamine aggregate conformations. The Protein Society, abstr B165.

23. Kayed R, Head E, Thompson JL, McIntire TM, Milton SC, Cotman CW, Glabe CG (2003) Common structure of soluble amyloid oligomers implies common mechanism of pathogenesis. *Science* 300:486-9.

24. Griffiths AAD, et al. (1994) Isolation of high affinity human antibodies directly from large synthetic repertoires. *EMBO J* 13: 3245-60.

25. Popiel HA, Nagai Y, Fujikake N, Toda T (2007) Protein transduction domain-mediated delivery of QBP1 suppresses polyglutamine-induced neurodegeneration in vivo. *Mol Ther* 15:303-9.

26. Khoshnan A, Ko J, Watkin EE, Paige LA, Reinhart PH, Patterson PH (2004) Activation of the IkappaB kinase complex and nuclear factor-kappaB contributes to mutant huntingtin neurotoxicity. *J Neurosci* 24:7999-8008.

27. Qin ZH, Wang Y, Sapp E, Cuiffo B, Wanker E, Hayden MR, Kegel KB, Aronin N, DiFiglia M (2004) Huntingtin bodies sequester vesicle-associated proteins by a polyproline-dependent interaction. *J Neurosci* 24:269-81.

28. Steffan JS, Bodai L, Pallos J, Poelman M, McCampbell A, Apostol BL, Kazantsev A, Schmidt E, Zhu YZ, Greenwald M, Kurokawa R, Housman DE, Jackson GR, Marsh JL, Thompson LM (2001) Histone deacetylase inhibitors arrest polyglutamine-dependent neurodegeneration in Drosophila. *Nature* 413:739-43.

29. Faber PW, Barnes GT, Srinidhi J, Chen J, Gusella JF, MacDonald ME (1998) Huntingtin interacts with a family of WW domain proteins. *Hum Mol Genet.* 7:1463-74.

30. Gafni J, Hermel E, Young JE, Wellington CL, Hayden MR, Ellerby LM (2004)

Inhibition of calpain cleavage of huntingtin reduces toxicity: accumulation of calpain/caspase fragments in the nucleus. *J Biol Chem* 279:20211-20.

31. Graham RK, Deng Y, Slow EJ, Haigh B, Bissada N, Lu G, Pearson J, Shehadeh J, Bertram L, Murphy Z, Warby SC, Doty CN, Roy S, Wellington CL, Leavitt BR, Raymond LA, Nicholson DW, Hayden MR (2006) Cleavage at the caspase-6 site is required for neuronal dysfunction and degeneration due to mutant huntingtin. *Cell* 125:1179-91.

32. Paganetti P, Calanca V, Galli C, Stefani M, Molinari M (2005) Beta-site specific intrabodies to decrease and prevent generation of Alzheimer's Abeta peptide. *J Cell Biol* 168:863-8.

33. Kaplitt MG, Feigin A, Tang C, Fitzsimons HL, Mattis P, Lawlor PA, Bland RJ, Young D, Strybing K, Eidelberg D, During MJ. Safety and tolerability of gene therapy with an adeno-associated virus (AAV) borne GAD gene for Parkinson's disease: an open label, phase I trial. Lancet. 2007 369:2097-105.

34. Fukuchi K, Tahara K, Kim HD, Maxwell JA, Lewis TL, Accavitti-Loper MA, Kim H, Ponnazhagan S, Lalonde R (2006) Anti-Abeta single-chain antibody delivery via adeno-associated virus for treatment of Alzheimer's disease. *Neurobiol Dis* 23:502-11.

35. Masliah E, Rockenstein E, Adame A, Alford M, Crews L, Hashimoto M, Seubert P, Lee M, Goldstein J, Chilcote T, Games D, Schenk D (2005) Effects of alpha-synuclein immunization in a mouse model of Parkinson's disease. *Neuron* 46:857-68.

36. Harper, SQ, et al. (2005) RNA interference improves motor and neuropathological abnormalities in a Huntington's disease mouse model. *Proc Natl Acad Sci* 102: 5820-5.

37. Machida Y, Okada T, Kurosawa M, Oyama F, Ozawa K, Nukina N (2006) rAAV-mediated shRNA ameliorated neuropathology in Huntington disease model mouse. *Biochem Biophys Res Commun* 343:190-7.

38. Kells AP, Fong DM, Dragunow M, During MJ, Young D, Connor B (2004) AAV-mediated gene delivery of BDNF or GDNF is neuroprotective in a model of Huntington disease. *Mol Ther* 9:682-8.

39. Wang CE, Zhou H, McGuire JR, Cerullo V, Lee B, Li SH, Li XJ (2008) Suppression of neuropil aggregates and neurological symptoms by an intracellular antibody implicates the cytoplasmic toxicity of mutant huntingtin. *J Cell Biol.* 181:803-816.

40. Holliger P, Hudson PJ (2005) Engineered antibody fragments and the rise of single domains. *Nat Biotechnol* 23:1126-36.

Figures

Fig 1

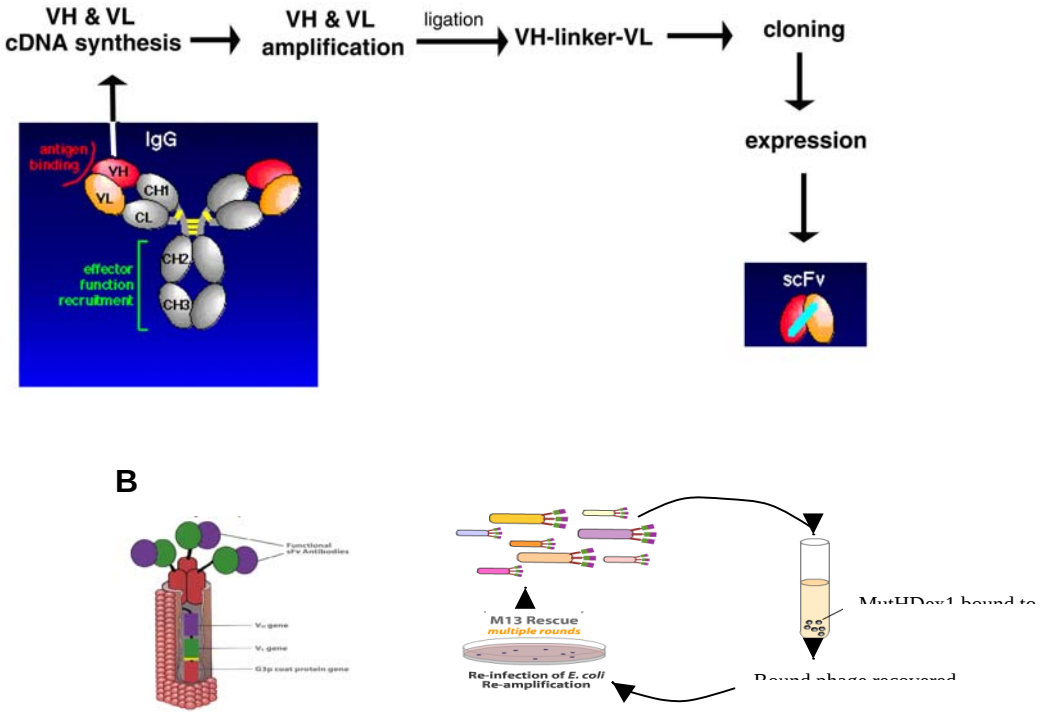

Figure 1. Intrabody construction strategies. (A) Cloning of scFv from monoclonal parental antibodies. (B) selection of intrabodies from phage display library.

Fig 2

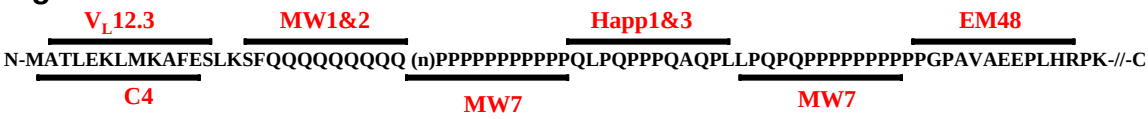

Figure 2. Binding domains of different intrabodies that have been developed against the HDx-1 peptide sequence.

Fig 3

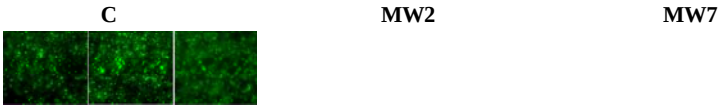

Figure 3. MW7 prevents while MW2 promotes aggregation of mutant HDx1-EGFP in PC12 cells. MW7 and MW2 cDNAs were cloned into ecdysone-inducible vectors and transfected into PC12 cells that were engineered to express HDx1 in response to ecdysone (26). Selected PC12 cell clones were then treated with ecdysone to induce simultaneous expression of HDx1 and the scFv. A luciferase construct was used as control (far left panel).

Fig 4

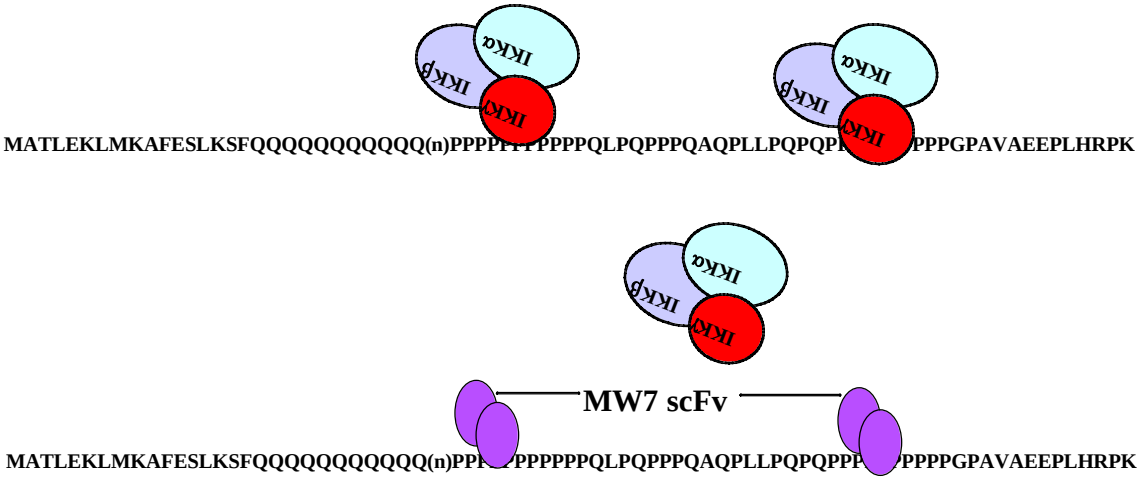

Figure 4 Blocking the interaction of mutant HDx1 with the IKK complex reduces the toxicity in a brain slice culture model of HD. Binding of MW7 intrabodies to the poly-P domains of Htt also prevents IKK–HDx1 interaction and

thereby reduces the toxicity of mutant HDx1. Binding of HDx1 to the IKK complex requires the polyP domain of Htt and the N-terminus of IKKγ.

Fig 5

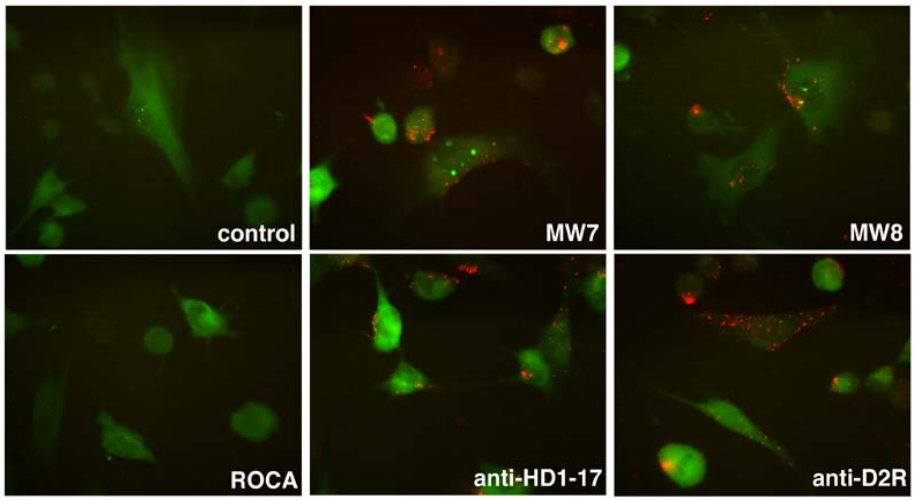

Figure 5. The anti-huntingtin antibodies/intrabodies, anti-N1-17, MW7 and MW8, stain living striatal cells with a punctate pattern (red) similar to an anti-dopamine D2 receptor (D2R) antibody. The striatal ST-14 cell line was transduced with PQ103-EGFP lentivirus and live cells were incubated with either control antibodies (mouse Ig2b, and a non-neuronal anti-CD9 (ROCA)), or anti-Htt antibodies/intrabodies as indicated. A polyclonal antibody against D2R was used as positive control for cell surface staining. Alexa 568-conjugated secondary antibody was used to visualize staining (red); the green fluorescence is native HDx1-EGFP.

Appendix B

GABA transporter deficiency causes tremor, ataxia, nervousness, and increased GABA-induced tonic conductance in cerebellum

Chiu CS, Brickley S, Jensen K, Southwell A, Mckinney S, Cull-Candy S, Mody I, Lester HA. *J Neurosci*. 25:3234-45, 2005.

ABSTRACT

GABA transporter subtype 1 (GAT1) knock-out (KO) mice display normal reproduction and life span but have reduced body weight (female, -10%; male, -20%) and higher body temperature fluctuations in the 0.2-1.5/h frequency range. Mouse GAT1 (mGAT1) KO mice exhibit motor disorders, including gait abnormality, constant 25-32 Hz tremor, which is aggravated by flunitrazepam, reduced rotarod performance, and reduced locomotor activity in the home cage. Open-field tests show delayed exploratory activity, reduced rearing, and reduced visits to the central area, with no change in the total distance traveled. The mGAT1 KO mice display no difference in acoustic startle response but exhibit a deficiency in prepulse inhibition. These open-field and prepulse inhibition results suggest that the mGAT1 KO mice display mild anxiety or nervousness. The compromised GABA uptake in mGAT1 KO mice results in an increased GABA(A) receptor-mediated tonic conductance in both cerebellar granule and Purkinje cells. The reduced rate of GABA clearance from the synaptic cleft is probably responsible for the slower decay of spontaneous IPSCs in cerebellar granule

cells. There is little or no compensatory change in other proteins or structures related to GABA transmission in the mGAT1 KO mice, including GAT1-independent GABA uptake, number of GABAergic interneurons, and GABA(A)-, vesicular GABA transporter-, GAD65-, and GAT3-immunoreactive structures in cerebellum or hippocampus. Therefore, the excessive extracellular GABA present in mGAT1 KO mice results in behaviors that partially phenocopy the clinical side effects of tiagabine, suggesting that these side effects are inherent to a therapeutic strategy that targets the widely expressed GAT1 transporter system.

INTRODUCTION

GABA is the principal inhibitory neurotransmitter in the mammalian brain, where it activates $GABA_A$, $GABA_B$, and $GABA_C$ receptors. GABA released from presynaptic terminals is removed from the vicinity of the synaptic cleft by GABA transporters, and this action is believed to be a key event in terminating synaptic currents. GABA transporters are also involved in maintaining a low extracellular GABA concentration throughout the brain, preventing excessive tonic activation of synaptic and extrasynaptic receptors. GABA transporters may also play a role in replenishing the supply of presynaptic transmitter. Furthermore, GABA transporters may reverse, under both normal and pathological circumstances, to release GABA (Richerson and Wu, 2003, 2004)

Of the three GABA transporters identified in the CNS, GABA transporter subtype 1 (GAT1) is highly expressed in the olfactory bulb, neocortex,

cerebellum, superior colliculus, and substantia nigra, where it is predominantly found in axons, presynaptic terminals, and glial cells. GAT2 is weakly expressed throughout the brain, primarily in arachnoid and ependymal cells. GAT3 expression is densest in the olfactory bulb, midbrain regions, and deep cerebellar nuclei, where it is found predominantly on glial cells (Radian et al., 1990; Ikegaki et al., 1994; Itouji et al., 1996; Yan et al., 1997; Engel and Wu, 1998; Barakat and Bordey, 2002; Chiu et al., 2002).

The GAT1 inhibitor tiagabine is a clinically useful antiepileptic drug with few cognitive side effects (Aldenkamp et al., 2003),but it also causes tremor (its major side effect), ataxia, dizziness, asthenia, somnolence (sedation), and nonspecific nervousness (Adkins and Noble, 1998; Pellock, 2001; Schachter, 2001). It is important to know whether these side effects arise directly from increased extracellular concentration of GABA in the CNS or, instead, from actions on unintended targets. For instance, GAT1 inhibitors may also inhibit $GABA_A$ receptors (Overstreet et al., 2000; Jensen et al., 2003). If the latter mechanism holds, then a more selective GAT1 inhibitor could be a more effective antiepileptic.

To address this question, we examined the phenotype of the ultimate GAT1-specific inhibitor: genetic interruption of GAT1 function. The homozygous and heterozygous mouse GAT1 (mGAT1) knock-out (KO) strain is viable and fertile, with a normal life span. Its hippocampal electrophysiology has been studied previously (Jensen et al., 2003), but this is the first report of several other phenotypes, including motor behavior, general mood, cerebellar

electrophysiology, and thermoregulation. We emphasize measurements on the cerebellum, where GAT1 is heavily expressed and has been quantified (Chiu et al., 2002).

GABA influences circadian rhythm (Liu and Reppert, 2000). Because tiagabine-treated patients show dizziness, asthenia, and somnolence, we determined whether the GAT1 KO mice display altered activity in their habituated home cage. We also monitored body temperature rhythm, which is synchronized with daily activity (Weinert and Waterhouse, 1999). We found that the mGAT1 KO mouse does phenocopy some effects of tiagabine, which, in turn, suggests that the various clinical side effects of this drug result, directly or indirectly, from its blockade of GAT1. We measure altered synaptic physiology, deriving from increased and prolonged extracellular [GABA], which provides a plausible physiological basis for these effects.

MATERIALS AND METHODS

GAT1 knock-out strain. The mGAT1 KO strain, previously termed "intron-14-neo-mGAT1," carries an intact neomycin selection marker in intron 14. The details of the targeting construct, homologous recombination, and genotyping were described previously (Chiu et al., 2002).

Synaptosomal GABA uptake assay. Details of synaptosomal preparation and GABA uptake assay were described previously (Chiu et al., 2002). Briefly, mice were anesthetized with halothane (2-bromo-2-chloro-1,1,1-trifluorothane), and brains were dissected and collected on ice. The cerebellum (~50 mg) was

homogenized in 20x (w/v) medium I (0.32 M sucrose, 0.1 mM EDTA, and 5 mM HEPES, pH 7.5; 1 ml) (Nagy and Delgado-Escueta, 1984). The P2 fraction (synaptosome fraction) was suspended with 1 ml of medium I. Protein concentrations were analyzed by using the Coomassie Plus kit (Pierce, Rockford, IL).

GABA uptake assays were performed by mixing 20 µl of the suspension with 280 µl of uptake buffer (in mM: 128 NaCl, 2.4 KCl, 3.2 $CaCl_2$, 1.2 $MgSO_4$, 1.2 KH_2PO_4, 10 glucose, 25 HEPES, pH 7.5) and then incubated at 37°C for 10 min (Lu et al., 19980). GABA and [^{3}H]GABA in various concentrations (100 µl) were added to the synaptosome suspension and incubated for 10 min (final radioactive concentrations were 2.2-8.8 µCi/ml). Uptake was terminated by placing the samples in an ice-cold bath, followed by two washes with uptake buffer containing the same concentration of cold GABA at 10,000 x *g*. The GABA uptake inhibitor 1-[2-[[(diphenylmethylene)imino]oxy]ethyl]-1,2,5,6-tetrahydro-3-pyridinecarboxylic acid hydrochloride (NO711) (final concentration, 30 µM) was included to measure the non-GAT1 uptake activity; the NO711-sensitive fraction accounted for 75-85% of wild-type (WT) activity.

Tremor measurements. The mouse was placed in a 2 L polyethylene freezer container. A piezoelectric transducer (LDT0 - 028K; Measurement Specialties, Fairfield, NJ) was taped to the bottom of a 7.5 x 10 cm plastic board (8 g), and this board was loosely attached to the bottom of the container with a loop of paper tape. The mice were placed directly on the board. The signal from the sensor was low-pass filtered at 200 Hz, amplified by 100 (model 902;

Frequency Devices, Haverhill, MA), and led to the analog-to-digital inputs on an Axon DigiData 1200 interface (Axon Instruments, Union City, CA). The signals were collected using Clampex Gap-Free recording, and power spectra were computed in ClampFit. We verified that the resonant frequency of this instrument was far from the tremor frequency by replacing the mouse with 20 g of mass, and the response of the instrument to constant-frequency mechanical stimulation varied, with frequency, by <40% between 20 and 32 Hz.

Benzodiazepine modulation of the tremor. Mice were tested for baseline tremor as described previously. They were then injected intraperitoneally with either flunitrazepam in 20% FreAmine HBC (B Braun Medical, Bethlehem, PA) or vehicle. After 15 min, the tremor was measured.

Footprint. Hindpaws were painted with black India ink, and mice were placed in a cardboard box (90 x 12 x 12 cm) with a 75-cm-long white paper floor. Paw angle is the hindpaw central axis relative to its walking direction.

Rotarod. Mice were tested on a motorized rotarod (Ugo Basile, Comerio, Italy) consisting of a grooved metal roller (3 cm in diameter) and separated 11-cm-wide compartments elevated 16 cm. The acceleration rate was set at 0.15 rpm/s. Mice were placed on the roller, and the time they remained on it during rotation was measured. The rotarod has an increment of 4 rpm/step. Tests were performed for fixed speed at either 12 or 20 rpm and for accelerating speed. A maximum of 120 s was allowed per animal for fixed speed tests.

Exploratory locomotor activity. An individual mouse was placed in a novel environment of a square open field (50 x 50 cm), the floor of which was divided

into 25 smaller squares (5 x 5) by painted lines. Within 10 cm of the chamber walls is termed the periphery (16 squares), and the central region indicates the central nine squares. The animal behavior in the open field was recorded by videotaping for 10 min and analyzed subsequently. The measurements include delayed exploratory activity (measuring the time required for mice to walk the first 50 cm), frequency of visits to the central area, dwell time in the inner field, number of rearing events, total distance traveled, and walking speed. Mice usually made short walks interrupted by brief stops. To make meaningful walking-speed measurements, we chose uninterrupted walking for >25 cm and averaged 3-12 such walking-speed measurements for each animal. All animals were tested in a particular behavioral assay on the same day during the light part of the light/dark cycle.

Elevated plus maze. Mice were allowed to habituate to the testing room for 2 h. The maze consisted of two opposing open arms (40 x 10 cm) and two opposing closed arms (40 x 10 cm, with 40 cm walls) on a platform 50 cm above the ground. Mice were placed in the center square (10 x 10 cm) facing an open arm and videotaped during a 5 min exploration. Arm entries and duration were scored when all four paws entered the arm. Partial arm entries were scored when one to three paws entered the arm. Head dipping was scored when the head was dipped over the edge of the maze. All animals were tested on the same day during the light part of the light/dark cycle.

Home-cage activity. Mice were housed individually in cages with bedding, food, and water. To assess activity, beam breaks were collected for 42 h with a photo

beam system (San Diego Instruments, San Diego, CA). Plots show the number of beam breaks for each 5 min interval.

Benzodiazepine hyperlocomotor activity. Mice were allowed to habituate to activity cages for 2 h. They were then injected intraperitoneally with either flunitrazepam in 20% FreAmine HBC (5 or 15 mg/kg) or vehicle. Activity (single beam breaks) and ambulation (successive beam breaks) data were then collected for 1 h and plotted for each 5 min interval.

Acoustic startle and prepulse inhibition. Animals were tested in a Startle Response system (SR-LAB; San Diego Instruments) consisting of a 5 cm Plexiglas cylinder mounted on a Plexiglas platform in a ventilated, lighted, sound-attenuated chamber. Acoustic stimuli were presented by a high-frequency loudspeaker mounted 28 cm above the cylinder. A piezoelectric accelerometer attached to the Plexiglas base was used to detect movement of the animals within the cylinder. Animal movement was scored in arbitrary numbers between 0 and 1000. Ambient background noise of 68 dB was maintained throughout each testing session. Each session was initiated with a 5 min acclimation period followed by six 120 dB trials and concluded with another six 120 dB trials. These first and last sets of six 120 dB pulses were not included in the analysis. For acoustic startle-response (ASR) testing, seven different levels of acoustic startle pulse (73, 78, 83, 85, 100, 110, and 120 dB) were presented along with a trial containing only the background noise for 40 ms each in random order with variable intertrial intervals of 10-20 s. At the onset of stimulus, 65 startle-amplitude readings were taken for 1 ms each. Ten trials of each decibel level

were performed, and the average startle amplitude was determined. The session used for prepulse inhibition (PPI) testing consisted of five different trials presented 10 times each in random order. These include 120 dB startle pulse alone, 120 dB startle pulse preceded by a prepulse of 73, 78, or 83 dB (5, 10, and 15 dB above background), and a trial containing only the background noise. The percentage of prepulse inhibition was calculated as follows: 100 x [(average 120 dB startle pulse - average prepulse + 120 dB startle pulse)/average 120 dB startle pulse].

Temperature measurements. Mini Mitter (Sunriver, OR) ER-4000 telemetric temperature probes were used in 3- to 6-month-old male mGAT1 KO mice. For implantation, mice were anesthetized with halothane, and a 1 cm incision was made at the back of the neck. Probes were inserted subcutaneously into the back. The incision was sealed with surgical glue. The mice were housed with *ad libitum* water and food at 24 ± 2.5°C. Lights were on between 6:00 A.M. and 6:00 P.M. for 7-10 d after implantations and then off for the period of data collection. Temperature and activity data were acquired using Vital View software (Mini-Mitter) and analyzed (including fast Fourier transforms) in Origin.

Seizure tests. Pentylenetetrazole (PTZ) was solubilized in 0.9% NaCl saline solution, and bicuculline was dissolved in 0.1N HCl, pH adjusted to 5.5 with 0.1N NaOH (Pericic and Bujas, 1997). Animals were injected intraperitoneally with either PTZ or bicuculline. For PTZ, animals were injected with either subthreshold (40 mg/kg) or suprathreshold (70 mg/kg) doses. For bicuculline, animals were injected with 3, 4, or 5 mg/kg.

Brain slice electrophysiology. Cerebellar slices were prepared using standard procedures (Brickley et al., 1996). The brain was rapidly dissected and submerged in cold slicing solution (≈4°C), which contained the following (in mM): 125 NaCl, 2.5 KCl, 1 $CaCl_2$, 4 $MgCl_2$, 25 $NaHCO_3$, 1.25 NaH_2PO_4, and 25 glucose. All extracellular solutions were bubbled with 95% O_2 and 5% CO_2, pH 7.4. After cutting on a moving-blade microtome, slices were maintained at 32°C for 60 min before transfer to a recording chamber. For granule cell recordings, slices were constantly perfused (1.5 ml/min) with recording solution containing the following (in mM): 125 NaCl, 2.5 KCl, 2 $CaCl_2$, 1 $MgCl_2$, 26 $NaHCO_3$, 1.25 NaH_2PO_4, and 25 glucose. For Purkinje cell recordings, slices were perfused with the following (in mM): 126 NaCl, 2.5 KCl, 2 $CaCl_2$, 2 $MgCl_2$, 26 $NaHCO_3$, 1.25 NaH_2PO_4, 10 glucose, 0.2 L-ascorbic acid, 1 pyruvic acid, and 3 kynurenic acid. All experiments were performed at room temperature, and whole-cell voltage-clamp recordings were made using Axopatch 1D or 200B amplifiers (Axon Instruments). The pipette solution contained the following (in mM): 140 CsCl, 4 NaCl, 0.5 $CaCl_2$, 10 HEPES, 5 EGTA, 2 Mg-ATP, adjusted to pH 7.3 with CsOH. Currents were filtered at 2-3 kHz and digitized at 10 kHz. The tonic $GABA_A$ receptor-mediated conductance (G_{GABA}) was measured from the reduction in holding current recorded in the presence of the $GABA_A$ receptorantagonist2-(3-carboxypropyl)-3-amino-6-(4-methoxyphenyl)-pyridazinium bromide (SR95531) (>100 μM). All-points histograms were constructed from sections of data not containing synaptic currents and mean values calculated from a Gaussian fit to the histogram. Spontaneous IPSCs (sIPSCs) were detected with amplitude- and

kinetics-based criteria (events were accepted when they exceeded a threshold of 6-8 pA for 0.5 ms) using custom-written LabView-5.1-based software (National Instruments, Austin, TX). All IPSCs were also inspected visually, and sweeps were rejected or accepted manually. Individual spontaneously occurring IPSCs were then aligned on their initial rising phase, and average IPSC waveforms were constructed from those events that exhibited a clear monotonic rise and returned to baseline before the occurrence of later sIPSCs. The decay of average sIPSC waveforms was quantified as a weighted τvalue calculated from the charge transfer of normalized averages ($\tau_{integral}$).

Immunocytochemistry. Detailed procedures for immunocytochemistry were described previously (Chiu et al., 2002; Jensen et al., 2003). Mice were anesthetized with halothane and perfused with 4% paraformaldehyde in PBS, pH adjusted to 7.6 with Na_2HPO_4. Brains were dissected and kept in 4% paraformaldehyde for 1 h in 4°C and then incubated in 30% sucrose in PBS for ~ 20 h. The brains were embedded in OCT medium (Tissue-Tek; Miles, Elkhart, IN) for either horizontal or sagittal sections and sliced by cryostat at 35 μm. Brain slices were stored in a solution containing the following (in mM): 11 NaH_2PO_4, 20 Na_2HPO_4, 30% ethylene glycol, and 30% glycerol, pH 7.5, at -20°C. Sections were incubated for 2 h at room temperature in a blocking solution (10% normal goat serum and 0.3% Triton X-100 in PBS, pH 7.6), followed by incubation with the primary antibody for 2 d at 4°C with rotational mixing. Primary antibodies and their dilutions were rabbit anti-GAT3 (1:200 dilution; Chemicon, Temecula, CA), rabbit anti-$GABA_A$ receptor α1 (1:100; Upstate Biotechnology,

Lake Placid, NY), rabbit anti-glutamate decarboxylase 65 (GAD65) (1:1000; Chemicon), and rabbit anti-vesicular GABA transporter (vGAT) (1:100; Synaptic Systems, Goettingen, Germany). The brain slices were first washed with PBS containing 0.5% Triton X-100 followed by two additional washes with PBS. The slices were then incubated in solutions containing the appropriate rhodamine red-x-conjugated secondary antibodies. These secondary antibodies include goat anti-rabbit, goat anti-guinea pig, or donkey anti-goat secondary antibodies (1:200; Jackson ImmunoResearch, West Grove, PA). After three washes with PBS, slices were rinsed with PBS, mounted with Vectashield (Vector Laboratories, Burlingame, CA), and subjected to confocal microscope imaging.

RESULTS

Evidence for functional knock-out of GAT1. The knock-in mouse strain studied here, previously termed intron-14-neo-intact-mGAT1, harbors a neomycin resistance cassette (*neo*) in intron 14 as well as a green fluorescent protein (GFP) moiety fused to the C terminus of the mGAT1 coding region in exon 14 (Jensen et al., 2003). This strain was originally constructed as a genetic intermediate in the eventual construction of a *neo*-deleted mGAT1-GFP knock-in strain that has also been described previously (Chiu et al., 2002). However, we found that the present strain appears to have essentially no functional mGAT1 (Jensen et al., 2003), presumably because the *neo* sequences interfere with mRNA or protein. Figure 1 shows additional evidence on this point in the cerebellum, for which we later provide electrophysiological data. First, the GFP

moiety at the C terminus of the GAT1 construct provides a fluorescent label for the level of GAT1 expression (Chiu et al., 2002). The mGAT1 KO strain shows <2% as much fluorescence as the mGAT1-GFP strain (Chiu et al., 2002) and no more fluorescence than WT mice (Fig. 1*A-C*). Second, to measure mGAT1 function, we performed GABA uptake assays on cerebellar synaptosomes. The NO711-sensitive GABA uptake activity from mutant mice synaptosomes was <2% of that of WT littermates, whereas heterozygotes displayed intermediate GABA uptake activity (Fig. 1*E*), indicating that mutant mice have little or no functional presynaptic GAT1 activity. mGAT1-deficient mice also display reduced body weight, ~20 and ~10% less than WT for males and females, respectively (Fig. 1*F*).

Cerebellar immunocytochemistry. To test whether the mGAT1 KO mouse has abnormalities in the GABAergic system, we performed immunocytochemistry on several proteins related to GABA function. Immunocytochemistry using antibodies against GAD65, the $GABA_A$ α1 subunit and the vGAT indicated that mGAT1 KO mice do not change GABAergic synapse densities and related receptor expression in the molecular layer of the cerebellum (summarized in Fig. 1*D*) (based on images in the supplemental figure, available at www.jneurosci.org as supplemental material). We also found no qualitative differences in $GABA_A$ α1 subunit staining in the granule cell layer (data not shown). These data agree with previous data on the hippocampus (Jensen et al., 2003). Also, the expression pattern for GAT3 is not changed, suggesting that no compensatory changes occurred because of the GAT1 deficit (see supplemental

figure, available at www.jneurosci.org as supplemental material). Immunocytochemistry using antibodies against GABAergic, interneuron-specific, calcium-binding proteins showed no changes in GABAergic interneuron density in the hippocampus and in the cerebellum.

Behavioral characterizations of GAT1 KO mice

Tremor. The mGAT1 KO mice display readily observable, nearly continuous tremor in the limbs and tail. Measured by a simple instrument (Fig. 2*A*) (see Materials and Methods), the tremor frequency is 25-32 Hz (Fig. 2*B*). In addition, KO and WT share an additional lower amplitude tremor at ~80 Hz (Fig. 2*B*) (n = 6). Vibrations in both frequency ranges are highest during rearing episodes (Fig. 2*A*, arrows). Acute high-dose NO711 treatment caused complete sedation in WT mice, vitiating any observations on tremor in NO711-treated WT mice. Flunitrazepam treatment decreased the frequency and increased the amplitude of the tremor in mGAT1 KO mice (Fig. 2*C*) but had very little effect on the power spectrum of WT mice (data not shown). These effects in KO mice were both significant for 15 mg/kg flunitrazepam; both effects were intermediate for 10 mg/kg flunitrazepam, but only the frequency change was significant for 10 mg/kg flunitrazepam.

Ataxia. Ataxia is associated with cerebellar defects in many strains of mice (Mullen et al., 1976; Watanabe et al., 1998; Rico et al., 2002). The mGAT1 KO mice walk with an abnormally large paw angle relative to the direction of walking: 23 ± 0.7 versus 12.5 ± 1.4° for KO and WT, respectively (Fig. 3*E, F*). In another indication of ataxia, mGAT1 KO mice display flattened stance and lowered hip on

the rotarod (Fig. 3*B*). The mGAT1 KO mice show reduced time on the rotarod in both fixed speed (Fig. 3*C*) and accelerating speed (Fig. 3*D*) tests, indicating ataxia. Both WT and mutant mice improved performance on the rotarod after training; however, the difference of latency to fall remained significant between WT and KO mice (data not shown). The mGAT1 KO and WT mice displayed equal muscle strength in hanging-wire activity tests (data not shown).

Mild anxiety: flexor contraction, exploratory activity, elevated plus maze, and startle. When suspended by the tail, the mGAT1-deficient mice display trembling and flexor contraction (front paws held together and rear paws flexed) (Fig. 3*A*). This gesture resembles typical mouse models for anxiety. WT littermates displayed normal extension without trembling (Fig. 3*A*). The flexor contraction was also observed in WT mice treated with a high dose of NO711 (10-40 mg/kg; data not shown).

The open field was used as an additional test of anxiety-like behavior (Fig. 4) (Prut and Belzung, 2003). Because an open field is a novel environment, rodents tend to prefer the periphery of the apparatus, later exploring the central parts of the open field. We observed several aspects of behavior in this apparatus. The mGAT1 KO mice tend to remain longer in the corner of the open field (Fig. 4*A*) and then tend to walk slowly along the wall; thus, there was markedly reduced frequency of visits to the central area (Fig. 4*B*), reduced dwell time in the central area (Fig. 4*C*), and reduced rearing activity (Fig. 4*D*). These results may signify anxiety of the mGAT1 KO mice. There was modestly reduced walking speed (Fig. 4*E*). Although WT and heterozygotes walk faster than KO

mice, they spend more time in rearing; as a consequence, all three genotypes traveled about the same distance (Fig. 4*F*). Several of the observations in the open-field test suggest that the heterozygote is the least anxious phenotype; we did not explore this observation systemically.

We observed the mGAT1 KO mice in the elevated plus maze, another test of anxiety (Fig. 5*A, B*). The mGAT1 KO mice displayed increased partial arm entries (Fig. 5*A*) and time spent in the central square (Fig. 5*B*) compared with WT mice. Homozygous mutant mice showed reduced open-arm entries and reduced total time spent in the open arms (data not shown). There was a trend toward reduced closed-arm entries; however, this difference was not statistically significant compared with WT. Mutant mice spent the majority of the testing time in the central square engaging in partial-arm entries, indicating no reduction in locomotor activity. No difference was seen in head dipping. Thus, the elevated plus maze provided some additional evidence for anxiety.

Startle is a fast twitch of facial and body muscles evoked by sudden and intense tactile, visual, or acoustic stimulations. Many anxious mouse strains display both enhanced ASR and reduced PPI. The mGAT1-deficient mice display normal ASR (Fig. 5*C*) but reduced PPI (Fig. 5*D*), compared with their WT littermates. The baseline movement of the mGAT1 mutant in the absence of acoustic stimulation was elevated above the WT. This most likely reflects the constant tremor of these mice.

Ambulation activity. The mGAT1 KO mice show reduced ambulation in their cages; as a consequence, the 24 h activity cycle becomes less obvious (Fig.

6*A*). The total ambulation activities were 2425 ± 395 versus 965 ± 146 times during 42 h for WT and mGAT1 KO mice, respectively (Fig. 6*B*) (mean ± SEM). Flunitrazepam treatment caused hyperlocomotor activity in KO animals and sedation in WT animals (data not shown).

Autonomic regulation: body temperature fluctuations. The mGAT1 KO mice display a striking pattern of abnormal temperature regulation (Fig. 7*A,B*). There is a normal circadian temperature rhythm, but in addition, there are many fluctuations, primarily hyperthermic episodes on a time scale of several minutes to ~2 h. To quantify these fluctuations, we computed and averaged the power spectral density of temperature fluctuations in WT or KO mice (Fig. 7*C*). The data have been normalized to the peak at 0.0416 h^{-1} (corresponding to the circadian rhythm). It is clear that mGAT1 KO mice display increased relative noise power in the frequency range from 0.2 to 1.5 h^{-1}. The mGAT1 hyperthermic episodes are larger, especially during high activity (i.e., higher body temperature), but no more frequent than in WT mice (Fig. 7*B*). Two additional animals in each group provided similar data, but these animals were not included in the averaged power spectra because of differences in sample rate.

Sensitivity to convulsants. The mGAT1 KO mouse is slightly more sensitive than the WT mouse to PTZ-induced seizures, but there is no obvious change in bicuculline-induced seizure susceptibility. Bicuculline (i.p.) at 5 mg/kg kills WT and mGAT1 KO mice, whereas at 3 and 4 mg/kg, both WT and KO mice survived with moderate seizure (n = 2 each). PTZ at a subthreshold dose (40 mg/kg, i.p.) decreased observable activity in WT and heterozygotes while causing

preconvulsive states and mild seizures in mGAT1 KO mice (*n* = 3 each). At a suprathreshold dose (70 mg/kg), all WT and heterozygotes survived with severe seizures, whereas mGAT1 KO mice showed severe seizures, and one of three died (*n* = 3 each).

Cerebellar slice electrophysiology. $GABA_A$ receptor-mediated currents, recorded from wild-type mice, are similar to those reported previously (Brickley et al., 2001) (Fig. 8). Granule cells dialyzed with high-internal Cl^- and voltage clamped at -70 mV (see Materials and Methods) exhibit sIPSCs, with a frequency of 0.8 ± 0.6 Hz (*n* = 4). In addition, a tonic $GABA_A$ receptor-mediated conductance (G_{GABA}) is clearly present in all recordings. The phasic and tonic conductances are both blocked by the $GABA_A$ receptor antagonist SR95531 (>100 μM) (Fig. 8*A*). The magnitude of G_{GABA} (84.2 ± 50.4 pS/pF) is similar to previous reports for animals of this age, as are the peak amplitude (388.5 ± 143.3 pS/pF) and kinetics ($\tau_{integral}$ = 17.6 ± 3.3 ms) of average sIPSCs (Brickley et al., 2001).

Recordings from mGAT1 KO cerebellar granule cells reveal marked differences in both the tonic and phasic conductances, consistent with the removal of a GABA transporter. In all seven recordings from mGAT1 KO mice, G_{GABA} is significantly increased (Fig. 8*B*) to an average value of 318.9 ± 65.6 pS/pF ($p < 0.05$) (Fig. 8*C*). Conventional sIPSCs (Fig. 8*D,E*) are still detectable within the current record, albeit at an apparently lower average frequency (0.4 ± 0.2 Hz). The increased current variance associated with G_{GABA} (Fig. 8*E*, histogram) made resolution of small sIPSCs more difficult. Nevertheless, it

appears that the average peak amplitude is not significantly different in the mGAT1 KO recordings (270.5 ± 31.5 pS/pF). However, as shown in Figure 8*F*, the decay of sIPSCs is slower in the mGAT1 KO cells ($\tau_{integral}$ = 36.9 ± 5.7 ms compared with 17.6 ± 3.3 ms in wild-type granule cells). Therefore, in mature cerebellar granule cells, we observed an ~300% increase in the magnitude of G_{GABA} and a 100% increase in the decay time of sIPSCs after the removal of GAT1.

In Purkinje cell recordings, a standing inward $GABA_A$ receptor-mediated conductance, defined by sensitivity to the $GABA_A$ receptor antagonist SR95531 (>100 μM), was observed in mGAT1 KO mice, which is much larger than in WT mice (75 ± 19 pS/pF, *n* = 10 vs 13 ± 5 pS/pF, *n* = 9, respectively) (Fig. 9). However, the high frequency of sIPSCs consistently observed in Purkinje cells (>10 Hz) indicates that a comparison of sIPSC kinetics between WT and mGAT KO mice is not possible in this cell type because of the considerable superimposition of events. Moreover, it is not feasible to selectively analyze the tonic and phasic components of the $GABA_A$-mediated conductance in a similar manner to the granule cell recordings. Nonetheless, as shown in Figure 9, it is clear that in Purkinje cell recordings, the magnitude of a standing inward $GABA_A$ receptor-mediated conductance is significantly increased in mGAT1 KO mice.

DISCUSSION

The mGAT1 KO mouse as a model for tiagabine side effects. The distinct phenotype of mGAT1 KO mice includes ataxia, tremor, sedation,

nervousness (mild anxiety), increased frequency and amplitude of body temperature fluctuations, and reduced body weight. Similar behavioral patterns were also observed in WT mice treated with either tiagabine or NO711, both GAT1 inhibitors (Nielsen et al., 1991; Suzdak et al., 1992; Suzdak, 1994). Epileptic patients treated with Tiagabine display similar side effects, including dizziness, asthenia, somnolence (sedation), nonspecific nervousness, tremor, and ataxia (Adkins and Noble, 1998). The fact that the mGAT1 KO mice phenocopy many effects of both mice and humans treated with GAT1 inhibitors suggests that the clinical side effects might be expected from any systemically administered drug that targets GAT1, no matter how selective.

Synaptic basis of the tremor. GAT1 inhibition causes elevated extracellular [GABA] and therefore generates an increased tonic $GABA_A$-mediated conductance, perhaps primarily by acting at areas that typically express high-affinity, nondesensitizing $GABA_A$ receptors (Brickley et al., 1996; Wall and Usowicz, 1997; Hamann et al., 2002; Jensen et al., 2003). Our data for cerebellar granule (Fig. 8) and Purkinje (Fig. 9) cells support these ideas. Previous studies also report a prolongation of the evoked $GABA_A$ receptor-mediated synaptic decay after block of GABA transporters (Dingledine and Korn, 1985; Roepstorff and Lambert, 1992, 1994; Thompson and Gahwiler, 1992; Draguhn and Heinemann, 1996; Rossi and Hamann, 1998; Overstreet et al., 2000). This phenomenon is not observed after action potential-independent release (Thompson and Gahwiler, 1992; Isaacson et al., 1993), suggesting that GAT1 transporters are likely to be more important in limiting the GABA profile after

multivesicular release. However, the use of GABA transport blockers in previous assays may be complicated by the fact that GAT1 inhibitors are also competitive antagonists of $GABA_A$ receptors (Overstreet et al., 2000; Jensen et al., 2003).

The cerebellar glomerulus, like the basket cell-Purkinje cell pinceau synapse and the chandelier cell-pyramidal cell cartridge of cortex, is a highly organized synaptic structure that contains many synaptic contacts produced by just a few presynaptic inhibitory axons (Jakab and Hamori, 1988) and features a dense level of GAT1 expression (Chiu et al., 2002). The dramatically prolonged granule cell IPSC waveforms in mGAT1 KO mice are certainly consistent with the idea that GAT1 plays a more important role in clearing GABA after multivesicular release in structures such as the glomerulus, where diffusion is limited (Nielsen et al., 2004). This may explain the greater prolongation of sIPSCs we observe in mGAT1 KO granule cells (Fig. 8) than previously observed in hippocampus (Jensen et al., 2003). The unchanged level of GAD65 (Fig. 1*D*), vGAT (Fig. 1*D*), the GABA receptor α1 subunit (Fig. 1*D*), $GABA_B$ receptors (Jensen et al., 2003), and GAT3 (see supplemental figure, available at www.jneurosci.org as supplemental material) in the mGAT1 KO mice argues against some classes of compensatory changes in response to the chronically elevated [GABA]. Furthermore, the NO711-insensitive cerebellar synaptosomal GABA uptake was only 15-25% of the total activity in WT, and the absolute value of NO711-insensitive GABA uptake activity showed no difference between WT and mGAT1 KO. However, we cannot rule out other changes such as altered subunit composition of $GABA_A$ receptors or an altered waveform of synaptically released

[GABA]. Whatever the underlying synaptic mechanisms, the distorted inhibitory waveform observed in granule cells suggests that inhibition in one or more motor control nuclei provides a reasonable, although not quantitative, explanation for the tremor that we observed in the mGAT1 KO mouse. An oscillation between excitation and inhibition underlies many neuronal pacemakers, and in mGAT KO mice, this oscillation is apparently timed in part by the accentuated inhibitory phase that results from increased and prolonged [GABA]. Flunitrazepam, an allosteric activator of $GABA_A$ receptors, increased the period and increased the amplitude of the tremor (Fig. 2*C*), consistent with the idea that one phase of the oscillation is governed by the waveform of $GABA_A$-mediated inhibition.

Which inhibitory synapse(s) dominates the tremor? We do not imply that the oscillation is solely determined by the timing of a cerebellar inhibitory synapse such as the Golgi cell-granule cell contact. The removal of GAT1 presumably alters characteristics of GABA-mediated transmission in many nuclei. $GABA_A$ receptor α1 subunit knock-out mice tremble at ~18 Hz (Kralic et al., 2002), suggesting that a tremor can arise from either too little or too much GABAergic transmission throughout the brain. However, the tremor in mGAT1 KO mice is inconsistent with the low-frequency tremors generally associated with basal ganglia and midbrain pathology. The tremor also has a higher frequency (25-32 Hz) (Fig. 2) than most previously reported mouse tremors but equal to that of mice expressing the hypofunctional glycine receptor (GlyR) *oscillator* α1 subunit (Simon, 1997) or a human hyperekplexia-related GlyR mutant (Becker et al., 2002). Glycine transporter 2 knock-out mice also display 15-25 Hz tremor

(Gomeza et al., 2003). These observations on the glycinergic system suggest that the tremor is primarily spinal in origin.

Ataxia. The ataxia exhibited by mGAT1-deficient mice (i.e., rotarod deficits) (Fig. 3*C,D*; broader paw angle in *E,F*) is more likely to originate from a specific cerebellar defect, because ablation of GABAergic neurons in the cerebellum also causes ataxia in several classic mouse mutants. Overall, these results illustrate that normal motor control depends on maintaining appropriate levels of both phasic and tonic $GABA_A$ receptor-mediated inhibition in the cerebellum.

Nervousness versus anxiety. Nervousness describes the clinical side effects of tiagabine (Dodrill et al., 1997, 1998, 2000; Adkins and Noble, 1998). In the absence of an accepted test for nervousness in rodents, we assumed that it can be assessed as a mild form of anxiety. The GAT1 KO mice show such a phenotype. In the open-field test, mGAT1-deficient mice display delayed exploratory activity and decreased frequency of visits to the central area (Fig. 4*A-C*). However, the reduced rearing (Fig. 4*D*) could be caused by simply the decreased motor ability that leads to the lowered stance (Fig. 3*B*); there was only moderately reduced walking speed (Fig. 4*E*) and no reduction in total distance traveled (Fig. 4*F*). Furthermore, mutant mice show no difference in acoustic startle response compared with WT (Fig. 5*C*), but they display a dramatic decrease in prepulse inhibition of the acoustic startle response (Fig. 5*D*). The mGAT1 KO displays reduced home-cage activity, but the modest decrement in open-field walking speed suggests that mutant mice remain active when

encountering novel environments, whereas they display reduced activity in a habituated environment (Fig. 5*A,B*). In contrast, 5-HT transporter null mice exhibit a classical pattern of increased anxiety-like behavior in the elevated plus maze, in light-dark exploration and emergence tests, and in open-field tests (Holmes et al., 2003).

It is also true that many classical anxiolytic drugs operate by increasing the activity of $GABA_A$ receptors. Likewise, reduced GABA also causes anxiety; for example, GAD65 knock-out mice exhibit increased anxiety-like behavior in both the open-field and elevated-zero maze assays (Kash et al., 1999).

Reduced body weight. The reduced body weight of mGAT1 KO mice (Fig. 1*F*) contrasts with obesity of transgenic mice overexpressing mGAT1 under nonspecific or pan-neuronal promoters (Ma et al., 2000). GABA-related regulatory mechanism of feeding behavior in the ventro-medial hypothalamus may be responsible for impaired responses to glucoprivation in genetically obese rats (Tsujii and Bray, 1991). Benzodiazepine-treated rats lose body weight, presumably via activation of $GABA_A$ receptors (Blasi, 2000). Excess GABA in the anterior piriform cortex region reduces feeding (Truong et al., 2002). We believe that the reduced body weight and tremor is not related to delayed (or retarded) development, because mGAT1 KO mice are reproductive at the same time as WT and display muscle strength and balance similar to WT. Additional detailed studies are required.

Thermoregulation and circadian rhythm. Thermoregulation is controlled by several brain regions, including the horizontal limb of the diagonal band of

Broca (HDB), the basal forebrain, the preoptic area (POA), and the rostral part of the raphe pallidus nucleus (rRPa). Many neurons in these areas are GABAergic. In the HDB, muscimol reduces thermosensitivity (Hays et al., 1999) and, in the rRPa, muscimol to rRPa blocks fever and thermogenesis in brown adipose tissue induced by intra-POA as well as by intracerebroventricular prostaglandin E2 applications (Nakamura et al., 2002).

We know of no clinical studies on temperature effects of tiagabine. However, the higher amplitude of hyperthermic episodes in the mGAT1 KO mouse (Fig. 7) clearly does not phenocopy the acute hypothermic effects of tiagabine in rodents (Inglefield et al., 1995). Interestingly, $GABA_B$ activation leads to hypothermia (Schuler et al., 2001), but we found previously that the presynaptic $GABA_B$ response is diminished or lost in mGAT1 KO mice (Jensen et al., 2003), which may explain the discrepancy.

Although GABA has been related to circadian rhythm in many publications (Liu and Reppert, 2000; Wagner et al., 2001), the mGAT1-deficient mice did not display obvious changes in circadian rhythm during 5 d of testing either in constant dark or in a 12 h light/dark cycle environment. These results suggest that excess GABA does not affect circadian rhythm.

An additional use for knock-out mice strains. To the other useful information obtained from knock-out mouse strains, we may add the decision regarding whether the clinical side effects of a drug (in this case, tiagabine) arise from either widespread expression of its target or nonselective actions on other targets. Such information is particularly valuable when the pleiotropic effects

cannot readily be predicted from, but are certainly consistent with, the widespread and varied roles of the target molecule. Of course, such a study is rather straightforward when it is believed that the effects are mostly acute and subject to straightforward neurological tests (as in the present case), rather than delayed and primarily psychiatric (as for serotonin and perhaps dopaminergic and noradrenergic transporters).

This research was supported by National Institutes of Health Grants DA-01921, NS-11756, MH-49176, NS-030549, and DA-010509, National Science Foundation Grant 0119493, the Wellcome Trust, a Royal Society-Wolfson Award (S.C.-C.), and a Della Martin Fellowship (C.-S.C.). We are indebted to members of Caltech and University of California Los Angeles groups for advice, Limin Shi and Paul Patterson for use and help with the startle system, and J. Crawley for comments on this manuscript.

REFERENCES

Adkins JC, Noble S (1998) Tiagabine. A review of its pharmacodynamic and pharmacokinetic properties and therapeutic potential in the management of epilepsy. Drugs 55: 437-460.

Aldenkamp AP, De Krom M, Reijs R (2003) Newer antiepileptic drugs and cognitive issues. Epilepsia 44 [Suppl 4]: 21-29.

Barakat L, Bordey A (2002) GAT-1 and reversible GABA transport in Bergmann glia in slices. J Neurophysiol 88: 1407-1419.

Becker L, von Wegerer J, Schenkel J, Zeilhofer HU, Swandulla D, Weiher H (2002) Disease-specific human glycine receptor α1 subunit causes hyperekplexia phenotype and impaired glycine- and $GABA_A$-receptor transmission in transgenic mice. J Neurosci 22: 2505-2512.

Blasi C (2000) Influence of benzodiazepines on body weight and food intake in obese and lean Zucker rats. Prog Neuropsychopharmacol Biol Psychiatry 24: 561-577.

Brickley SG, Cull-Candy SG, Farrant M (1996) Development of a tonic form of synaptic inhibition in rat cerebellar granule cells resulting from persistent activation of $GABA_A$ receptors. J Physiol (Lond) 497: 753-759.

Brickley SG, Revilla V, Cull-Candy SG, Wisden W, Farrant M (2001) Adaptive regulation of neuronal excitability by a voltage-independent potassium conductance. Nature 409: 88-92.

Chiu CS, Jensen K, Sokolova I, Wang D, Li M, Deshpande P, Davidson N, Mody I, Quick MW, Quake SR, Lester HA (2002) Number, density, and

surface/cytoplasmic distribution of GABA transporters at presynaptic structures of knock-in mice carrying GABA transporter subtype 1-green fluorescent protein fusions. J Neurosci 22: 10251-10266.

Dingledine R, Korn SJ (1985) γ-Aminobutyric acid uptake and the termination of inhibitory synaptic potentials in the rat hippocampal slice. J Physiol (Lond) 366: 387-409.

Dodrill CB, Arnett JL, Sommerville KW, Shu V (1997) Cognitive and quality of life effects of differing dosages of tiagabine in epilepsy. Neurology 48: 1025-1031.

Dodrill CB, Arnett JL, Shu V, Pixton GC, Lenz GT, Sommerville KW (1998) Effects of tiagabine monotherapy on abilities, adjustment, and mood. Epilepsia 39: 33-42.

Dodrill CB, Arnett JL, Deaton R, Lenz GT, Sommerville KW (2000) Tiagabine versus phenytoin and carbamazepine as add-on therapies: effects on abilities, adjustment, and mood. Epilepsy Res 42: 123-132.

Draguhn A, Heinemann U (1996) Different mechanisms regulate IPSC kinetics in early postnatal and juvenile hippocampal granule cells. J Neurophysiol 76: 3983-3993.

Engel JE, Wu CF (1998) Genetic dissection of functional contributions of specific potassium channel subunits in habituation of an escape circuit in *Drosophila*. J Neurosci 18: 2254-2267.

Gomeza J, Ohno K, Hulsmann S, Armsen W, Eulenburg V, Richter DW, Laube B, Betz H (2003) Deletion of the mouse glycine transporter 2 results in a hyperekplexia phenotype and postnatal lethality. Neuron 40: 797-806.

M, Rossi DJ, Attwell D (2002) Tonic and spillover inhibition of granule cells control information flow through cerebellar cortex. Neuron 33: 625-633.

Hays TC, Szymusiak R, McGinty D (1999) $GABA_A$ receptor modulation of temperature sensitive neurons in the diagonal band of Broca *in vitro*. Brain Res 845: 215-223.

Holmes A, Yang RJ, Lesch KP, Crawley JN, Murphy DL (2003) Mice lacking the serotonin transporter exhibit 5-HT_{1A} receptor-mediated abnormalities in tests for anxiety-like behavior. Neuropsychopharmacology 28: 2077-2088.

Ikegaki N, Saito N, Hashima M, Tanaka C (1994) Production of specific antibodies against GABA transporter subtypes (GAT1, GAT2, GAT3) and their application to immunocytochemistry. Brain Res Mol Brain Res 26: 47-54.

Inglefield JR, Perry JM, Schwartz RD (1995) Postischemic inhibition of GABA reuptake by tiagabine slows neuronal death in the gerbil hippocampus. Hippocampus 5: 460-468.

Isaacson JS, Solis JM, Nicoll RA (1993) Local and diffuse synaptic actions of GABA in the hippocampus. Neuron 10: 165-175.

Itouji A, Sakai N, Tanaka C, Saito N (1996) Neuronal and glial localization of two GABA transporters (GAT1 and GAT3) in the rat cerebellum. Brain Res Mol Brain Res 37: 309-316.

Jakab RL, Hamori J (1988) Quantitative morphology and synaptology of cerebellar glomeruli in the rat. Anat Embryol (Berl) 179: 81-88.

Jensen K, Chiu CS, Sokolova I, Lester HA, Mody I (2003) GABA transporter-1 (GAT1)-deficient mice: differential tonic activation of $GABA_A$ versus $GABA_B$ receptors in the hippocampus. J Neurophysiol 90: 2690-2701.

Kash SF, Tecott LH, Hodge C, Baekkeskov S (1999) Increased anxiety and altered responses to anxiolytics in mice deficient in the 65-kDa isoform of glutamic acid decarboxylase. Proc Natl Acad Sci USA 96: 1698-1703.

Kralic JE, O'Buckley TK, Khisti RT, Hodge CW, Homanics GE, Morrow AL (2002) Deletion of $GABA_A$ receptor ($GABA_A$-R) α1 subunit alters benzodiazepine (BZD) site pharmacology, function and related behavior. Soc Neurosci Abstr 28: 39.12.

Liu C, Reppert SM (2000) GABA synchronizes clock cells within the suprachiasmatic circadian clock. Neuron 25: 123-128.

Lu Y, Grady S, Marks MJ, Picciotto M, Changeux JP, Collins AC (1998) Pharmacological characterization of nicotinic receptor-stimulated GABA release from mouse brain synaptosomes. J Pharmacol Exp Ther 287: 648-657.

Ma YH, Hu JH, Zhou XG, Zeng RW, Mei ZT, Fei J, Guo LH (2000) Transgenic mice overexpressing gamma-aminobutyric acid transporter subtype I develop obesity. Cell Res 10: 303-310.

Mullen RJ, Eicher EM, Sidman RL (1976) Purkinje cell degeneration, a new neurological mutation in the mouse. Proc Natl Acad Sci USA 73: 208-212.

Nagy A, Delgado-Escueta AV (1984) Rapid preparation of synaptosomes from mammalian brain using nontoxic isoosmotic gradient material (Percoll). J Neurochem 43: 1114-1123.

Nakamura K, Matsumura K, Kaneko T, Kobayashi S, Katoh H, Negishi M (2002) The rostral raphe pallidus nucleus mediates pyrogenic transmission from the preoptic area. J Neurosci 22: 4600-4610.

Nielsen EB, Suzdak PD, Andersen KE, Knutsen LJS, Sonnewald U, Braestrup C (1991) Characterization of Tiagabine (NO-328), a new potent and selective GABA uptake inhibitor. Eur J Pharmacol 196: 257-266.

Nielsen TA, DiGregorio DA, Silver RA (2004) Modulation of glutamate mobility reveals the mechanism underlying slow-rising AMPAR EPSCs and the diffusion coefficient in the synaptic cleft. Neuron 42: 757-771.

Overstreet LS, Jones MV, Westbrook GL (2000) Slow desensitization regulates the availability of synaptic $GABA_A$ receptors. J Neurosci 20: 7914-7921.

Pellock JM (2001) Tiagabine (gabitril) experience in children. Epilepsia 42 [Suppl 3]: 49-51.

Pericic D, Bujas M (1997) Sex differences in the response to GABA antagonists depend on the route of drug administration. Exp Brain Res 115: 187-190.

Prut L, Belzung C (2003) The open field as a paradigm to measure the effects of drugs on anxiety-like behaviors: a review. Eur J Pharmacol 463: 3-33.

Radian R, Ottersen OP, Strorm-Mathisen J, Castel M, Kanner BI (1990) Immunocytochemical localization of the GABA transporter in rat brain. J Neurosci 10: 1319-1330.

Richerson GB, Wu Y (2003) Dynamic equilibrium of neurotransmitter transporters: not just for reuptake anymore. J Neurophysiol 90: 1363-1374.

Richerson GB, Wu Y (2004) Role of the GABA transporter in epilepsy. Adv Exp Med Biol 548: 76-91.

Rico B, Xu B, Reichardt LF (2002) TrkB receptor signaling is required for establishment of GABAergic synapses in the cerebellum. Nat Neurosci 5: 225-233.

Roepstorff A, Lambert JD (1992) Comparison of the effect of the GABA uptake blockers, tiagabine and nipecotic acid, on inhibitory synaptic efficacy in hippocampal CA1 neurones. Neurosci Lett 146: 131-134.

Roepstorff A, Lambert JDC (1994) Factors contributing to the decay of the stimulus-evoked IPSC in rat hippocampal CA1 neurons. J Neurophysiol 72: 2911-2926.

Rossi DJ, Hamann M (1998) Spillover-mediated transmission at inhibitory synapses promoted by high affinity α6 subunit $GABA_A$ receptors and glomerular geometry. Neuron 20: 783-795.

Schachter SC (2001) Pharmacology and clinical experience with tiagabine. Expert Opin Pharmacother 2: 179-187.

Schuler V, Luscher C, Blanchet C, Klix N, Sansig G, Klebs K, Schmutz M, Heid J, Gentry C, Urban L, Fox A, Spooren W, Jaton AL, Vigouret J, Pozza M, Kelly PH, Mosbacher J, Froestl W, Kaslin E, Korn R, et al. (2001) Epilepsy, hyperalgesia, impaired memory, and loss of pre- and

postsynaptic $GABA_B$ responses in mice lacking $GABA_{B(1)}$. Neuron 31: 47-58.

Simon ES (1997) Phenotypic heterogeneity and disease course in three murine strains with mutations in genes encoding for alpha 1 and beta glycine receptor subunits. Mov Disord 12: 221-228.

Suzdak PD (1994) Lack of tolerance to the anticonvulsant effects of tiagabine following chronic (21 day) treatment. Epilepsy Res 19: 205-213.

Suzdak PD, Frederiksen K, Andersen KE, Sorensen PO, Knutsen LJ, Nielsen EB (1992) NNC-711, a novel potent and selective gamma-aminobutyric acid uptake inhibitor: pharmacological characterization. Eur J Pharmacol 224: 189-198.

Thompson SM, Gahwiler BH (1992) Effects of the GABA uptake inhibitor tiagabine on inhibitory synaptic potentials in rat hippocampal slice cultures. J Neurophysiol 67: 1698-1701.

Truong BG, Magrum LJ, Gietzen DW (2002) GABA(A) and GABA(B) receptors in the anterior piriform cortex modulate feeding in rats. Brain Res 924: 1-9.

Tsujii S, Bray GA (1991) GABA-related feeding control in genetically obese rats. Brain Res 540: 48-54.

Wagner S, Sagiv N, Yarom Y (2001) GABA-induced current and circadian regulation of chloride in neurones of the rat suprachiasmatic nucleus. J Physiol (Lond) 537: 853-869.

Wall MJ, Usowicz MM (1997) Development of action potential-dependent and independent spontaneous $GABA_A$ receptor-mediated currents in granule cells of postnatal rat cerebellum. Eur J Neurosci 9: 533-548.

Watanabe D, Inokawa H, Hashimoto K, Suzuki N, Kano M, Shigemoto R, Hirano T, Toyama K, Kaneko S, Yokoi M, Moriyoshi K, Suzuki M, Kobayashi K, Nagatsu T, Kreitman RJ, Pastan I, Nakanishi S (1998) Ablation of cerebellar Golgi cells disrupts synaptic integration involving GABA inhibition and NMDA receptor activation in motor coordination. Cell 95: 17-27.

Weinert D, Waterhouse J (1999) Daily activity and body temperature rhythms do not change simultaneously with age in laboratory mice. Physiol Behav 66: 605-612.

Yan XX, Cariaga WA, Ribak CE (1997) Immunoreactivity for GABA plasma membrane transporter, GAT-1, in the developing rat cerebral cortex: transient presence in the somata of neocortical and hippocampal neurons. Brain Res Dev Brain Res 99: 1-19.

FIGURES

Fig 1

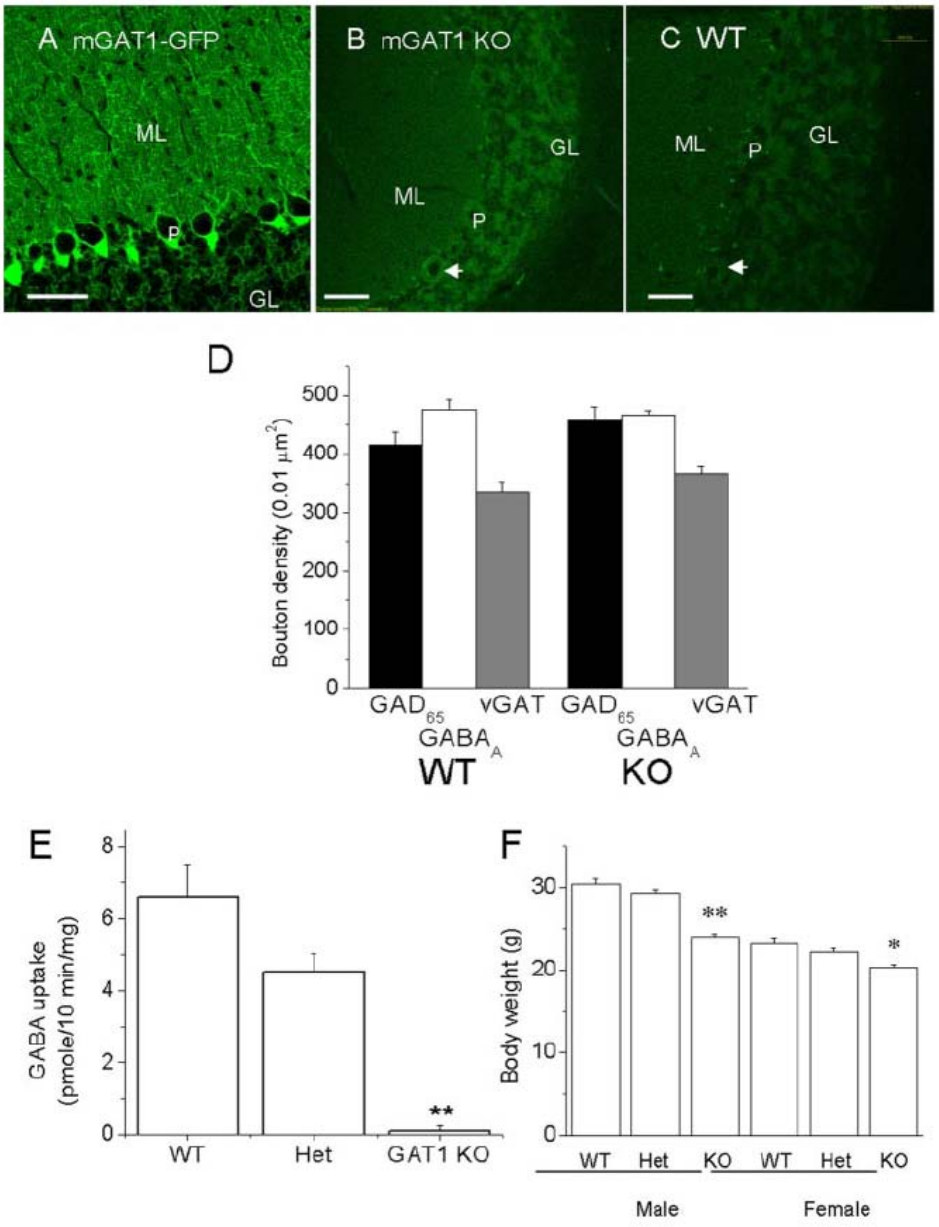

Figure 1. mGAT1 KO cerebellar images, synaptosomal GABA uptake, and body weight. ***A***, Fluorescent image of an mGAT1-GFP knock-in mouse cerebellar cortex, showing typical GAT1 expression pattern. ***B***, Fluorescent image of GAT1 KO showing no obvious GAT1 expression pattern. ***C***,WT mouse shows no obvious fluorescence. ***B*** and ***C*** were exposed to_20-fold greater photo power

than ***A***. GL, Granule cell layer; ML, molecular layer; P, Purkinje cell. Scale bar, 50_m.***D***, Quantification of GAD65, vGAT, and GABAA receptor-containing boutons in WT and KO mice based on the immunocytochemical staining (see supplemental figure for the actual images, available at www.jneurosci.org as supplemental material). ***E***, The NO711-sensitive synaptosomal [3H]GABA uptake activities among the three genotypes (mean_SEM; triplicate assays from each of two experiments with all three genotypes). ***E***, Decreased body weight of the GAT1 KO mouse. Data measured from 11 litters of het/het matings between the ages of 50 and 66 d are shown. Compared with WT littermates, male homozygotes weigh_20% less, whereas female homozygotes weigh _10% less. M, Male; F, female. WT, Het, KO: *n*_8, 17, 15 for males; *n*_11, 14, 8 for females. Differences fromWTat **p*_0.05 and ***p*_0.01.

Fig 2

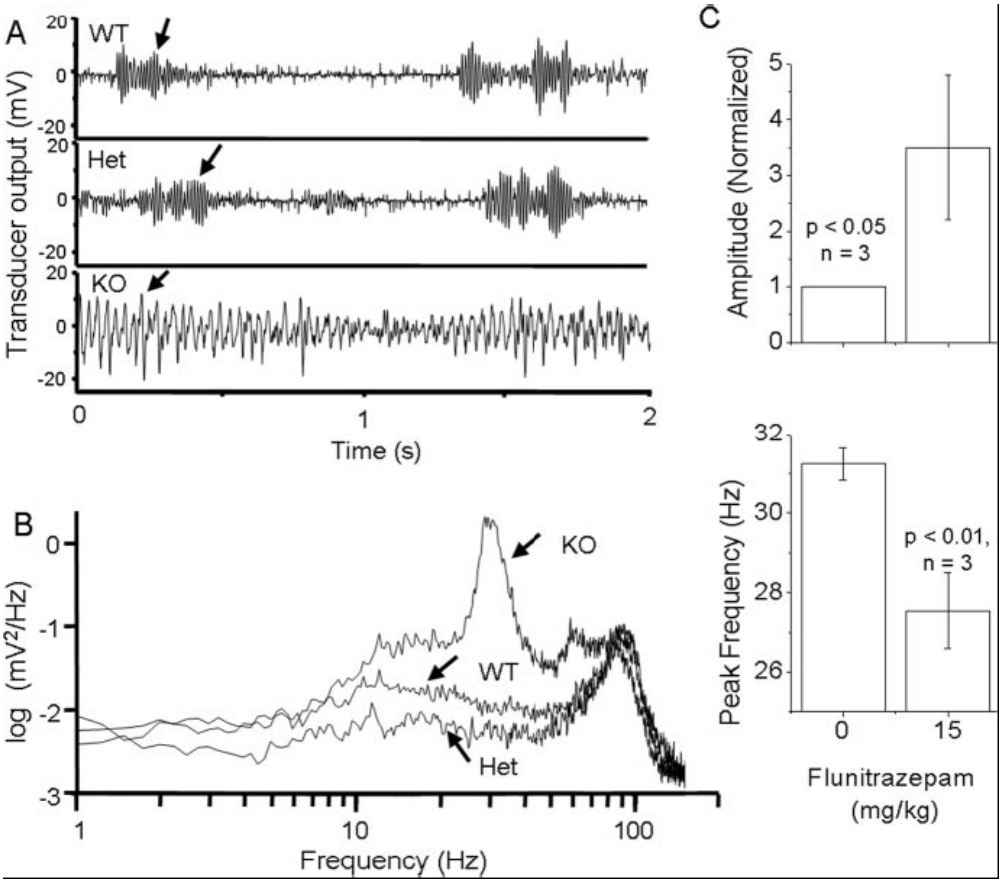

Figure 2. Characterization of mGAT1 KO tremor. ***A***, Recordings from the vibration transducer. Arrows (higher amplitude) indicate activities when forepaws were raised. ***B***, Power spectrum of the transducer signal for all genotypes. All genotypes shared a minor peak at ~80 Hz; however, only the KO showed a significant tremor at 25-32 Hz. ***C***, Modulation of tremor frequency and amplitude by flunitrazepam. Error bars represent SEM.

Fig 3

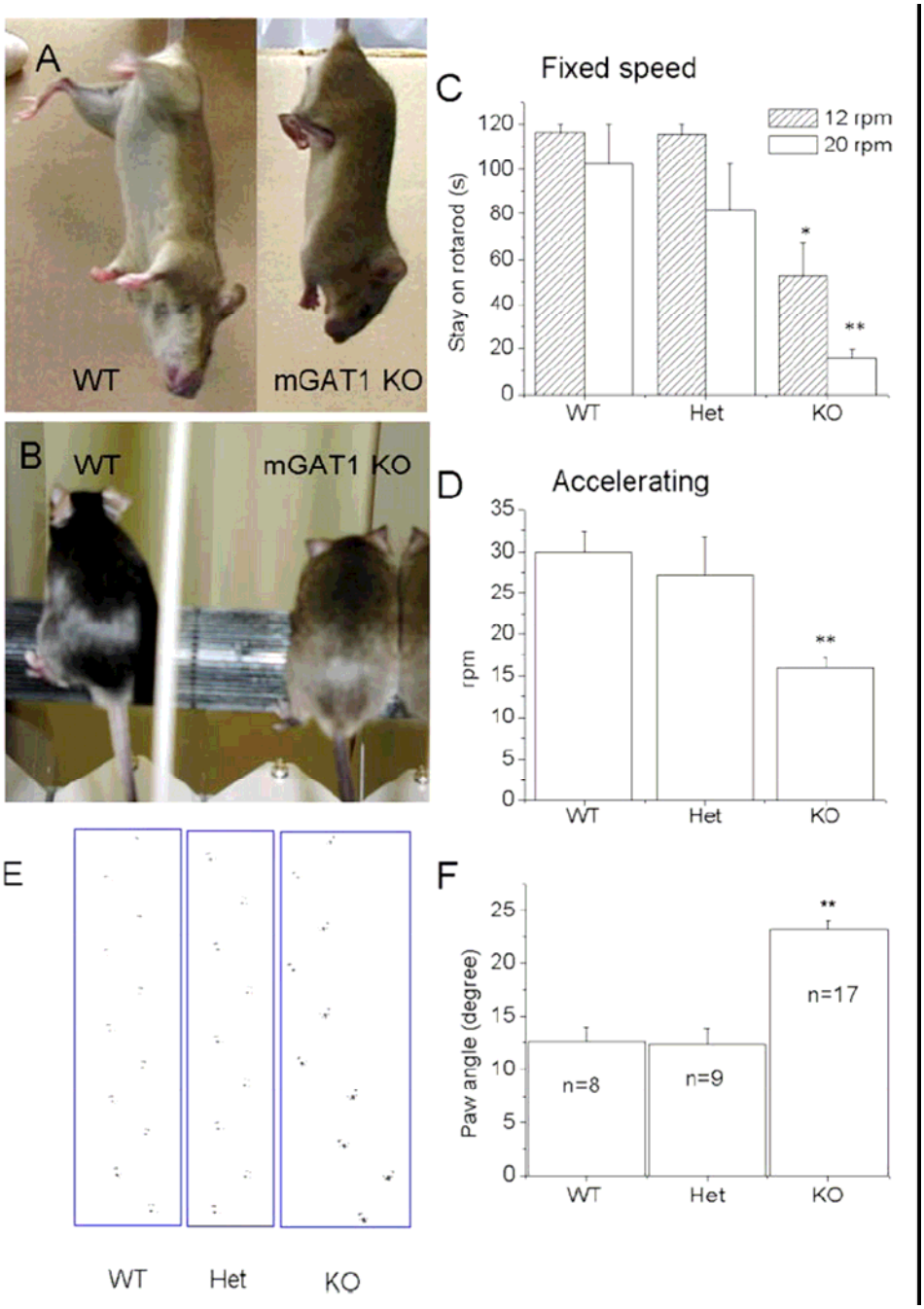

Figure 3. mGAT1 KO displays abnormal motor behavior. ***A***, WT (left) and mGAT1 KO (right) mice showed different gestures when hung by their tails. WT mice showed a typical extensor gesture, whereas KO mice showed flexor contraction. ***B***, Stance of WT and KO mice on the rotarod. The KO mice show flattened and lowered hips, and their paws move more slowly than WT mice. ***C***,

Mice were tested at fixed speed (either 12 or 20 rpm) on the rotarod. *n* = 6, 5, and 8 (WT, Het, and KO, respectively). ***D***, Mice were tested at accelerating speeds. KO mice fell significantly sooner than WT mice. ***E***, Abnormal gait. Hindpaw footprint pattern of WT, heterozygotes, and homozygotes is shown. The hindpaws of mGAT1 KO mice show a wider angle with respect to the direction of walking. The KO mouse seems to waddle. ***F***, Comparison of the average paw angles among WT (*n* = 8), Het (*n* = 9), and KO (*n* = 17) mice. The paw angle of the KO mouse is approximately twice as large as that of WT and heterozygotes (23 ± 1 vs 12.5 ± 1°). Differences from WT at $^{*}p < 0.05$ and $^{**}p < 0.01$.

Fig 4

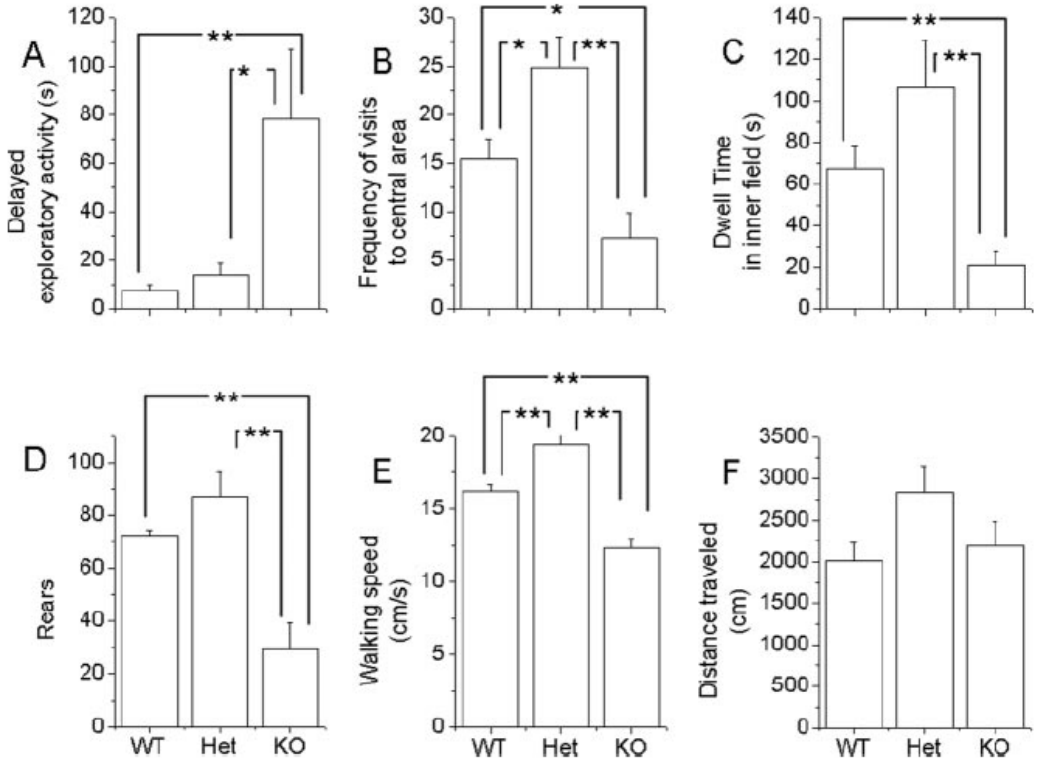

Figure 4. Characterization of mGAT1 KO exploratory activity in the open field. ***A***, The time required for mice to walk the first 50 cm in open field. Most WT and Het mice take <10 s, whereas KO mice spend 13-240 s. Points show mean ± SEM.

B, ***C***, The KO mouse shows reduced frequency (***B***) and reduced duration (***C***) visiting the central area in the open-field test. Total visits to the central area were 15 ± 2, 25 ± 3, and 7 ± 3, and total time to stay in the central area were 67 ± 11, 106 ± 23, and 21 ± 7s for WT, Het, and KO, respectively. ***D***, The GAT1 KO mouse showed reduced frequencies of rearing (73 ± 2, 87 ± 9, and 29 ± 10 for WT, Het, and KO, respectively). ***E***, The average walking speeds for WT, Het, and KO mice were 16.2 ± 0.5, 19.4 ± 0.6, and 12.3 ± 0.6 cm/s, respectively. ***F***, mGAT1 KO mice showed no obvious difference in total walking distance within 10 min (2000 ± 210, 2840 ± 320, and 2190 ± 300 for WT, Het, and KO, respectively). ***E***, n = 7, 12, and 10 (WT, Het, and KO, respectively). For all other panels, n = 6, 8, and 8 (WT, Het, and KO, respectively). $^{*}p < 0.05$; $^{**}p < 0.01$.

Fig 5

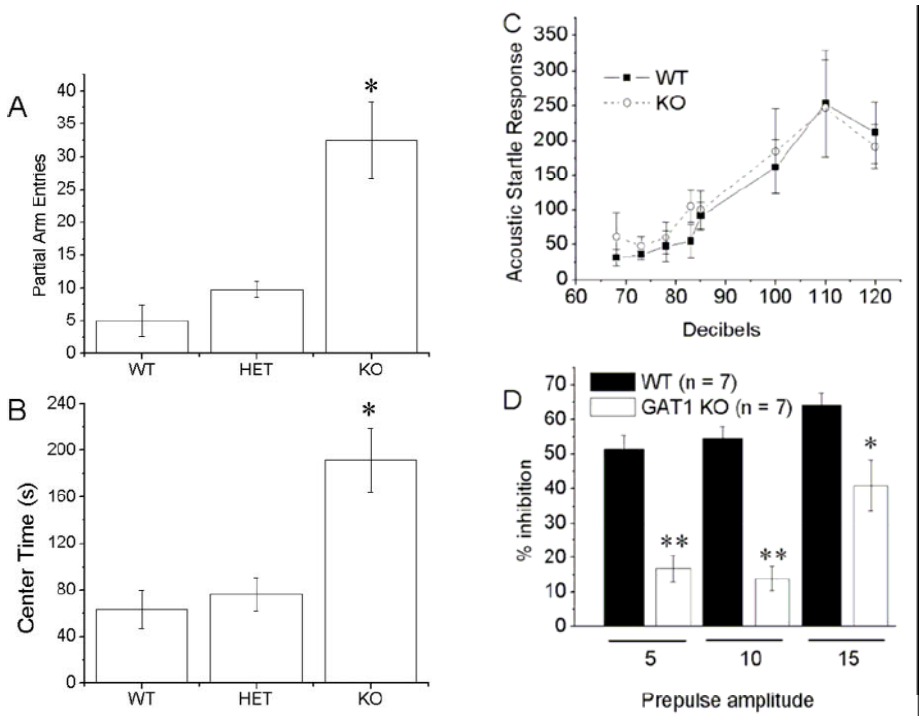

Figure 5. Additional anxiety-related behaviors: elevated plus maze and acoustic startle. mGAT1 KO mice display increased partial arm entries (***A***) and time spent in the central square (***B***) compared with WT mice. $^{*}p < 0.01$; $n = 4$ mice in each group. ***C***, Acoustic startle response of mutant (open circle; $n = 4$) and WT (filled square; $n = 4$) measured in arbitrary units. ***D***, Prepulse inhibition of mutant (open column; $n = 7$) and WT (filled column; $n = 7$). The 5, 10, and 15 under the *x*-axis refer to prepulses at 5, 10, and 15 dB, respectively, above the background level of 68 dB. The difference between KO and WT is significant at $^{*}p < 0.05$ and $^{**}p < 0.01$. Error bars represent SEM.

Fig 6

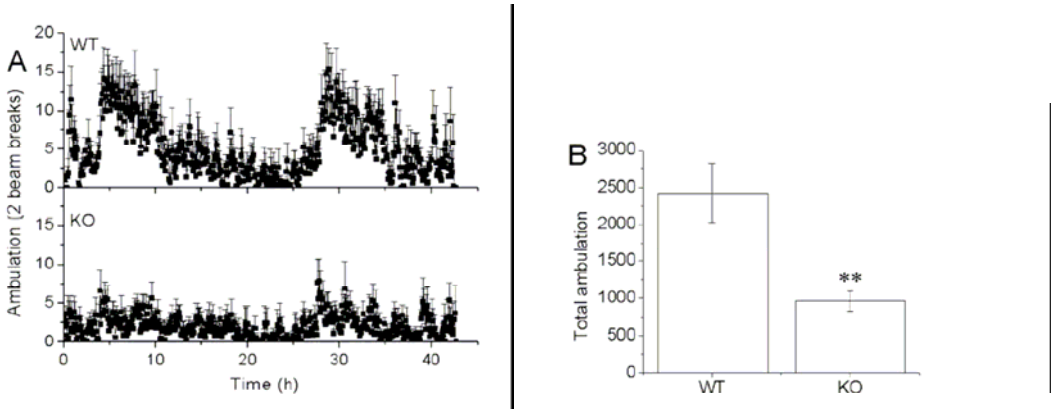

Figure 6. GAT1 KO mice showed reduced ambulation in home cages. ***A***, Profiles of ambulation activity of WT (top) and KO (bottom) mice over a 42 h recording period. WT displays a 24 h rhythm, whereas KO shows lower activity. ***B***, Total ambulation activity of KO and WT mice (2425 ± 395 and 965 ± 146 counts). Error bars represent SEM.

Fig 7

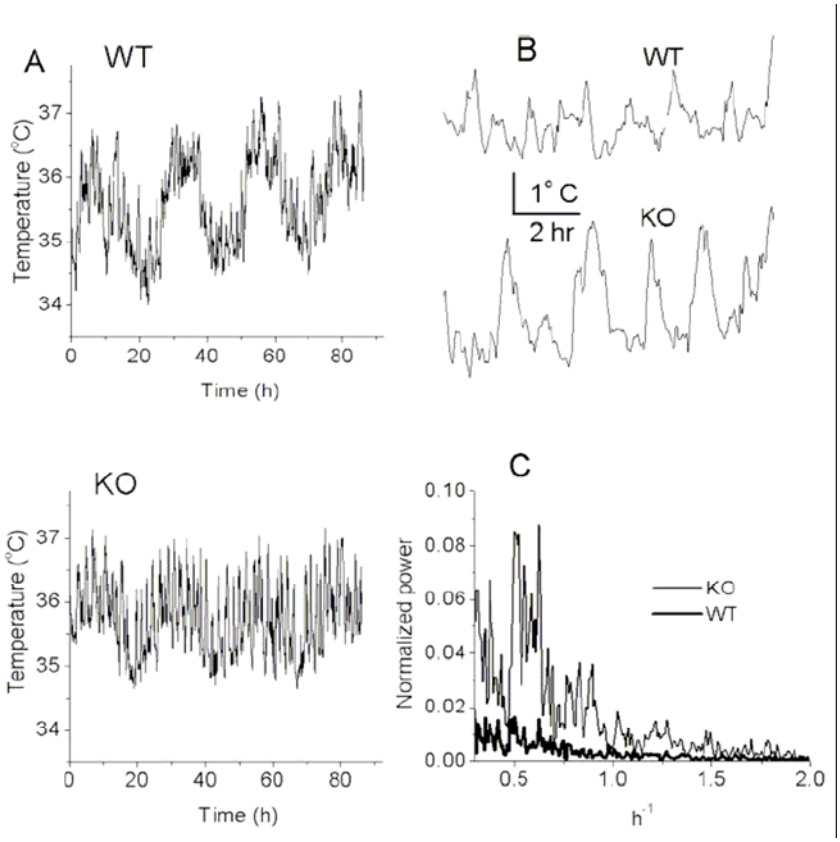

Figure 7. mGAT1-deficient mice display more body temperature fluctuations in the 0.2-1.5/h frequency range than WT mice. ***A***, Raw traces of body temperature fluctuation from one WT (top) and one mutant (bottom) mouse. Mutant mice display multiple hyperthermic episodes, especially during periods of higher activity (i.e., higher body temperature). ***B***, Expanded traces from ***A***. ***C***, Power spectrum analysis. The *y*-axis represents the average power (*n* = 4 KO, 3 WT) normalized to the peak at 24 h cycle as 100%. The *x*-axis represents the frequency (inverse hours).

Fig 8

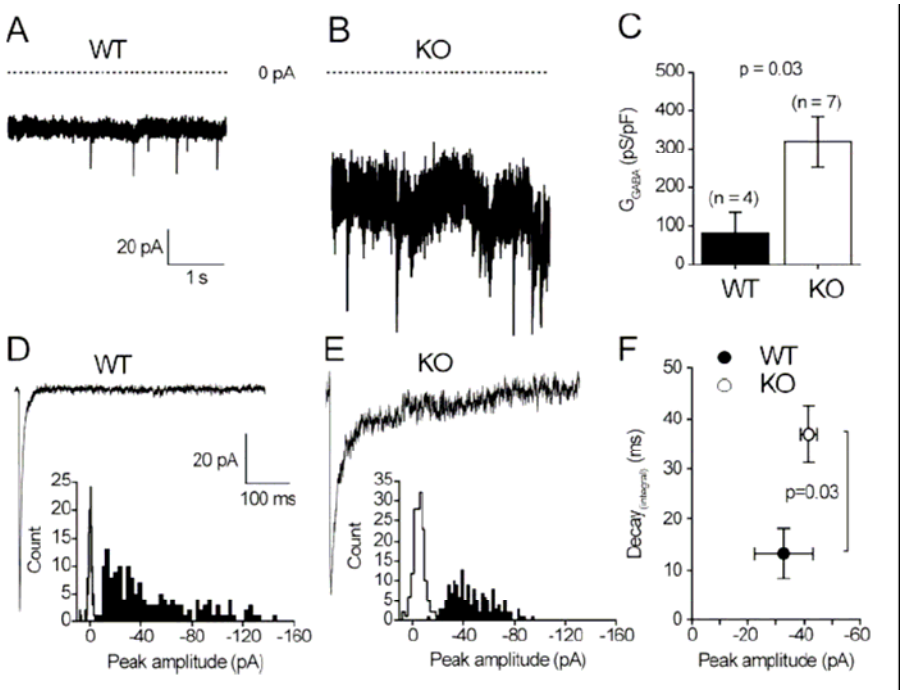

Figure 8. mGAT1 KO cerebellar granule cells are characterized by an increased tonic $GABA_A$-mediated conductance and prolonged IPSCs. ***A***, ***B***, Continuous current records from typical wild-type (***A***) and mGAT1 KO (***B***) internal granule cells voltage clamped at -70 mV. The horizontal line indicates the 0 current level in each recording. There is an increased inward current in mGAT1 KO cells and a substantial increase in the current variance associated with this conductance. This increased tonic conductance is completely blocked by the $GABA_A$ receptor antagonist SR95531 (gabazine). ***C***, The bar graph illustrates that, on average, G_{GABA} in GAT1 KO granule cells was 319 ± 65 pS/pF (*n* = 7) compared with 84 ± 50 pS/pF (*n* = 4) in control littermates. This resembles the 98 ± 20 pS/pF G_{GABA} recorded previously in the C57BL/6 strain (Brickley et al., 2001□). Therefore, the tonic conductance tripled after the removal of GAT1, indicating a raised concentration of ambient GABA in the slice preparation. ***D***, ***E***, Two average sIPSC waveforms recorded from a wild-type (***D***) and an mGAT1 KO (***E***) granule

cell are shown on the same scale. The waveforms have similar peak amplitudes but very different decays. The histograms also illustrate the peak amplitude distribution of all sIPSCs recorded in these cells. The open histograms were constructed from periods of baseline noise. As shown by the increase in the width of the baseline histogram for mGAT1 KO, the increased current variance associated with mGAT1 KO recordings does complicate interpretation of peak amplitude measurements. It is possible that we are missing a significant fraction of small events in the mGAT1 KO, because they would be unresolved in the noisy mGAT1 KO recordings. However, this possible artifact does not affect the decay estimates, because the decay of sIPSCs is not correlated with peak amplitude in granule cells (data not shown). ***F***, The significant increase in the decay of sIPSC recorded from mGAT1 KO granule cells. The decay was defined as $\tau_{integral}$ (see Materials and Methods). The $\tau_{integral}$ of control littermates was 13 ± 5 ms (n = 4) compared with 37 ± 6 ms (n = 5) in the mGAT1 KO animals. In contrast, there was no significant difference between the average peak amplitudes recorded in the two strains. Error bars represent SEM.

Fig 9

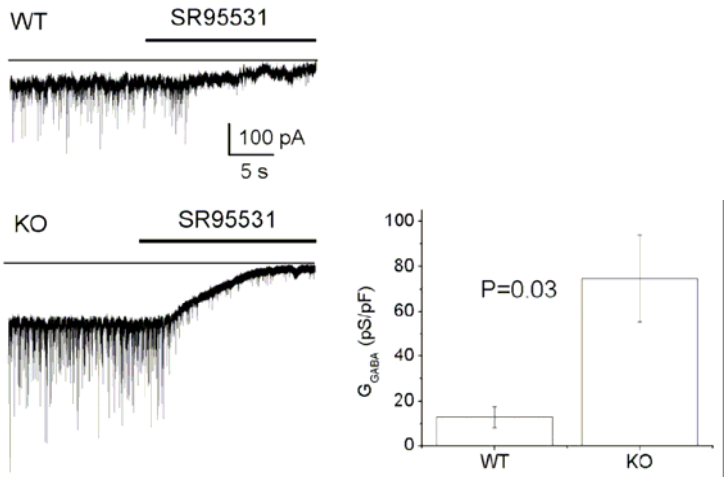

Figure 9. mGAT1 KO mice display higher tonic currents in cerebellar Purkinje cells. In both WT and mGAT1 KO slices, sIPSCs were recorded in Purkinje cells by holding at -70 mV. Zero current levels are shown in the light trace. Injection of SR95531 into the bath (>100 μM; heavy trace) blocked tonic current and sIPSCs. Average tonic currents in mGAT1 KO cells are approximately six times larger than in WT cells [75 ± 19 and 13 ± 5 pS/pF for KO (*n* = 10) and WT (*n* = 9), respectively]. Error bars represent SEM.

Appendix C

Atypical expansion in mice of the sensory neuron-specific Mrg G protein-coupled receptor family.

Zylka MJ, Dong X, Southwell AL, Anderson DJ.
PNAS. 2003,100(17):10043-8.

ABSTRACT

The Mas-related genes (Mrgs) comprise a family of >50 G protein-coupled receptors (GPCRs), many of which are expressed in specific subsets of nociceptive sensory neurons in mice. In contrast, humans contain a related but nonorthologous family of genes, called MrgXs or sensory neuron-specific receptors, of which many fewer appear to be expressed in sensory neurons. To determine whether the diversity of murine Mrgs is generic to rodents or is an atypical feature of mice, we characterized MrgA, MrgB, MrgC, and MrgD subfamilies in rat and gerbil. Surprisingly, although mice have approximately 22 MrgA and approximately 14 MrgC genes, rats and gerbils have just a single MrgA and MrgC gene. This murine-specific expansion likely reflects recent retrotransposon-mediated unequal crossover events. The expression of Mrgs in rat sensory ganglia suggests that the extensive cellular diversity in mice can be simplified to a core subset of approximately four different genes (MrgA, MrgB, MrgC, and MrgD), defining a similar number of neuronal subpopulations. Our results suggest more generally that mouse-human genomic comparisons may sometimes reveal differences atypical of rodents.

INTRODUCTION

In many sensory systems, including taste, olfaction, and vision, primary sensory neurons express diverse families of seven transmembrane domain G protein-coupled receptors (GPCRs) to detect and discriminate among various chemical and visual stimuli (1–3). The expansion of diverse GPCR families is enabled by the fact that functional receptors and their transcriptional controls often reside within small (≈10-kb) segments of DNA present in tandem arrays (4–6). The success of this molecular unit is reflected in the fact that GPCRs constitute the largest single gene family in all metazoan genomes (7–10).

Recent studies have identified a novel family of GPCRs specifically expressed in primary nociceptive sensory neurons in mice and humans (11, 12). *In vitro* studies suggest that some of these receptors can be activated by neuropeptides that contain C-terminal -RF(Y)amide or -RF(Y)G motifs (11–13). Members of this family have been referred to as Mas-related genes (*Mrgs*) (11, 14, 15). Alternatively, in humans they have been called sensory neuron-specific receptors (*SNSRs*) (12). In mice, the *Mrg* family is comprised of six single-copy genes (*MrgD, MrgE, MrgF*/*RTA, MrgG, MrgH*/*GPR90*, and *MAS1*), as well as three large clades or subfamilies (*MrgA, MrgB,* and *MrgC*) that together comprise ≈50 distinct sequences. The differential expression of various mouse (*m)Mrgs* defines a surprisingly diverse axis of cellular heterogeneity among murine nociceptive sensory neurons, the functional significance of which is currently unclear (11).

In contrast to the extensive sequence diversity exhibited by *mMrgA, mMrgB*, and *mMrgC* subfamilies, in humans there are only four functional *hMrgX*/*SNSR* genes. Although some of these genes are specifically expressed in nociceptive sensory neurons like their murine counterparts, none of the human and mouse genes are strictly orthologous (11). This difference raises the question of whether the extensive *Mrg* sequence diversity characteristic of mice is generic to rodents, perhaps reflecting differences with humans in nociceptive physiology, or rather reflects genomic expansion events unique to mice.

To address this question, we have characterized the complement of *Mrg* genes in two other rodent species, rat and gerbil.

Our results indicate that the extreme diversity of murine *Mrgs* is an atypical feature of mice. These findings simplify the problem of understanding the functional significance of *Mrg* sequence diversity in rodents to a core set of approximately four different genes (*MrgA, MrgB, MrgC*, and *MrgD*), defining a similar number of neuronal cell populations.

METHODS

Distance Calculations. Representative nucleotide sequences from the coding regions of *MrgA* (*mMrgA1-A8, rMrgA*), *MrgB* (*mMrgB1-B5, mMrgB7-B8, rMrgB1, rMrgB2, rMrgB5-B6, rMrgB8*), and *MrgC* (*mMrgC1, mMrgC2, mMrgC7, mMrgC11, rMrgC*) subfamilies were aligned with clustalw and then manually aligned on a codon-by-codon basis. Nucleotides that introduced gaps within a codon were removed from the analysis (complete-deletion option). The program

diverge was then used to calculate the number of pairwise synonymous (K_s) and nonsynonymous (K_a) nucleotide substitutions between *mMrgAs, mMrgBs, rMrgBs*, and *mMrgCs* by using the method described by Li *et al.* (16–18) with recent modifications. A neutral substitution rate of $4.5 = 10^{-9}$ substitutions per synonymous site (K_s) per year was used to calculate evolutionary distance between each pair of sequences (10). This rate was based on the assumption that humans and rodents last shared a common ancestor 75 million years ago (MYA), and it is similar to the neutral substitution rate for rodents calculated by others (19).

The details describing how rat and gerbil *Mrgs* were cloned as well as methods for *in situ* hybridizations and Southern blot hybridizations can be found in *Supporting Methods*, which is published as supporting information on the PNAS web site, www.pnas.org.

RESULTS

Identification of the Rat Mrg Family. Searches of the January 21, 2003, release of the rat genome using mouse *Mrgs* as query sequences revealed that the rat has a single copy each of rat (*r)MrgA* and *rMrgC* (Fig. 1*A*). These two rat genes have been previously characterized as an adenine receptor and *rSNSR*, respectively (12, 20). However, the total number of rat *Mrgs* was not systematically examined in these previous studies. Our searches also identified 10 *rMrgBs*, many of which are orthologous to at least one of the mouse *MrgB* genes (Fig. 6, which is published as supporting information on the PNAS web

site). The mouse and rat *MrgB* subfamily was divided further into phylogenetically defined B2, B4, and B8 subdivisions (Figs. 1 *A* and 6).

The rat genomic dataset also contained complete sequences of *rMrgD, rMrgE, rMrgF*/*RTA, rMrgG, rMrgH*/*GPR90*, and *rMAS1*. With the exception of *MrgH*, which has not been identified in humans, these genes all have orthologs in mice and humans. As in mice, we were unable to identify rat genes that are orthologous to the human *MrgX* subfamily or to *hMrg*, the first Mas-related gene identified in humans (14). Taken together, these data indicate that rats and mice contain orthologous sets of the *MrgA, MrgB, MrgC*, and *MrgD* genes, albeit in different numbers, and that neither species contains genes orthologous to human *MrgX*/*SNSRs*.

Because our bioinformatic analysis was based on draft genomic sequence, we performed Southern blot experiments to confirm the copy number of rat *Mrg* genes. We used probes that covered most of the coding regions of *rMrgA, rMrgB2, rMrgB4, rMrgB8, rMrgC*, and *rMrgD*. Because the coding region of each *Mrg* is contained within a single exon (11), the number of bands of equivalent intensity on a Southern blot approximates the number of genes. Control experiments using mouse genomic DNA indicated that the rat *Mrg* probes were capable of hybridizing to at least 10 genes in the *mMrgA* and *mMrgC* subfamilies [Fig. 1*B*, lanes *rMrgA* (M) and *rMrgC* (M)]. Analysis of rat genomic DNA [Fig. 1*B* (R)] revealed one band each for *rMrgA, rMrgC, rMrgB8* (B8 subdivision), and *rMrgD*; at least four strong bands for *rMrgB2* (B2 subdivision), and two strong bands for *rMrgB4* (B4 subdivision). The weaker

bands detected by the *rMrgB4* probe are likely due to cross-hybridization with other *rMrgB2*-like genes (note size similarities between *MrgB2* and *MrgB4* lanes). The number of bands detected by Southern blot analysis was therefore well correlated with the number of genes identified by our database searches.

Identification of Gerbil Mrg Family Members. The contrasting results in rat and mouse raised the question of whether the diversity of murine *Mrgs* represents the exception, or rather the rule, among rodents. To address this question, we characterized *Mrgs* from a third murid rodent, the Mongolian gerbil (*Meriones unguiculatus*). Because genomic sequence data are currently not available for this species, our approach was restricted to experimental analysis. First, using degenerate PCR primers and gerbil liver genomic DNA as the template, we identified gerbil orthologs of *MrgB1, MrgB4*, and *MrgD*. On the basis of a phylogenetic analysis, gerbil (*g)MrgB1* and *gMrgB4* are located in the B2 and B4 subdivisions, respectively (Fig. 6). Despite numerous attempts, we were unable to amplify gerbil *MrgA* or *MrgC* sequences with degenerate primers.

We therefore conducted a Southern blot analysis of gerbil genomic DNA using rat *MrgA* and *MrgC* probes. That these rat probes strongly cross-hybridized to their murine orthologs under our hybridization conditions (Fig. 1*B*) suggested they would likely cross-hybridize to their gerbil orthologs as well. Consistent with this expectation, the rat *MrgA* and *MrgC* as well as the *MrgD* probes cross-hybridized to gerbil DNA, revealing single intense bands of 7.5, 1.5, and 8 kb, respectively (Fig. 1*B*, lanes G). The two additional weak bands revealed by the *rMrgC* probe likely represent cross-hybridization to *gMrgA* and/or a restriction

fragment of *gMrgC*. These data suggest that, like the rat, the gerbil has a single copy of *MrgA* and *MrgC* and a single copy of *MrgD*, like all mammals thus far examined.

Gerbil DNA was also probed with *rMrgB* probes. We detected a total of three bands that cross-hybridized to both the *rMrgB2* and *rMrgB4* probes, albeit with different intensities to each (Fig. 1*B*). The 3.5- and 11-kb bands correspond to *gMrgB1* and *gMrgB4*, respectively, as determined by probing duplicate blots with gerbil *MrgB1* and *MrgB4* DNA probes (data not shown). The 1.1-kb band did not hybridize to the *rMrgB8* probe, and its identity is unknown. It could represent an additional gerbil *MrgB* gene or a restriction fragment of *gMrgB1* or *gMrgB4*. Taken together, these data suggest that gerbil has at least two, and possibly three, *MrgB* genes, a number significantly less than mouse or rat (Fig. 1*C*).

Expansion of the MrgA, MrgB, and MrgC Subfamilies Occurred at Different Times During Rodent Evolution. The foregoing data suggested that the murine genome contains a far greater number of *Mrgs* than either the rat or the gerbil. This difference could reflect an evolutionary contraction of the family that occurred in the latter two species or a selective expansion in the mouse. To distinguish between these alternatives, we determined the evolutionary times at which expansions of the different *Mrg* subfamilies occurred in mice, in relation to the times of speciation of rat, mouse, and gerbil (see *Methods*). These calculations suggested that the mouse *MrgA* and *MrgC* subfamilies each diverged from their respective common ancestors 10–25 MYA (Fig. 2), corresponding to a time shortly after, or coincident with, the speciation of rats and

mice, and ≈25–45 million years after the speciation of gerbils from the rat–mouse lineage (21–23). Thus the larger sizes of the *MrgA* and *MrgC* subfamilies in mouse are consistent with an evolutionarily late selective expansion in that species.

In contrast to the results for the *MrgA* and *MrgC* subfamilies, the divergence times for *MrgB* gene pairs generally occurred before rat–mouse speciation but fell over a much broader window of evolutionary time spanning 10–80 MYA (Fig. 2). Pairwise (rat–rat and mouse–mouse) comparisons between members of the three different *MrgB* subdivisions (B2, B4, and B8) yielded average divergence times of 71 ± 6, 66 ± 4, and 70 ± 3 MYA (±SD) for B2–B4, B2–B8, and B4–B8 comparisons, respectively. The small variability in these numbers, combined with their similar absolute values, suggests that the B2, B4, and B8 subdivisions originated from a single ancestral *MrgB* gene ≈65–70 MYA. That this divergence occurred shortly before or during the time that rats and mice were predicted to have speciated from gerbils is consistent with our identification of one gerbil *MrgB* gene in each of the B2 and B4 subdivisions. The average divergence time calculated for rat or mouse *MrgB* members within each subdivision was 34 ± 17 MYA, consistent with the idea that these subdivisions expanded after the divergence of rats and mice from the gerbil lineage. Thus, it appears that at least two subdivisions of the *MrgB* family are likely present in all rodents but differ in size due to additional expansion events (Fig. 1*C*).

Mrgs Expressed in Sensory Neurons Are Positioned Adjacent to One Another in the Genome. To determine whether rat *Mrgs* are expressed in

sensory neurons like their murine counterparts, we performed *in situ* hybridization experiments with tissue from newborn and adult rats. These experiments indicated that *rMrgA, rMrgB4, rMrgB5, rMrgC*, and *rMrgD* were all expressed strongly in newborn dorsal root ganglia (DRGs), adult DRGs, and trigeminal ganglia (gV; Figs. 3 and 4; data not shown). Others have similarly reported expression of *rMrgA* and *rMrgC* exclusively in adult rat DRG neurons (12, 20). In contrast, we did not detect expression of *rMrgB1, rMrgB2, rMrgB3, rMrgB6*, or *rMrgB8* in sensory neurons. Although we have not looked exhaustively, none of our *rMrg* probes clearly hybridized to any other tissues or organs in postnatal day 0 animals. As in the rat, *mMrgB4* and *mMrgB5* were likewise expressed in adult mouse DRG neurons (see below), although not in newborn DRG neurons (11). Taken together, these data indicate that genes within the *MrgB* B4 subdivision, but not the B2 or B8 subdivisions, are expressed in sensory neurons like *MrgA, MrgC*, and *MrgD*.

The sensory neuron-specific expression of rat *Mrgs* raised the possibility that they might be clustered together within the genome, like olfactory and vomeronasal GPCRs (6, 24, 25). Using the draft rat genome assembly as a guide, we found that most of the *rMrg* family members map to rat chromosome 1 (Fig. 3*B*, Rn). The *rMrgA, rMrgB*, and *rMrgC* genes are found together within a 760-kb cluster (the *MrgABC* cluster), and the *rMrgD, rMrgE, rMrgF*, and *rMrgG* genes are found together within a 1.9-Mb cluster (the *MrgDEFG* cluster). All of the *Mrgs* from the *MrgABC* cluster expressed in sensory neurons are adjacent to one another in the rat genome. Within this cluster, the *MrgBs* are arranged along

the chromosome in a centromeric to telomeric orientation, within phylogenetically defined B4, B8, and B2 subdivisions.

Analysis of the assembled mouse genome revealed a similar arrangement of *mMrgs* into phylogenetically segregated *mMrgABC* and *mMrgDEFG* clusters on syntenic regions of mouse chromosome 7 (Fig. 3*B*, Mm). Furthermore, the murine *mMrgA* and *mMrgC* genes were generally found as a repeat of $(A\text{-}A\text{-}C)_n$. This arrangement may explain why there are roughly twice as many *mMrgAs* (*n* = 22) as *mMrgCs* (*n* = 14) (11). The clustering of *Mrgs* with sensory neuron-specific expression suggests the presence of a locus control region and/or that the gene duplication events expanding these subfamilies included local cell type-specific transcriptional regulatory elements.

To obtain more clues about how the *MrgABC* cluster could have evolved, we searched assembled genomic sequences surrounding the rat and mouse *MrgABC* cluster for repetitive elements with the repeatmasker program (http://ftp.genome.washington.edu). For comparison, we searched a similar stretch of assembled genomic DNA surrounding the rat and mouse *MrgD* and *MrgF* cluster. This search revealed that the mouse and rat *MrgABC* clusters are intercalated with very large amounts of LINE1/L1 retrotransposon sequences (mouse *MrgABC* cluster = 43.2% L1; rat *MrgABC* cluster = 48.3% L1) (Figs. 7 and 8, which are published as supporting information on the PNAS web site). In contrast, the rat and mouse *MrgD* and *MrgF* cluster contains very few L1 elements or other repeats (mouse *MrgDF* cluster = 0.76% L1; rat *MrgDF* cluster = 0.58% L1). We also noticed that L1 retrotransposon sequences were found

only at the 5′ end of the *rMrgA* coding exon but were found at the 5′ and 3′ ends of the coding exon of most *mMrgAs* (Figs. 7 and 8). These repeat elements may have played a role in the expansion of the *MrgABC* cluster (see *Discussion*).

Similar Subpopulations of Nociceptive Sensory Neurons Are Defined by Mrg Receptor Expression in Rat and Mouse. Nociceptive primary sensory neurons fall into many different subclasses. These subclasses can be distinguished on the basis of their function, neurotrophin dependence, and expression of molecular markers (26, 27). One such subclass expresses the glial cell line-derived neurotrophic factor (GDNF) receptor c-Ret and binds *Griffonia simplicifolia* isolectin IB4 (28). This GDNF-dependent subset has been implicated in neuropathic and inflammatory pain, conditions for which current analgesics are inadequate (29–34). In the mouse, *Mrgs* are expressed exclusively within this subset of nociceptors (11). We therefore wished to determine whether the restriction of *Mrg* expression to this neuronal subclass was conserved in the rat.

As in the mouse, we found that all *rMrgB4* $^+$, *rMrgC* $^+$, and *rMrgD* $^+$ (all of which are *rMrgA* $^+$; see below) neurons were also IB4 binding$^+$ and c-Ret$^+$ (Fig. 4*A*; Table 1, which is published as supporting information on the PNAS web site). Within this population, *rMrgD* $^+$ cells were approximately two and three to four times more numerous than *rMrgB4* $^+$ or *MrgC* $^+$ cells, respectively, similar to the situation in mouse (Table 1). As in the mouse, the *MrgD* $^+$ subset of c-Ret$^+$ cells coexpressed the purinergic receptor P2X3 (11). The main difference between rat and mouse was that in the rat, all *rMrgD* $^+$ cells [as well as a minority (7%) of *rMrgC* $^+$ cells] express the capsaicin receptor VR1 (Fig. 4*A* and Table 1),

whereas most or all *Mrg*-expressing cells are $VR1^{-}$ in the mouse (11). In addition, in the mouse, only *mMrgD* $^{+}$ neurons coexpress the purinergic receptor P2X3, whereas in the rat, all *Mrg* $^{+}$ neurons are $P2X3^{+}$ (Fig. 4*A*). Taken together, these studies indicate that in rats, as in mice, *Mrgs* are restricted to the GDNF-dependent subset of nociceptive sensory neurons but display subtle differences in the other signaling molecules that they coexpress (Fig. 4*B*).

In the mouse, *Mrg* expression defines multiple subsets of neurons within the $IB4^{+}/Ret^{+}$ population (11). Because rats have a much smaller number of *Mrgs*, we next performed a series of double-label *in situ* hybridization experiments to determine how many adult DRG cell types they distinguish (Fig. 9 and Table 2, which are published as supporting information on the PNAS web site, for quantification). Briefly, we found that *rMrgD* and *rMrgA* are 100% coexpressed and define a single cell type that does not express *rMrgB4* or *rMrgC*. A second nonoverlapping cell type was defined by coexpression of *rMrgB4* and *rMrgB5* (Table 2) and a third by unique expression of *rMrgC*. A fourth cell type was defined by coexpression of *rMrgC* and *rMrgB4* in 27% of the *MrgC* $^{+}$ cells (Fig. 4*B* and Table 2). Thus, the number of distinct neuronal subtypes defined by the combinatorial expression of *rMrgA, rMrgB, rMrgC*, and *rMrgD* is on the same order as the number of genes (Fig. 4*B*).

Because we had not previously detected expression of *mMrgB4* or *mMrgB5* in newborn mouse DRG (11), these rat data prompted us to reexamine the coexpression of *Mrgs* in adult mouse DRG. These experiments revealed subtle differences between mouse and rat in the relative distribution of these

receptors. For example, in the rat, *rMrgB4* and *rMrgC* are partially coexpressed; however, the mouse orthologs mark two nonoverlapping populations of murine DRG neurons (Fig. 9). Furthermore, unlike the rat, where *rMrgD* is coexpressed with *rMrgA, mMrgD* is not coexpressed with any *mMrgA* genes thus far examined in the adult mouse (Fig. 4*B*). Conversely, whereas *rMrgC* never overlaps with *rMrgA* in the rat, all *mMrgC11* $^{+}$ cells coexpress *mMrgA3* in mouse (although some *mMrgA3* $^{+}$ cells are *mMrgC11* $^{-}$). We used the *mMrgA3* probe as representative of the murine *MrgA* family, because it gave the strongest signal in adult mouse DRG tissue. However, these observations were confirmed by using mixed probes containing *mMrgA1, mMrgA2, mMrgA3*, and *mMrgA4* (data not shown). These data therefore suggest that *MrgA* genes are always coexpressed with another *Mrg*, but that the companion gene differs in rat and mouse (Fig. 4*B*).

DISCUSSION

Expression of the *Mrg* family of GPCRs revealed a previously unanticipated degree of molecular diversity among murine nociceptive sensory neurons (11). Humans, in contrast, express a smaller number of related genes (12). On the one hand, *Mrg* diversity in mice could reflect aspects of sensory physiology and/or neuronal connectivity that are generic to rodents but different from that in humans. On the other hand, it could reflect genomic expansion events that are an atypical feature of mice. In an effort to distinguish these possibilities, we characterized the complement of *Mrgs* expressed in two related rodent species. Surprisingly, our data suggest that rats and gerbils each have a

single *MrgA* and *MrgC* gene, and that these subfamilies underwent a relatively recent expansion in mice, primarily via local gene duplication events. However, like mice, rats and gerbils contain several *MrgB* genes and one *MrgD* gene. These and other findings suggest that *Mrg* diversity and function in rodents can be reduced to a core set of approximately four different genes, defining a comparable number of nociceptive neuron subtypes. These observations reduce the complexity of *Mrg* diversity in rodents to a level more closely approximating the limited *Mrg* diversity in humans.

The Localized Expansion of Murine MrgA and MrgC Genes May Be Driven by Interspersed Retrotransposons and Nonhomologous Recombination Events. What mechanism(s) underlie the selective and localized expansion of the *mMrgA* and *mMrgC* subfamilies in mice? The high frequency of interspersed L1 retrotransposons in the mouse *MrgA-C* cluster (>40% L1 sequence) suggests that such repeats could have facilitated unequal crossover events that expanded these subfamilies (Fig. 5). Consistent with this idea, *Mrgs* are generally arranged in a head-to-tail (5′ to 3′) fashion. This gene arrangement, coupled with the fact that phylogenetically related genes are adjacent, strongly supports an unequal crossover mechanism for expansion (24, 25, 35). However, such a mechanism by itself would not explain why a similar *MrgA-C* expansion did not occur in rat, because the rat also contains a similarly high frequency of L1 retrotransposons surrounding the *rMrgA* and *rMrgC* genes (≈48%). One possibility is that the expansion of the murine genes could be due to local L1 retrotransposition of the *mMrg* sequence, which seems unlikely,

however, because the average *mMrgA* transcriptional unit (first and second exon ≈14 kb; Fig. 8) is significantly larger than the average length of extraneous DNA transposed by L1 elements (36).

A more likely explanation is that expansion of the murine *MrgA-C* cluster was initiated by *de novo* L1 retrotransposition into the ancestral *MrgA-C* cluster during murine evolution, followed by unequal crossover with preexisting L1 sequences to duplicate the ancestral *mMrgA* gene and create an (A-A-C) repeat (Fig. 5*A*) (37). Additional rounds of localized unequal crossover could have created the present day $(A\text{-}A\text{-}C)_n$ repeats, explaining why there are roughly twice as many *mMrgAs* (*n* = 22) as *mMrgCs* (*n* = 14) (11). Our observation that mouse *MrgAs* have L1 sequences at the 5′ and 3′ ends of their coding exons, but that rat *MrgA* has an L1 sequence only at the 5′ end of its coding exon, supports the idea that a unique retrotransposition event took place during murine evolution. Furthermore, the broader clustering of divergence times calculated for *mMrgAs* versus the more recent and compact clustering of divergence times for *mMrgCs* (Fig. 2) is consistent with the idea that the ancestral *mMrgA* duplicated first, followed by duplication of the (A-A-C) repeat. This model therefore takes into account the high level of ongoing retrotransposition as well as the large number of local gene family expansions observed in the mouse genome (10).

Such an expansion mechanism could also explain, in principle, why all of the murine *MrgC* genes except *mMrgC11* are pseudogenes, whereas numerous *mMrgA* sequences are maintained as expressed ORFs (11, 13). Because the initial (A-A-C) cluster contained the ancestral *mMrgA* gene, each additional

duplication of the (A-A-C) cluster should have included at least one expressed *mMrgA*. In contrast, the first exon of *mMrgC11* is located at the boundary of the (A-A-C) cluster, thus transcriptional regulatory elements in the *mMrgC11* gene could have been damaged or eliminated after additional duplications of the (A-A-C) cluster. This would prevent duplicated *mMrgCs* from being expressed and thereby eliminate selection pressure to maintain functional genes. Consistent with this idea, *mMrgC11* is the only mouse *MrgC* that encodes a functional and expressed receptor, is more similar to *rMrgC* than to any other mouse *MrgC* (Fig. 6), and is located in the same “ancestral” chromosomal location as *rMrgC* (11, 13).

An unequal crossover mechanism could also account for why humans have *MrgX* genes rather than orthologs of rodent *MrgAs, MrgBs*, and *MrgCs*. After such nonhomologous meiotic recombination events, one homologous chromosome gains a gene (or genes), whereas the other loses a gene (or genes) (35). It is tempting to speculate that a nonreciprocal crossover event within a primordial *MrgX-MrgB* cluster yielded recombination products differentially preserved by unique selective pressures in the rodent and primate lineages (Fig. 5*B*). In a similar fashion, red and green cone opsins, which arose from an unequal crossover event, were selectively maintained on the X chromosome of Old World primates, because trichromacy provides a selective advantage (3). Despite this nonorthologous conservation of coding sequence, members of the human *MrgX* subfamily and rodent *MrgA, MrgB*, and *MrgC* subfamilies are all expressed in nociceptive sensory neurons, supporting the idea that common

promoter and/or enhancer elements were preserved during the evolution of these families.

The Functional Significance of mMrgA Sequence Diversity in Mice. Does the fact that mice express more *MrgAs* than rats or gerbils imply that this diversity has a physiological significance unique to mice? Our analysis indicates that most intact *MrgA* coding sequences are under neutral or weak negative selection pressure ($K_a/K_s \leq 1$; Fig. 2), arguing against the idea that expansion of the *mMrgA* family was driven by positive selection for diversification of receptor coding sequences. However, this expansion could reflect positive selection for differential transcription of duplicated *MrgA* genes. Evidence for such selection, however, is difficult to glean from inspection of noncoding sequences, because calculations based on third-position changes do not apply. The relative conservation of coding sequences among the expanded family of *mMrgAs*, taken together with the fact that other rodent species examined retain a single *MrgA* gene, suggests that the various murine *MrgA* receptors may have similar or equivalent functions *in vivo*. In support of this view, both *mMrgA1* and *mMrgA4* can be activated by related RF-amide neuropeptides (11).

If the murine *MrgAs* have similar functions, the problem of *Mrg* diversity in mice would reduce to a core group of approximately four receptors (*MrgA, MrgB, MrgC*, and *MrgD*). In rats as in mice, these four receptors define a similar number of distinct neuronal subtypes (Fig. 4*B*). Because these receptors all are restricted to the GDNF-dependent subset of small-diameter nociceptive neurons in both rodent species, they are likely to play a conserved functional role in rodent

nociception. In humans, the related *hMrgXs*/*SNSRs* are also specifically expressed in subsets of small-diameter sensory neurons (12), although whether they are restricted to the GDNF-dependent subset is not yet clear. Furthermore, like *mMrgAs* and *mMrgC11*, these human receptors are activated by RF/Y-(G)/amide-containing neuropeptides (11–13). Thus, despite the evolutionary divergence of the rodent *MrgABC* and human *MrgX*/*SNSR* subfamilies, some aspects of *Mrg* function in nociceptive neurons are likely to be conserved between these mammalian species. A better understanding of these conserved functions may aid in the development of *Mrg*-specific agonists or antagonists as novel pain therapeutics.

Finally, although the mouse has been the mammalian genetic model of choice for humans, our results highlight the importance of comparing and analyzing additional rodent genomes before drawing evolutionary and functional inferences based on mouse–human differences in the size of particular gene families. This note of caution may be especially true for comparative studies of gene families, like the GPCRs, which have the potential to rapidly expand. Although such expansion may facilitate rapid functional adaptation and reproductive isolation (10, 24), it may also reflect genomic expansion events atypical of rodents, perhaps due to unique retrotransposition events occurring during evolution. Our data suggest that analysis of the completed rat genome may reveal additional instances of atypical expansions of murine gene families and argue for the sequencing of at least one additional rodent genome to serve as an outgroup for mouse–rat comparisons.

We thank Gaby Mosconi for laboratory management; Jung-Sook Chang for technical assistance; Mel Simon, Sang-Kyou Han, and Jong-Ik Hwang for helpful discussions throughout the course of this work; and Mel Simon and Cori Bargmann for comments on the manuscript. M.J.Z. was supported by the Cancer Research Fund of the Damon Runyon–Walter Winchell Foundation Fellowship (DRG-1581). X.D. is a postdoctoral fellow of the American Cancer Society, and D.J.A. is an Investigator of the Howard Hughes Medical Institute.

REFERENCES

1.Young, J. M. & Trask, B. J. (2002) Hum. Mol. Genet. 11:**,** 1153–1160.

2.Lindemann, B. (2001) Nature 413:**,** 219–225.

3.Nathans, J. (1999) Neuron 24:**,** 299–312.

4.Wang, Y., Macke, J. P., Merbs, S. L., Zack, D. J., Klaunberg, B., Bennett, J., Gearhart, J. & Nathans, J. (1992) Neuron 9:**,** 429–440.

5.Vassalli, A., Rothman, A., Feinstein, P., Zapotocky, M. & Mombaerts, P. (2002) Neuron 35:**,** 681–696.

6.Lane, R. P., Cutforth, T., Axel, R., Hood, L. & Trask, B. J. (2002) Proc. Natl. Acad. Sci. USA 99:**,** 291–296.

7.Adams, M. D., Celniker, S. E., Holt, R. A., Evans, C. A., Gocayne, J. D., Amanatides, P. G., Scherer, S. E., Li, P. W., Hoskins, R. A., Galle, R. F., *et al.* (2000) Science 287:**,** 2185–2195.

8.Lander, E. S., Linton, L. M., Birren, B., Nusbaum, C., Zody, M. C., Baldwin, J., Devon, K., Dewar, K., Doyle, M., FitzHugh, W., *et al.* (2001) Nature 409:**,** 860–921.

9.Venter, J. C., Adams, M. D., Myers, E. W., Li, P. W., Mural, R. J., Sutton, G. G., Smith, H. O., Yandell, M., Evans, C. A., Holt, R. A., *et al.* (2001) Science 291:**,** 1304–1351.

10.Waterston, R. H., Lindblad-Toh, K., Birney, E., Rogers, J., Abril, J. F., Agarwal, P., Agarwala, R., Ainscough, R., Alexandersson, M., An, P., *et al.* (2002) Nature 420:**,** 520–562.

11.Dong, X., Han, S., Zylka, M. J., Simon, M. I. & Anderson, D. J. (2001) Cell 106:**,** 619–632.

12.Lembo, P. M., Grazzini, E., Groblewski, T., O'Donnell, D., Roy, M. O., Zhang, J., Hoffert, C., Cao, J., Schmidt, R., Pelletier, M., *et al.* (2002) Nat. Neurosci. 5:**,** 201–209.

13.Han, S. K., Dong, X., Hwang, J. I., Zylka, M. J., Anderson, D. J. & Simon, M. I. (2002) Proc. Natl. Acad. Sci. USA 99:**,** 14740–14745.

14.Monnot, C., Weber, V., Stinnakre, J., Bihoreau, C., Teutsch, B., Corvol, P. & Clauser, E. (1991) Mol. Endocrinol. 5:**,** 1477–1487.

15.Young, D., Waitches, G., Birchmeier, C., Fasano, O. & Wigler, M. (1986) Cell 45:**,** 711–719.

16.Li, W. H., Wu, C. I. & Luo, C. C. (1985) Mol. Biol. Evol. 2:**,** 150–174.

17.Li, W. H. (1993) J. Mol. Evol. 36:**,** 96–99.

18.Pamilo, P. & Bianchi, N. O. (1993) Mol. Biol. Evol. 10:**,** 271–281.

19.Li, W. H., Luo, C. & Wu, C. (1985) in Molecular Evolutionary Genetics, ed. Macintyre, R. J. (Plenum, New York), pp. 1–94.

20.Bender, E., Buist, A., Jurzak, M., Langlois, X., Baggerman, G., Verhasselt, P., Ercken, M., Guo, H. Q., Wintmolders, C., Van den Wyngaert, I., *et al.* (2002) Proc. Natl. Acad. Sci. USA 99:**,** 8573–8578.

21.Kumar, S. & Hedges, S. B. (1998) Nature 392:**,** 917–920.

22.Kumar, S. & Subramanian, S. (2002) Proc. Natl. Acad. Sci. USA 99:**,** 803–808.

23.O'hUigin, C. & Li, W. H. (1992) J. Mol. Evol. 35:**,** 377–384.

24.Young, J. M., Friedman, C., Williams, E. M., Ross, J. A., Tonnes-Priddy, L. & Trask, B. J. (2002) Hum. Mol. Genet. 11:**,** 535–546. fdt

25.Zhang, X. & Firestein, S. (2002) Nat. Neurosci. 5:**,** 124–133.

26.Hunt, S. P. & Mantyh, P. W. (2001) Nat. Rev. Neurosci. 2:**,** 83–91.

27.Julius, D. & Basbaum, A. I. (2001) Nature 413:**,** 203–210.

28.Snider, W. D. & McMahon, S. B. (1998) Neuron 20:**,** 629–632.

29.Bennett, D. L., Michael, G. J., Ramachandran, N., Munson, J. B., Averill, S., Yan, Q., McMahon, S. B. & Priestley, J. V. (1998) J. Neurosci. 18:**,** 3059–3072.

30.Boucher, T. J., Okuse, K., Bennett, D. L., Munson, J. B., Wood, J. N. & McMahon, S. B. (2000) Science 290:**,** 124–127.

31.Bradbury, E. J., Burnstock, G. & McMahon, S. B. (1998) Mol. Cell Neurosci. 12:**,** 256–268.

32.Cockayne, D. A., Hamilton, S. G., Zhu, Q. M., Dunn, P. M., Zhong, Y., Novakovic, S., Malmberg, A. B., Cain, G., Berson, A., Kassotakis, L., *et al.* (2000) Nature 407:**,** 1011–1015.

33.Malmberg, A. B., Chen, C., Tonegawa, S. & Basbaum, A. I. (1997) Science 278:**,** 279–283.

34.Souslova, V., Cesare, P., Ding, Y., Akopian, A. N., Stanfa, L., Suzuki, R., Carpenter, K., Dickenson, A., Boyce, S., Hill, R., *et al.* (2000) Nature 407:**,** 1015–1017.

35.Li, W. H. (1997) Molecular Evolution (Sinauer, Sunderland, MA).

36. Goodier, J. L., Ostertag, E. M. & Kazazian, H. H., Jr. (2000) Hum. Mol. Genet. 9:, 653–657.

37. Fitch, D. H., Bailey, W. J., Tagle, D. A., Goodman, M., Sieu, L. & Slightom, J. L. (1991) Proc. Natl. Acad. Sci. USA 88:, 7396–7400.

FIGURES

Fig 1

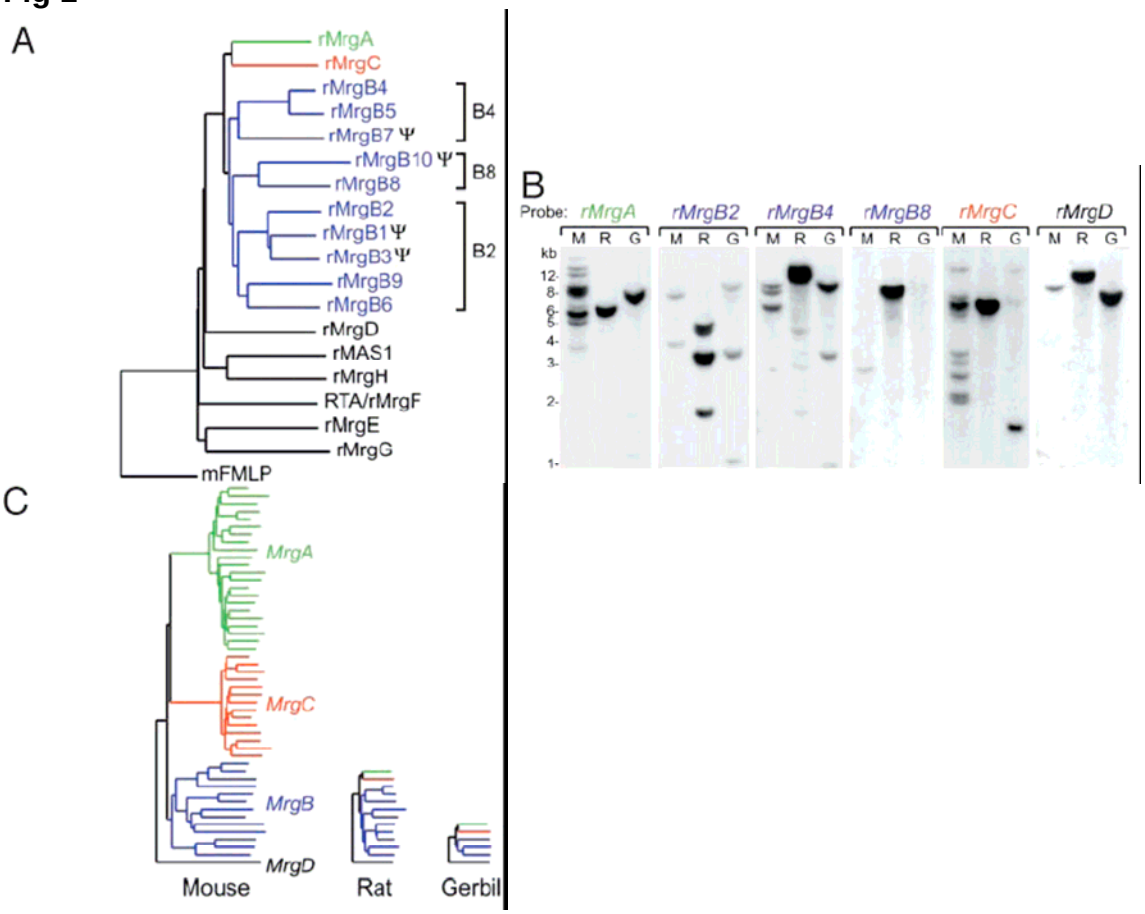

Fig. 1. Analysis of the rat and gerbil *Mrg* families. (*A*) Phylogenetic analysis of the rat *Mrg* family. The program clustalw was used to align rat MRG protein sequences and assemble them into a dendrogram by using the neighbor-joining method. The mouse formyl peptide receptor 1 (mFMLP) was used as the outgroup. Genes that fall into the B2, B4, and B8 subdivisions are bracketed. Ψ, predicted pseudogenes. (*B*) Southern blot analysis of rodent *Mrgs*. Each lane contains 9 µgof *Bgl*II digested liver genomic DNA from mouse (M), rat (R), or gerbil (G). Blots were probed and washed under high stringency conditions with the designated rat *Mrg* probes. For all lanes, no bands were visible below 1 kb. (*C*) Summary of rodent *MrgA*, *MrgB*, *MrgC*, and *MrgD* subfamilies based on data

obtained from Southern blots, degenerate PCR, and genomic analyses. For mouse and rat, the number of bands detected by Southern blotting is similar to the number of genes predicted from the draft genomic sequences.

Fig 2

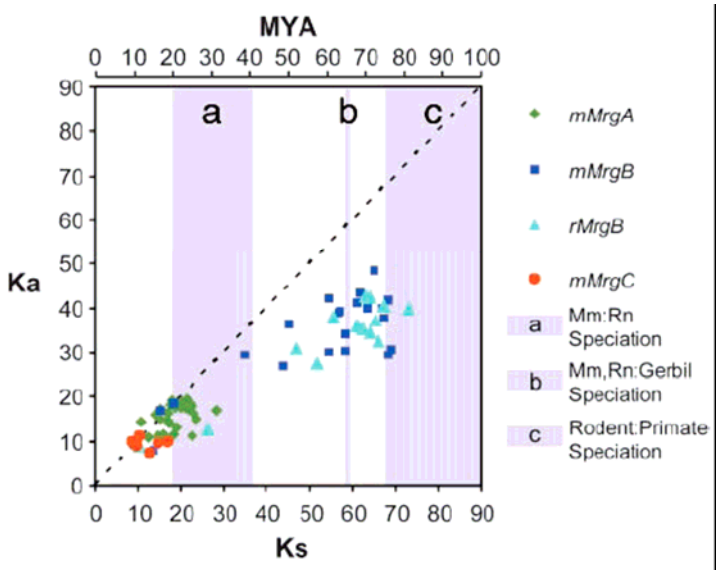

Fig. 2. Pairwise synonymous (K_s) and nonsynonymous (K_a) nucleotide substitutions per 100 sites between mouse and rat *Mrg* subfamily members. Each point represents a single pairwise comparison between *Mrgs* of the *mMrgA* (green diamonds), *mMrgB* (dark blue squares), *rMrgB* (light blue triangles), or *mMrgC* (red circles) subfamily. The dashed line marks a K_a/K_s ratio of 1.0 or neutral selection. Points below the line are considered to be under negative selection (K_a/K_s ratio <1.0) and points above, under positive selection (K_a/K_s ratio >1.0). The scale at the top of the graph relates K_s values to evolutionary divergence time in MYA. a, The shaded bar marks the approximate time when

rats last shared a common ancestor with mice 20–41 MYA (21–23). B, The shaded bar indicates the approximate time when gerbils last shared a common ancestor with rats and mice 66 MYA (21, 22). C, The shaded bar indicates the approximate time when rodents and primates last shared a common ancestor 75–115 MYA (21–23).

Fig 3

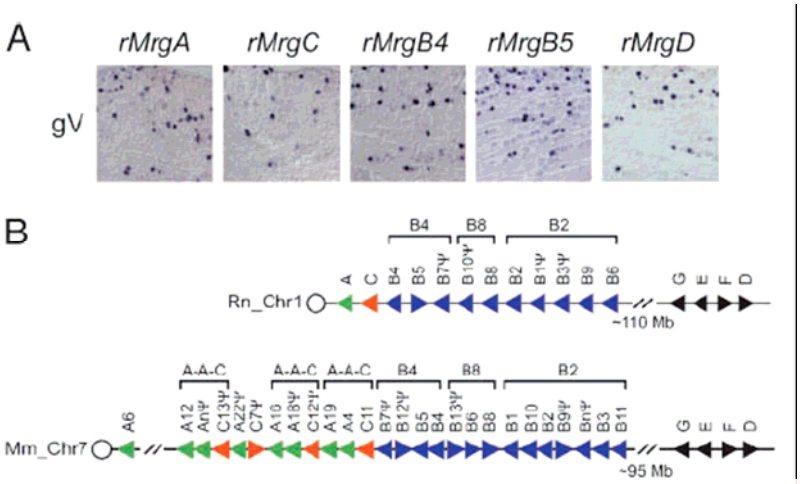

Fig. 3. Correlated expression and chromosomal localization of rodent *Mrgs*. (*A*) Expression analysis of rat *Mrgs* in adult trigeminal ganglia (gV). *In situ* hybridization was performed with antisense digoxigenin-labeled riboprobes. (*B*) Chromosomal arrangement of rat and mouse *Mrgs*. Analyses of the January 21, 2003, assembly of the rat genome and the February 24, 2003 (National Center for Biotechnology Information mouse build 30), assembly of the mouse genome revealed that most of the *Mrg* family members were located within two discrete regions of rat chromosome 1 and mouse chromosome 7. These two regions encompass the *MrgABC* cluster (760 kb in size from rat assembly NW_043369; 1.2 Mb in size from mouse assemblies NT_039420-NT_039423) and the *MrgDEFG* cluster (1.9 Mb in size from rat assemblies NW_043404-NW_043405;

1.6 Mb in size from mouse assembly NT_039437). The circle marks the relative position of the centromere. Triangles denote the direction of transcription and indicate the relative position of each gene on the chromosome. This figure is not drawn to scale. Brackets indicate the location of the three *MrgB* subdivisions. Several of the mouse A-A-C repeats are also highlighted. The mouse A-C cluster begins with *MrgA6* and ends with a misassembled fragment of *MrgC11*. We did not plot all of the *mMrgA* and *mMrgC* genes because of obvious inaccuracies in the mouse assembly.

Fig 4

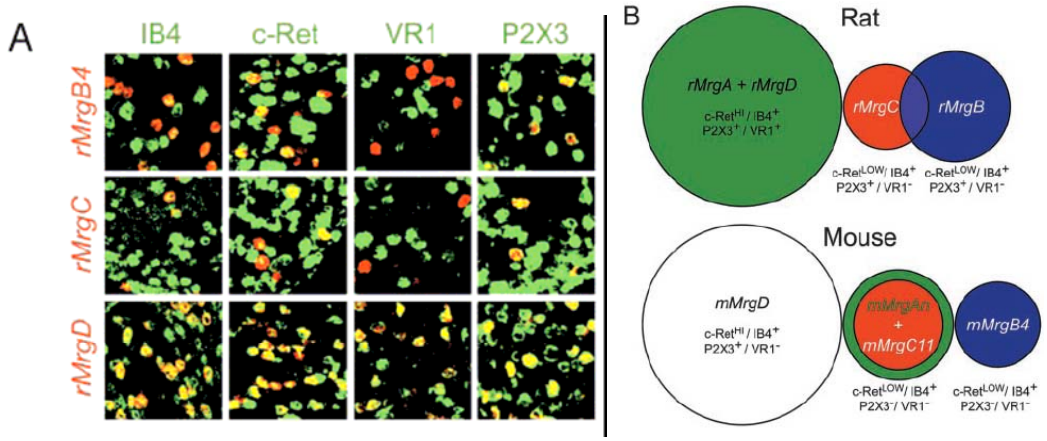

Fig. 4. Analysis of *Mrg* expression in adult rat and mouse DRG neurons. (*A*) Coexpression of rat *Mrgs* with various sensory neuron markers. With the exception of IB4, all gene combinations were detected by double-label *in situ* hybridization (ISH) with the indicated antisense cRNA probe. Fluorescein-conjugated *G. simplicifolia* IB4-lectin was applied to sections after the ISH procedure to detect IB4-binding cells. (*B*) Summary of the rat and mouse *Mrg* expression domains in adult DRG sensory neurons. The sizes of the circles in the Venn diagrams are proportional to the sizes of the cell populations. Our

results of double-label ISH among *mMrgAs*, *mMrgB4*, *mMrgC11*, *mMrgD*, and several nociceptive sensory neuron markers are also indicated (11, 13).

Fig 5

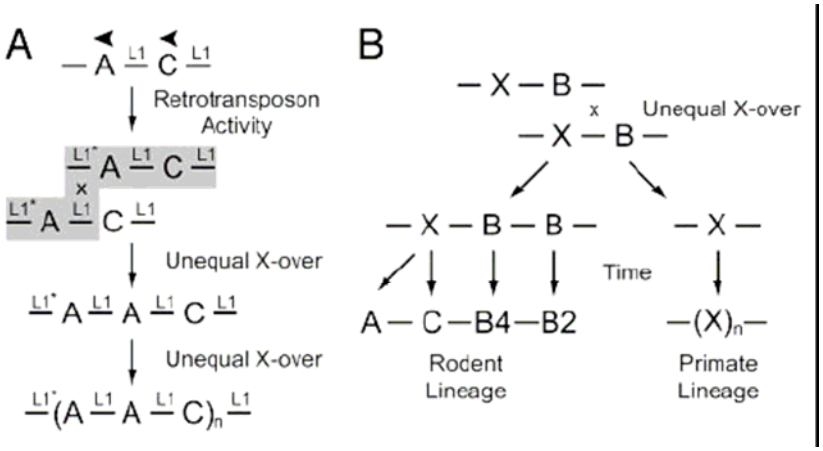

Fig. 5. Possible mechanisms for *Mrg* expansion. (*A*) Idealized mechanism for the expansion of the mouse *MrgA* and *MrgC* (-A-C-) gene cluster. First, an L1 retrotransposon inserts into the 3′ end of the ancestral murine *MrgA* gene (L1*). At a later date, an unequal crossover event occurs between this new L1* and preexisting intergenic L1 sequences, creating the initial (A-A-C) repeat. Last, additional rounds of unequal crossover take place due to the large amount of homologous L1 sequence in the local genomic environment. (*B*)An unequal crossover event could explain why rodent and primate *Mrg* families are related but not orthologous. Assume that the common ancestor of primates and rodents contained single *MrgX* and *MrgB* genes. Unequal crossover could resolve into -X-B-B- and -X-containing chromosomes. In the rodent lineage, the -X-gene may have evolved into *MrgA* and *MrgC* genes, because they appear to be more closely related to human *MrgXs* than to rodent *MrgBs* (Fig. 6 and ref. 11). In

humans, the -X-gene likely underwent additional rounds of unequal crossover to create the clustered *MrgX*/*SNSR* subfamily.

The End :)